BOOK OF ABSTRACTS

APT 2026

Exhibitors

TSI
Knowledge Beyond Measure.

Swisens

Cambustion

naneos
particle solutions gmbh

Catalytic Instruments
hot technologies · clean solutions

DEKATI

AAR
American Association for Aerosol Research

Aerosol Science and Technology

aerosol dynamics

SyNest

Prof. Inge Herrmann

ETH Zurich

Talk: *Aerosol-made nanomaterials for diagnostics and therapy*

Abstract: Aerosol-made nanomaterials can bridge precision diagnostics and targeted therapy by enabling engineered particles and devices with controlled composition, catalytic activity, imaging contrast, and biological interactions. Based on research at the Ingenuity Lab Zurich, this talk will highlight how materials engineering, advanced analytics, and simulation are combined to design clinically translatable nanomaterials for precision medicine, including contrast and imaging agents, infection sensing platforms, and nanoparticle radioenhancers that improve radio- and proton-therapy performance while reducing side effects.

Prof. Lutz Maedler

U. Bremen and Leibniz Institute for Materials Engineering IWT

Talk: *Hetero aggregates – building blocks for many applications*

Abstract: Essential key technologies, for example in the context of digitalization for Industry 4.0 (sensor technology), energy conversion (catalysis) and energy storage as well as e-mobility (battery technology) or also life science, depend on functional disperse particle systems with very specific functional properties. Particles are rarely present individually and isolated, but mostly as powder or heap, so interactions occur between particles at their points of contact. If particles of different materials are present, contacts between different particles can occur, and these hetero contacts are of fundamental importance for functional properties and many applications. This lecture discusses how such hetero contacts can be created specifically by mixing particles in the gas phase and how they can be made visible or measurable, focusing on double and triple flame spray pyrolysis, the role of mixing in determining the number and quality of hetero contacts, and the need for transmission electron microscopy coupled with AI to characterize interfaces at the scale of roughly 10 nm primary particles.

Prof. George Sotiriou

SciLifeLab, Department of Chemistry, Stockholm University, Sweden

Talk: *Flame-made high-value nanoparticles for biomedicine*

Abstract: Flame aerosol technology has emerged as a highly scalable and reproducible manufacturing route for engineering high-value nanomaterials. This talk highlights recent advances in developing flame-made nanoparticles tailored for cutting-edge biomedical applications, focusing on diagnostics, antimicrobial strategies, and smart therapeutic platforms. It covers the precise structural engineering of plasmonic nanoaggregates for highly uniform surface-enhanced Raman scattering substrates and silver nanoparticle-based colorimetric sensors, multifaceted strategies against bacterial biofilms and medical device infections using nanostructured implant coatings, photocatalytic nanocomposites, and superhydrophobic coatings, and the integration of flame-made nanomaterials into advanced delivery systems such as near-infrared photothermal microneedles and tunable CaP-SiO2 nanoparticles. Overall, the lecture shows how the precision and scalability of flame synthesis can accelerate the clinical translation of next-generation nanomedicines.

Prof. Andreas Guentner

ETH Zurich & University Hospital Zurich | Co-Founder Alivion AG

Talk: *Nanoparticle and Surface Engineering with Aerosols for Chemical Sensors*

Abstract: Aerosol technologies are exceptionally versatile for the synthesis of nanostructures, offering precise control over particle size, composition, and phase across a wide functional materials space. This versatility has enabled the scalable fabrication of high-performance molecular sensors, where steep thermal gradients and high particle concentrations in combustion-derived aerosols give access, for instance, to metastable phases and high surface defect densities. In this lecture, Prof. Guentner discusses recent progress in nanoparticle synthesis using aerosol technology, with particular emphasis on surface engineering to tune the sensitivity, selectivity and reversibility of molecular sensors. The talk moves from the atomic-scale design of highly reactive surface sites to the interfacing of functional nanoparticles with microelectronic circuitry and device integration for health and environmental monitoring in terrestrial and space applications, concluding with key challenges and opportunities for translation from laboratory to industry.

Prof. Epaminondas Mastorakos, FREng

University of Cambridge | Co-Founder Pinepeak Ltd

Talk: *Real and virtual particle and aerosol transport in wildfires: the underlying science and the business case*

Abstract: Fast wildfire propagation and its effects on land, property, and human health, especially in the wildland-urban interface, are devilishly complex due to a combination of combustion mechanisms including convection, radiation, embers, smoke and haze transport, fluid mechanical aspects such as turbulence, buoyancy, heat-release modifications on the wind and aerosol dynamics, materials and construction choices, and response actions such as water, retardants and aerial bombardment. This lecture presents a comprehensive modelling framework developed at the University of Cambridge and Imperial College and recently commercialised, briefly addressing the pertinent fundamentals and the resulting requirements for underlying data analysis, while focusing on how modelling can inform firefighter response, preventive measures and risk assessment, and how it connects to the surrounding business and policy ecosystem by optimizing resources and quantifying wildfire risk with high granularity.

Closing the loop: Processing End-of-Use Photovoltaic Silicon in a Gas Phase Reactor for Application in Additive Manufacturing

S. Kuns[1], C. Kunz[2], F. Kunze[1], G. Schierning[3,4], J.K. Hufenbach[2] and S.M. Schnurre[1,4]

[1]Institut für Umwelt & Energie, Technik & Analytik e.V. (IUTA), Duisburg, 47229, Germany
[2]Leibniz Institute for Solid State and Materials Research (IFW) Dresden e.V., 01069, Germany
[3]University of Duisburg-Essen, Institute for Energy and Materials Processes Applied Quantum Materials (EMPI), University of Duisburg-Essen, 47057, Germany
[4]Center for Nanointegration Duisburg-Essen (CENIDE), 47057, Germany
Keywords: gas phase synthesis, additive manufacturing, sustainable process development, pilot scale.

Presenting author email: schnurre@iuta.de

The efficient recycling and reprocessing of end-of-use (EoU) photovoltaic (PV) silicon represents a key challenge in sustainable resource management and circular economy. This work investigates gas-phase synthesis as a method for conditioning PV silicon microparticles targeting a particle size distribution with optimal flow properties to meet the requirements of laser powder bed fusion (PBF-LB/M) – a dominating metal additive manufacturing process.

Initially, the morphologically highly undefined EoU PV silicon (Figure 1, left) was converted into a powder in the µm range (Figure 1, right). Subsequently, continuous feeding into a hot wall reactor (HWR) was performed via a special powder feeding system.

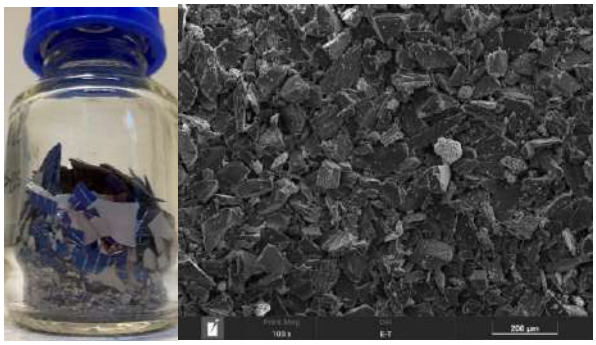

Figure 1: Silicon recovered from EoU PV modules before (left) and after (right) the first processing step.

The HWR was operated under inert conditions with working temperatures below silicon's melting point, to investigate whether thermal treatment could induce superficial particle softening and rounding. However, even a long residence time does not affect the morphology of the PV silicon powder. As a subsequent approach, thermal decomposition of silane was employed to generate free silicon atoms for the surface modification of PV silicon particles. This led to irregular island-like layer growth and nanoparticle formation, rather than the desired rounding. These results demonstrated that the HWR approach was unsuitable for morphological modification of EoU PV silicon.

A process technology change to a microwave supported plasma reactor enabled the conversion of the coarse, spattered PV silicon powder to rounded particles.

By varying residence time of the PV silicon powder in the active plasma, controlled morphological modification was achieved. The result was either a modified morphology of the PV silicon without sharp edges (Figure 2) or a complete evaporation of the PV silicon and the formation of new nanoparticles. The wide range of materials that can be produced thus demonstrates the high flexibility of the process.

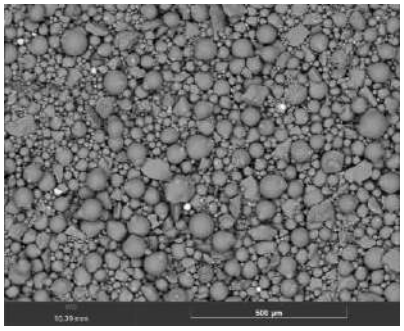

Figure 2: Rounded PV silicon particles after treatment in the microwave plasma reactor.

This work demonstrates that microwave plasma technology combined with powder feeding technology represents an energy-efficient, scalable method (kg/h range potential) for conditioning recycled PV silicon for additive manufacturing, thereby saving both costs and resources.

This work was supported by the Federal Ministry for Economic Affairs and Energy under grant 01F22324N.

Duan, Y. et al. (2024) *Chemical Engineering Journal*. **500**, 157132.

Mariotti, D, Mohan Sankaran, R. (2011*) Journal of Physics D: Applied Physics*. **44 (17)**, 174023

Kortshagen, U.R. et al. (2016) *Chemical Reviews.* **116(18)**, 11061-11127.

Sehhat M.H. et al. (2022) *International Journal of Refractory Metals and Hard Materials.* **103**, 105764.

Eco-friendly Fast-facile Synthesis of Single-phase Hydroxyapatite Nanoparticles for Biomedical Applications

A. Charmforoushan[1], M. Sorvali [1], T. Ylihärsilä [1] P. Karjalainen[1], I. Urlic[2], A. Ressler[3] and J. M. Mäkelä[1]

[1]Aerosol Physics Laboratory, Physics Unit, Tampere University, Tampere, FI-33014, Finland
[2]Department of Biology, University of Zagreb, Zagreb, HR-10000, Croatia
[3]Department of Materials Science, Tampere University, Tampere, FI-33014, Finland
Keywords: Calcium Phosphates, Flame Spray Synthesis, Biocompatibility, Particle Size Distribution.

Presenting author email: alireza.charmforoushan@tuni.fi

Hydroxyapatite (HAp) is a key bioceramic for biomedical applications due to its chemical resemblance with hard tissues. It makes up about 70 % of bone and 90 % of tooth enamel and is highly biocompatible as well as bioactive. In addition, HAp is widely used in numerous nonmedical industrial and technological fields.

Nanostructured HAp bioceramics demonstrate enhanced functional performance relative to microscale HAp, primarily owing to their high specific surface area (SSA), i.e., increased surface reactivity. Consequently, significant research efforts have focused on developing synthesis methods for nanostructured HAp.

The high demand for HAp nanoparticles, and environmentally sustainable aspects has driven the development of an eco-friendly, simple, scalable, adjustable, fast, and continuous pathway for producing HAp nanoparticles. In this study, a newly developed flame aerosol synthesis method, Liquid Flame Spray (LFS), is introduced for HAp nanoparticle production, providing a process that meets all these criteria. The LFS technique is a flame aerosol method that employs a turbulent, high-temperature hydrogen–oxygen flame and does not rely on combustible solvents. Consequently, LFS can be considered an eco-friendly synthesis route, as it enables nanoparticle production in the absence of organic solvents and surfactants.

In this study, the single-phase HA nanoparticles were successfully synthesized feeding a water-based precursor into the flame without using any organic solvents and/or surfactants as shown in Fig. 1. The influence of synthesis parameters, particularly hydrogen flow rate, precursors concentration, and feeding rate of the liquid precursors on phase purity and particle characteristics was systematically investigated. Increasing the hydrogen flow rate enhanced flame humidity and residence time, effectively preventing the formation of secondary calcium phosphate phases and residual (sub-)micron particles. Under optimized conditions, phase-pure HAp nanoparticles with an average size of ca. 8 nm and an exceptionally high SSA of about 250 m^2/g were obtained.

Beyond structural and physicochemical characterization, the biomedical relevance of the LFS-synthesized HAp nanoparticles was assessed through cytotoxicity and protein adsorption studies. The nanoparticles exhibited no cytotoxic effects, confirming their biocompatibility, while protein adsorption tests demonstrated excellent surface–protein interactions, attributed to their nanoscale size and high SSA. These results indicate strong potential for biomedical applications.

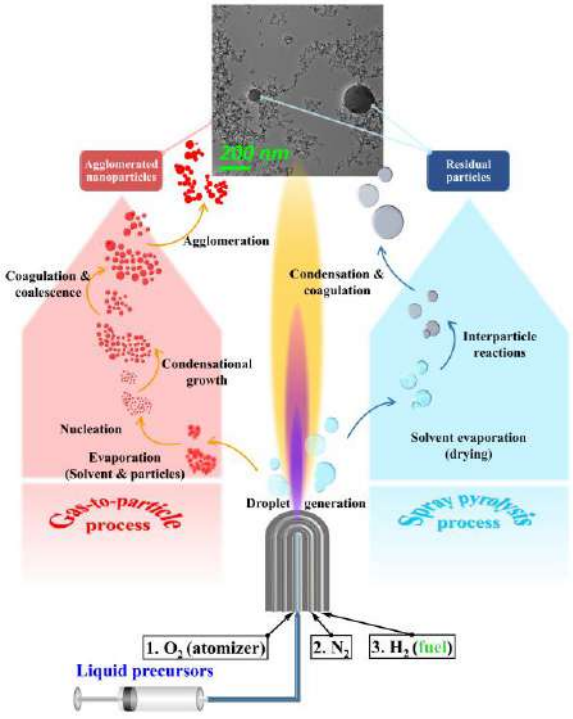

Figure 1. Schematic figure of the experimental setup for LFS synthesis of HAp nanoparticles.

This work was supported by the Doctoral School of Tampere University and Research Council of Finland, under grant 339545.

S. Pai *et al* (2020) *Journal of Water Process Engineering.* **38**, 101574.
O. Oni *et al* (2022) *Materials Chemistry Frontiers.* **7**, 9-43.
A. Charmforoushan *et al* (2025) *Materials Today Chemistry.* **43**, 102448.
A. Charmforoushan *et al* (2025) *Ceramics International.* **51**, 65273–65285.

Gas-Phase Engineering of Heterogeneous Metal Nanoaggregates

C. Jourdain[1] and A. Boies[1]

[1]Department of Mechanical Engineering, Stanford University, Stanford, 94305, USA
Keywords: metal, aggregates, plasmonics, coating, energy.

Presenting author email: cyprien@stanford.edu

Metal fractal nanoarchitectures are of growing interest due to their exceptional radiative properties and high surface-area-to-volume ratios. Their tunable morphology makes them particularly attractive for catalysis and energy-related applications, as well as for label-free DNA sensing and cancer therapy, where gap-dependent plasmon shifts and near-field enhancement can be exploited (Sotiriou, 2014). In wet-chemical synthesis routes, nanocages can confine nanocargoes, including catalysts, biomolecules, or drugs, while preserving plasmonic coupling for sensing, photothermal, and photochemical applications (Skrabalak, 2008). By contrast, gas-phase processing provides a continuous, ligand-free alternative for engineering heterogeneous nanostructures with controlled composition, tailored optical response, and functional architecture. Here, we demonstrate a single-step gas-phase approach for synthesizing metal aggregates and tuning their intrinsic properties.

Figure 1 shows bare metal aggregates including Al, Mg, and W, generated by evaporation-condensation and ablation techniques. In parallel, optical simulations were performed to quantify radiative properties as a function of particle size and morphology. The resulting structures span from primary particles below 10 nm to fractal aggregates with diameters of several hundred nanometers. Aggregate gyration diameter and compactness are controlled by agglomeration kinetics and surface energy, with additional compaction induced by capillary forces or surface- and grain-boundary-driven sintering. Size, mass, and effective density were continuously monitored using dedicated aerosol instrumentation.

Figure 2 illustrates the construction of heterogeneous silver-based nanostructures, revealing pronounced changes in physical properties through aggregate-sphere attachment (Jourdain, 2025). These results demonstrate that metal aggregate cores can not only be compacted via condensation but also functionalized through electrostatically driven attachment of secondary species. These combined mechanisms provide key building blocks for more complex gas-phase-synthesized nanomaterials, such as metallic nanocages and nanoframes. Overall, gas-phase tuning of metal aggregates opens new pathways for the scalable synthesis and application of high-value heterogeneous nanomaterials with engineered structure and functionality.

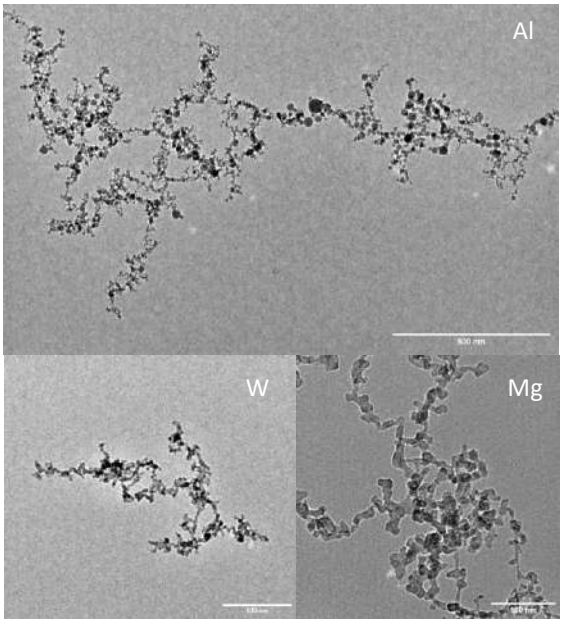

Figure 1. Examples of TEM images of synthesized metal aggregates: aluminum (limited sintering), tungsten (limited sintering), and magnesium (advanced sintering)

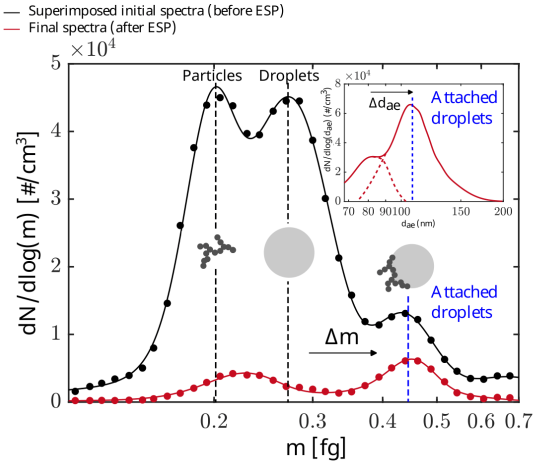

Figure 2. Mass and aerodynamic diameter (inset) distributions of attached silver aggregates and droplets. Spline fits to guide the eye only (Jourdain, 2025)

Sotiriou, G.A. *et al.* (2014) *Advanced Functional Materials.* **24**, 2818-2827.

Skrabalak, S.E. *et al.* (2008) *Accounts of Chemical Research*. **41**, 1587-1595.

Jourdain, C. (2025) *Physical and radiative properties of coated nanoparticle aggregates,* University of Cambridge.

Generating Nanoparticles from Tellurium, Bismuth, Gallium, Gold, Iron and Various Salts Using the Silver Particle Generator

V. Berger[1], P.S. Bauer[1], M. Dollner[1], K.M. Risby[2], H.J. Schulz[1], J. Swanson[1,3], A. Boies[1,4]

[1]Catalytic Instruments GmbH & Co.KG, 83026 Rosenheim, Germany.
[2]University of Cambridge, Department of Engineering, Cambridge CB2 1PZ, United Kingdom.
[3]Minnesota State University, Mankato, MN 56001, United States.
[4]Stanford University, Department of Engineering, Stanford, CA 94305, United States.
Keywords: metal particles, aerosol, DMA calibration, evaporation, condensation.

Presenting author email: vinicius.berger@catalytic-instruments.com

Generating aerosol in a defined, stable and reproducible way is a crucial part of many aerosol studies, instrument calibrations (e. g. EN 16976:2024) and technical applications. The evaporation-condensation method has been established as one of the most versatile and reliable techniques to generate nanoparticles from different materials, e.g., from salts, metals or even plastics (Scheibel and Porstendörfer, 1983; Wlasits et al., 2022). However, the equipment used for these experiments is typically a large tube furnace, which is bulky and slow. This limits the number of experiments per week, as each day, typically two hours are needed for heatup and two hours for cooldown. Usually, it is not allowed to keep the furnace running overnight due to safety concerns. Exchanging aerosol material is therefore possible only once a day.

The Silver Particle Generator (SPG) from Catalytic Instruments (CI) was developed to standardize the evaporation-condensation generation method (Hammer et al., 2022) and despite its name, it can be used with all different kinds of materials (Krasa et al., 2025). The focus of this work is to show which aerosols can be generated from various materials which this device. It offers several benefits regarding this application: it is a compact device that can heat up in less than 30 minutes. Cooldown takes approximately one hour. Exchange of material can be done in 15 minutes by replacing the tube set. The usable temperature range of the heated section is 100 to 1250 °C. For the work shown here, a maximum of 1350 °C could be reached. Furthermore, the device generates aerosol in a very stable and repeatable manner due to its precise temperature control.

In all experiments mentioned here, nitrogen was used as a carrier gas to avoid oxidation. To vaporize considerable amounts of material from the solids investigated, it is necessary to heat the materials up close to the melting point. Sufficient vapor concentration is needed for homogeneous condensation i. e. particle nucleation.

An overview of the materials investigated and resulting aerosol geometric mean diameters are shown in Figure 1.

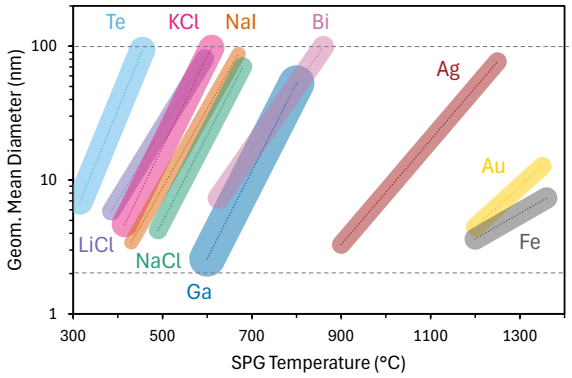

Figure 1. Geometric Mean Diameters (GMD) of the polydisperse aerosols generated by evaporation-condensation of various materials in a Silver Particle Generator.

The temperature of the SPG was varied to obtain GMDs from approx. 5 to 100 nm. Mostly due to the exponential nature of the vapor pressure curves of the materials, the GMD curves plotted logarithmically over temperature appear as linear functions. Additionally, effects like coagulation and loss mechanisms play important roles in generating the observed particle size distributions. The ability to generate aerosol from the materials presented here in a fast, simple and reproducible manner gives this method significant potential in materials research.

EN 16976:2024 (2024) *European Committee for Standardization*.

Hammer, T., Irwin, M., Swanson, J., Berger, V., Sonkamble, U., Boies, A., Schulz, H., and Vasilatou, K. (2022). *J. Aerosol Sci.* **163**:105978.

Krasa, H., Risby, K.M., Kupper, M., Bergmann, A., and Boies, A.M. (2025). *Aerosol Science and Technology*. **59:9**, 1151-1162

Scheibel, H.G. and Porstendörfer, J. (1983). *Journal of Aerosol Science* **14 (2)**:113.

Wlasits, P.J., Stöllner, A., Lattner, G., Maggauer, K., and Winkler, P.M. (2022). *Aerosol Science and Technology* **56 (2)**:176.

Predicting aerogel formation in aerosol phase nanowire synthesis

N. Abomailek[1,2], A. Boies[3] and J.J. Vilatela[1]

[1]IMDEA Materials Institute, Getafe, Madrid, 28906, Spain
[2]Department of Applied Physics, Universidad Autónoma de Madrid, Cantoblanco, Madrid, 28049, Spain
[3]Department of Mechanical Engineering, Stanford University, Stanford, CA, 94305, USA

Keywords: nanowire, DLCA, percolation, agglomeration, kinetics.

Presenting author email: nabil.abomailek@imdea.org

Floating Catalyst Chemical Vapour Deposition (FCCVD) is a promising technique for the synthesis of 1D nanomaterials and their assembly into macroscopic networks. It consists of the growth and agglomeration of 1D nanostructures in the aerosol phase. When performed for synthesizing carbon nanotubes (CNT), the floating CNTs collide with each other and form a connected network that develops into a macroscopic aerogel, which can be pulled out of the reactor outlet as a continuous fibre, forming the basis of a fibre spinning process (Li *et al.,* 2004). This technique has recently evolved as a universal method for inorganic nanowire (NW) synthesis. Under FCCVD, NWs can be directly assembled into aerogels by deposition, but they still do not show the spontaneous gelation process of CNTs (Gómez-Palos *et al.,* 2023), hindering direct nanotextile fabrication routes. Recently, we described FCCVD-synthesised silicon NW agglomerates collected from the aerosol phase by their apparent fractal dimension (D_f = 1.8) measured by SEM (Abomailek *et al.,* 2025). Through these morphological factors, we concluded that SiNW agglomerates needed longer times than CNTs to reach percolation and form an aerogel in the gas phase.

In this new study, we further investigate the possibilities of aerogel generation from NW aerosols. Specifically, we built a diffusion-limited cluster agglomeration code to simulate Brownian agglomeration of SiNWs in the gas phase. NW populations with different size distributions and volume fractions were generated. Then, NWs walk in random paths and agglomerate upon collision, following size-dependent translational and rotational diffusivities derived from Boies *et al.,* 2019.

For different NW initial size distributions, we obtained D_f = 1.3-1.9. Due to their low fractal dimensionality and the high aspect ratio of their primary particles, the excluded volume of different agglomerates overlaps as they grow. The consequences of this effect are an increase of the kinetic exponent of agglomeration, and the formation of D_f = 2.5 clusters of agglomerates formed by several agglomerates jamming together when they are in proximity. The evolution of the kinetic exponent can be extracted from Smoluchowski kinetics graphs, and the two fractal dimensions of agglomerate clusters can be measured by q-factor analysis of their scattering profiles (Fig 1). Depending on the aspect ratio of the nanowires, these effects happen at volume fractions that are 3 to 4 orders of magnitude lower than the ones described for spherical particle agglomerates (Sorensen and Chakrabarti, 2011).

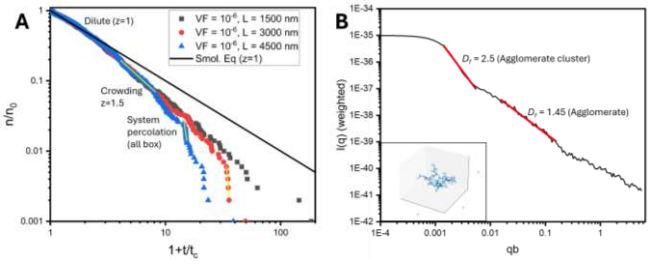

Figure 1. A) Normalized number concentration vs a characteristic time scale. Slope indicates the evolution of the kinetic exponent (z) for different NW populations. B) Scattering profile of an agglomerate cluster showing an external agglomerate cluster D_f (2.5), and an internal agglomerate D_f (1.45).

By combining the calculated collision kinetics with fractal percolation models, we built time-scale maps in which we predict if a nanowire population will evolve into a full-volume spanning aerogel or will remain an aerosol of high and/or low fractal dimension agglomerates.

This work was supported by the European Research Council under UNIYARNS grant (101045394).

Abomailek, N., Gómez-Palos, I., Carnicero, C., Murillo, M., Schäufele, R.S., Qiao, R., Boies, A. and Vilatela, J.J. (2025). *Small,* **21**(9), 2409673.

Boies, A., Hoecker, C., Bhalerao, A., de la Verpilliere, J., Graves, B. and Smail, F. (2019) *Small*, **15**(27), 1900520.

Gómez-Palos, I., Vazquez-Pufleau, M., Schäufele, R.S., Mikhalchan, A., Pendashteh, A., Ridruejo, A. and Vilatela, J.J. (2023). *Nanoscale* **15**, 6052-6074.

Li, Y., Kinlock, I. A. and Windle, A.H. (2004). *Science*, **304**, 276-278.

Sorensen, C.M. and Chakrabarti, A. (2011). *Soft Matter*, **7**, 2284-2296.

Spark ablation of Ti and Au for Au@TiO_2 hetero-aggregate nanoparticle formation and characterisation

Benjamin Gfeller[1], Mariia Becker[1], Aaron Oechsle[2], Patrik Willi[3], Sebastian Langloz[1], Christoph Schmidt[1], Thomas Jung[2], Wendelin Stark[3], Markus Kalberer[1]

[1]Department of Environmental Sciences, University of Basel, Basel, 4056, Switzerland
[2]Center for Photon Science, Paul Scherrer Institute, 5232 Villigen, Switzerland
[3]Institute of Chemical and Bioengineering, Department of Chemistry and Applied Biosciences, ETH Zurich, Zurich, 8093, Switzerland
Keywords: spark ablation, TiO_2 phase tuning, Au hetero-aggregation, functional nanoparticles, nanoparticle characterisation.

Presenting author email: benjamin.gfeller@unibas.ch

Various ways of generating nanoparticles have been developed in recent years. An effective way, using a precursor-less method, is the generation of nanoparticles via the physical process of spark ablation (Tabrizi, 2009). This gas phase production method offers high purity and high number concentrations of well above 10^6 particles per cm^3.(Gfeller, 2025) Applications of this method include the functionalization of nanoparticles such as the oxidation of non-noble metals as well as hetero-aggregations.

This study focuses on the generation of spark ablated and in situ oxidized Ti(O_2) nanoparticles, using a spark generator (Palas, Karlsruhe, GER) and a high temperature oven for oxidation and modification of particle crystal structure and morphology. Furthermore, Au nanoparticles are generated via spark ablation (VSParticle, Delft, NL) and coated on the TiO_2 particles to form hetero aggregates.

Resulting aggregates are analysed via transmission electron microscopy (TEM) and scanning electron microscopy (STEM) combined with electron dispersive X-ray spectroscopy (EDX). Crystal phases and oxidation states are analysed via X-ray diffraction (XRD) and X-ray photoemission spectroscopy (XPS) of particles collected on filters. Optical properties are determined using UV-vis absorption measurements.

TiO_2 particle properties could be tuned by passing them through a furnace at varying temperature between 500 and 1000°C. Lower temperatures produce highly fractal particles with sub 5 nm primary particles predominantly in the anatase phase exhibiting a high number of defects. Higher temperatures result in less fractal structures with less defects and a smaller bandgap. TiO_2 crystal phases can be tuned to 80:20 anatase to rutile ratio, the optimal ratio for photocatalysis (Figure 1).

Au particle coating decreased the bandgap of TiO_2 for 500 and 750°C (Figure 2). The most pronounced decrease occurred for TiO_2 generated at 750°C simultaneously also increasing the absorbance in the visible range (i.e. an increase in the Urbach tail as well as the absorbance due to the excitation of localised plasmon resonances in Au).

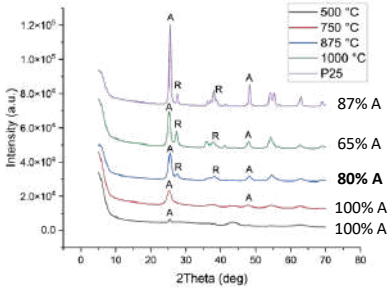

Figure 1. XRD spectra for TiO_2 generated at oxidation temperatures between 500 and 1000°C compared to P25 reference TiO_2 powder.

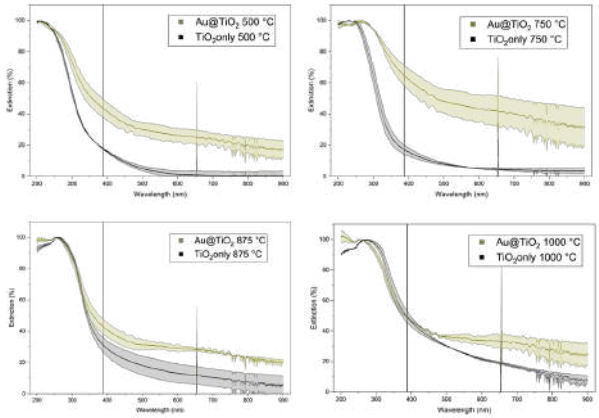

Figure 2. UV-vis extinction spectra for TiO_2 (black) and Au@TiO_2 (red) for all temperatures.

This work was supported by the Swiss National Science Foundation (200021_192192/1).

Tabrizi, N. S., Ullmann, M., Vons, V. A., Lafont, U. and Schmidt-Ott, A. (2009) J. Nanopart. Res. **11**, 315-332.
Gfeller, B., Becker, M., Aebi, A. D., Bukowiecki, N., Wyss, M. and Kalberer, M. (2025) Aerosol Res. **3**, 351–369.

The effect of inductance-controlled energy release rate on the plasma resistance and size distribution of copper nanoparticles generated by spark-discharge discharge ablation

J. Morán[1], S. Bin Karim[1], D. Konguende[1] and Q. Fu[2]

[1]Department of Mechanical Engineering, University of Ottawa, Ottawa, K1N 6N5, Canada
[2]Department of Mechanical Engineering, University of Minnesota, 55455, USA
Keywords: External inductance, Nanoparticle Synthesis, Spark Ablation, Copper, Thermal channel.

Presenting author email: jose.moran@uottawa.ca

Spark-discharge ablation (SDA) exhibits high versatility to produce nanoparticles with precisely controlled size and composition, significant throughput (mg/h in bench laboratory settings), repeatability, and stability (Pfeiffer *et al* (2014)). Different alternatives have been explored to control the produced nanoparticles by changing electrodes geometry/distance, flowrate, and electrical properties of the circuit. For instance, increasing the electrical resistance of the circuit is an effective way to change single discharge regime from (commonly) underdamped to critically or even overdamped resulting in smaller particle mean mobility diameters (Kohut *et al* (2018)). However, this approach is energy inefficient. An alternative is to modify the circuit inductance to control the energy release rate of single discharges without significant energy lost as heat. Excepting a few works from the literature (*e.g.* Vazquez-Pufleau *et al* (2023)), this parameter has received little attention and its effect on both the discharge properties and nanoparticle size distribution is unclear.

We have developed a custom-made SDA nanoparticle generator operated at 3 L/min nitrogen flow (99.999% purity; nearly atmospheric pressure). Electrodes (0.67 mm gap distance, cylindrical/flat head, 3.15 mm diameter Cu 99.95% purity) are aligned perpendicular to the gas flow axis. One of the electrodes is grounded and the other is connected to a high-voltage RLC circuit (10 nF capacitance, 7.10 µH inductance, and 3.06 Ω resistance), and 1 mA charging current. In this circuit we have added external inductors of 10, 50, 100 and 560 µH. Discharge voltage and current were measured showing a duration of individual discharges to monotonically increase from 7.1 µs (no external inductance) to 60 µs (for 560 µH). Energy release of individual discharges was calculated yielding values from 37 to 80% of the capacitors stored energy (45 mJ).

Based on an analytical fit of the time-evolving current and voltage of single discharge ringing oscillations, a constant discharge resistance was obtained (dashed lines in Fig. 1i). In addition, we have developed a new simple adiabatic model where an energy balance equation (including Ohmic heating and coupled to the electric circuit dynamic response) is solved to model the expansion of the thermal channel formed during discharges predicting a time-decreasing plasma resistance (Continuous lines in Fig. 1i). The latter magnitudes may be explained by the individual discharge ringing frequency, energy, plasma channel geometry and temperature. Indeed, external inductance seems to drastically affect the light emission from discharges, and deflected thermal channels were observed when external inductance is increased (Fig. 1a-h). Fig. 1j shows scanning-mobility particle spectrometer measured size distributions. In all cases, a unimodal size distribution exists with a narrow peak below 10 nm. Excepting in the case of 50 µH, external inductance tends to shift the size distribution towards larger geometric mean values.

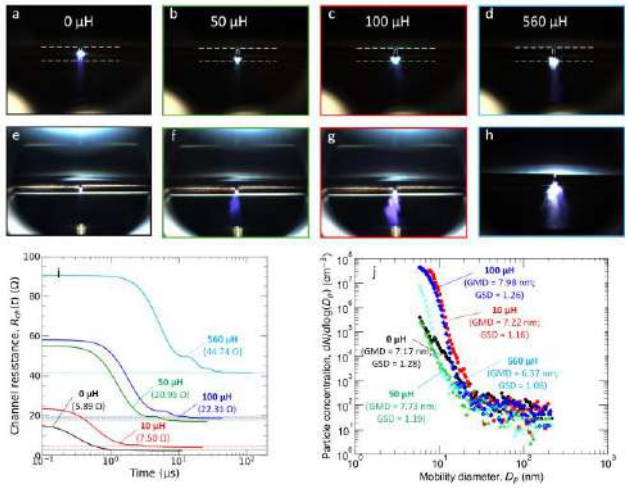

Figure 1. Spark-discharge channel imaging, resistance, and particle size distribution at different external inductances (in µH).

This work was supported by NSERC Canada, under grant RGPIN-2025-04803.

Kohut, A., Villy, L.P., Ajtai, T., Geretovszky Z., Galbacs, G. (2018) *Journal of Aerosol Science*. 118:59–63.

Pfeiffer, T.V., Feng, J., Schmidt-Ott, A. (2014) *Advanced Powder Technology*. 25(1):56–70.

Vazquez-Pufleau, M., Gomez-Palos, I., Arevalo, L., Garcia-Labanda, J., Vilatela, J.J. (2023) *Advanced Powder Technology*, 34(3):103955.

Time-resolved composition of CuZn nanoparticles generated by spark ablation

Linnéa Jönsson[1,2], Vinzent Olszok[3], Dániel Megyeri[4], Thomas Krinke[1,2], Calle Preger[5], Jenny Rissler[2,6], Axel. C. Eriksson[2,6], Zsolt Geretovszky[4], Knut Deppert[1,2], Alfred P. Weber[3], Attila Kohut[4], and Maria E. Messing[1,2,7]

[1]Solid State Physics and NanoLund, Lund University, 221 00, Lund, Sweden
[2]NanoLund, Lund University, 221 00, Lund, Sweden
[3]Clausthal University of Technology, Institute of Particle Technology, 38678, Clausthal-Zellerfeld, Germany
[4]Department of Optics and Quantum Electronics, University of Szeged, 6720, Szeged, Hungary
[5]MAX IV Laboratory, Lund University, Box 118, Lund 221 00, Sweden
[6]Ergonomics and Aerosol Technology, Lund University, 221 00, Lund, Sweden
[7]Quantum Device Physics Laboratory, Department of Microtechnology and Nanoscience, Chalmers University of Technology, 412 96, Gothenburg, Sweden
Keywords: spark ablation, nanoparticles, time-resolved, composition.

Presenting author email: linnea.jonsson@fysik.lu.se

Spark ablation is a versatile method that can generate an aerosol consisting of metal and metal oxide nanoparticles (NPs) in a carrier gas. Compared to wet chemical production routes, spark ablation effectively avoids the various necessary steps for surface contamination removal, since the particles are produced in a gas. Furthermore, spark ablation offers a myriad of materials mixing capabilities, as all conductive materials can be used as feedstocks and mixed on the nanoscale using this technique, and with control over the resulting NP composition.

Previous studies have indicated that even if using feedstocks made of alloys containing elements with different melting points or vapor pressures, the composition of the resulting particles will still retain the same composition as the electrodes due to the fast dynamics of the generation process (Jönsson et al., 2024; Tabrizi et al., 2009b). In this study, we show that this is not the case for CuZn (brass) alloys.

The focus of this project is advanced and time-resolved compositional analysis of CuZn nanoparticles produced via spark ablation. The NP composition is investigated by analysing individual particles (TEM-EDS), an ensemble of particles (ICP-MS, XRF), and their surface while still suspended in gas (in-flight XPS), using time-resolved techniques. To understand the dynamics of particle formation, atomic species in the plasma are observed over time by optical emission spectroscopy (OES). The feedstock is analysed by SEM-EDS.

The average single-particle composition agrees with the observed ensemble compositions but exhibits a large variation between individual particles. The ensemble techniques show that the average nanoparticle composition changes over time. The initial particles contain a higher fraction of Zn than those generated 30 minutes later. In-flight XPS spectra reveal that the relative signal from Zn and Cu on the particle surface follow a similar trend, see Figure 1.

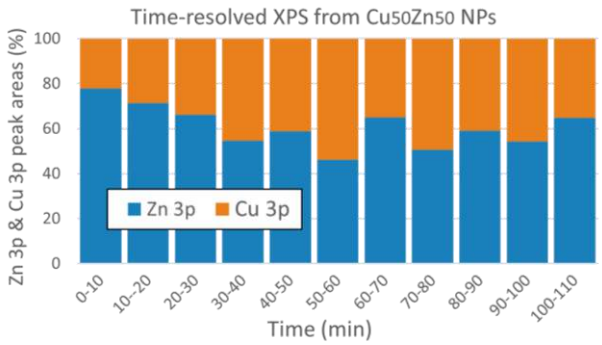

Figure 1. Indication of the relative amount of Zn and Cu on the NPs surface over time, captured by in-flight XPS. The NPs were generated using $Cu_{50}Zn_{50}$ alloys.

The ablation is of a dynamic character especially in the initial stage (~30 min) of NP production. Analysis of the plasma by OES confirms the preferred ablation of Zn over Cu during generation, though a steady state is reached with time. The feedstock composition from SEM-EDS shows a higher fraction of Cu after generation than that of the original, and the effect seems more pronounced for the cathode compared to the anode.

Using advanced characterization techniques, we reveal time-dependant dynamics in the generation of NPs using alloyed feedstocks containing elements with significant differences in vapor pressure and melting point. The new knowledge is essential for understanding and controlling particle generation using spark ablation.

This work was supported by the Swedish Foundation for Strategic Research (FFL18–0282), the Swedish Research Council (2019-04970 & 201904694), and the National Research, Development and Innovation Fund (Hungary, TKP2021-NVA-19).

Jönsson, L. et al. (2024) *J. of Aerosol Science.* **177**.
Tabrizi, N. S. et al. (2009b) *J. of Nanoparticle Research.* **11**(5), 1209-1218.

Time-Resolved Laser Diagnostics of Metal Cluster Formation from Spark Ablation

T. Krinke[1], V. Kornienko[2], M. Bermeo Vargas[1], M. Raveesh[2], Yupan Bao[2,3],
K. Deppert[1], A. Ehn[2], J. Bood[2], and M.E. Messing[1,4]

[1]NanoLund & Solid State Physics, Lund University, Lund, S-221 00, Sweden
[2]Combustion Physics, Lund University, Lund, S-221 00, Sweden
[3]Department of Mechanical and Aerospace Engineering, Princeton University, Princeton, USA
[4]Quantum Device Physics Laboratory, Chalmers University of Technology, S-412 96 Gothenburg, Sweden
Keywords: Spark ablation, nanoparticle formation, two-photon laser-induced fluorescence

Presenting author email: thomas.krinke@fysik.lu.se

Spark ablation has emerged as a versatile method for generating metal and metal oxide nanoparticles with controlled properties. When different electrode materials are employed, the resulting metal vapor plume provides a unique environment where mixing and alloying processes can occur at the earliest stages of particle formation (Kohut, 2025; Jönsson, 2024). Despite its relevance for nanomaterials synthesis, experimentally validated insights into vapor-phase mixing and cluster formation in such transient plasmas remain severely limited.

To investigate the earliest stages of metal cluster formation, we focus on the temporal evolution from the initial spark event to the appearance of the first atomic aggregates. In our approach, individual sparks are deliberately triggered, and the spatial distribution as well as the dynamics of neutral gold atoms (Au I) are examined directly following spark generation. This is achieved using femtosecond twophoton laser-induced fluorescence (TALIF) technique with structured illumination. Ultrashort laser pulses with precisely tailored spectral and spatial characteristics selectively excite gold atomic transitions, while the resulting fluorescence is recorded and analysed using a spatial lock-in detection scheme (Li, 2018). This method provides high temporal and spatial resolution, enabling us to capture transient atomic populations and transport processes that precede nucleation and early cluster growth.

Performing experiments on gold targets, our results show that the markedly different breakdown voltages of the carrier gases—air, nitrogen, and argon—have a strong influence on the post-spark expansion of the gold vapor. This highlights the critical role of the surrounding gas environment in governing the initial dispersion dynamics relevant to subsequent cluster formation.

Figure 1 shows two series of spatial distributions of gold vapor in air and argon, respectively. In air the spark generates a hydrodynamic shock wave that produces a characteristic toroidal structure, and the resulting “donut-shaped” vapor cloud expands at about 26 m/s. In this case, the breakdown voltage is approximately 8 kV. After about 350 µs, no gold vapor can be detected when the cloud has reached a maximum diameter of roughly 18 mm. Reducing the breakdown voltage under otherwise identical conditions by using nitrogen (4 kV) or argon (2 kV) results in a significantly slower expansion of the gold vapor cloud, and longer lifetime of the atomic species. In the case of argon as shown below, a markedly smaller final cloud size of about 10 mm in diameter is recorded after 1050 µs.

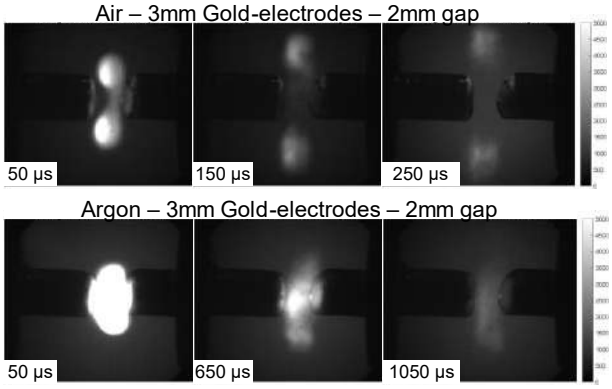

Figure 1.: Evolution of cloud of Au I – atoms in air (top) and Argon (bottom). Timestamps show elapsed time after the spark event.

The results of the quantitative TALIF analysis reveal a decrease in the concentration of individual gold atoms. Since the probed volume is well defined by the imaging data, this temporal evolution can be directly attributed to gas-phase nucleation, providing time-resolved experimental evidence of the initial stages of particle formation.

This work is supported by the Light and Materials profile area of Lund University and by NanoLund.

Jönsson, L. et. al., (2024) Journal of Aerosol Science, 177.
Kohut, A. et. al., (2025) Nanoscale Advances., 7, 3322-3330.
Li, Z. et. al., (2018) Combust. Flame, 192, 160-169.

SPES approach to characterizing nano-hetero-aggregates produced by spray synthesis

Philipp Rembe[1], Alfred Weber[1*], Pietro Vahramian[2], and Tiziano Sanvito[2+]

[1]Clausthal University of Technology, Institute of Particle Technology, 38678 Clausthal-Zellerfeld, Germany
[2]EOS S.r.l., Via Caianello 23, 20158 Milano (MI), Italy, [+]tiziano.sanvito@eosinstruments.com

Keywords: optical properties, single particle extinction and scattering, hetero-contacts

Presenting author email: philipp.rembe@tu-clausthal.de

Nanoparticles are widely used due to their special electronic, optical, and magnetic properties. Direct contact between nanoparticles of different materials can also result in new functionalities. The synthesis and properties of these hetero-aggregates are being intensively investigated as part of the German Research Foundation's Priority Program 2289 (Pokhrel et al. 2025). The use of a bipolar electrospray has proven to be a particularly versatile and effective synthesis method. In this process, the particles are generated in a spraying process, with the two sprays having opposite charges. The bipolar collision efficiency can be significantly increased by carefully selecting the droplet charge and spray geometry. Compared to the collision of neutral droplets, the coagulation frequency is increased by a factor corresponding to the product of the number of elementary charges of the two jets in a first approximation.

However, quantifying collision frequency remains difficult using direct measurement methods. Offline methods such as analytical electron microscopy enable accurate classification of hetero-aggregates, but they are costly and suffer from modest statistics. Therefore, a relatively new optical method was used in this study to determine the proportion of successful hetero-contacts. This method consists of single particle extinction and scattering (SPES) (Potenza et al., 2017). Information about particle size and refractive index is obtained from the temporal course of the forward scattering signal and lateral scattering. When plotting the scattered light signal against extinction, particles with the same optical properties but different sizes lie in a characteristic cloud. Applied to hetero-aggregates, this means that the respective individual components form such characteristic clouds, while true hetero-aggregates lie between them. A comparison of the total number of measured points and the points on the intermediate cloud then allows the proportion of hetero-aggregates to be determined.

In order to investigate the applicability of the SPES method to the determination of hetero-aggregates, different model particles were first produced using classical spray synthesis. At a later date, when the bipolar electrospray is fully operational, the SPES will be tested on it. Here a mixture of silica nanoparticles (Köstrosol) and iron nitrate nonahydrate (Sigma-Aldrich) solution in water was nebulized with a pneumatic atomizer and dried by passing a tube furnace. Particle size distributions were measured with a Scanning Mobility Particle Sizer. The dried particles were sampled on a heated filter for subsequent SPES measurements (EOS Classizer™ ONE) and TEM analysis.

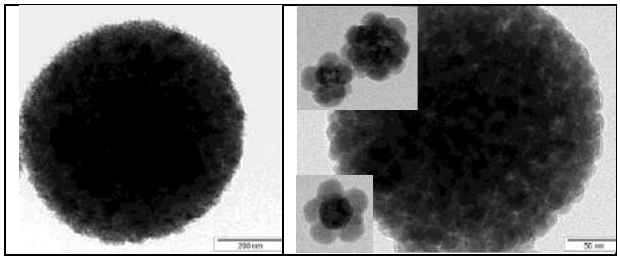

Figure 1. TEM micrographs: (left) pure SiO_2 aggregate (scale bar=200nm); (right) hetero-aggregates of SiO_2&Fe_2O_3 for SPES investigations (scale bar=50nm)

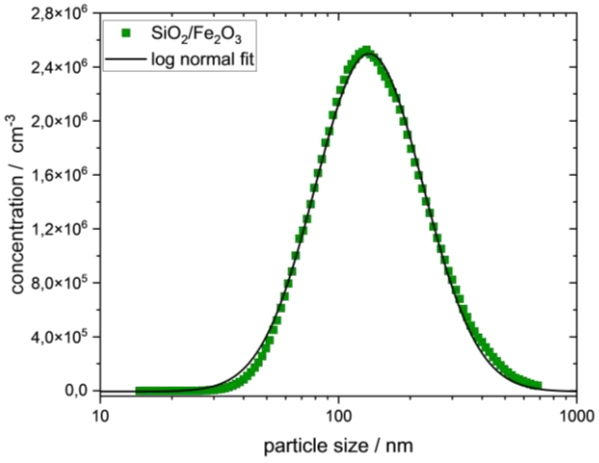

Figure 2. Mobility size distribution of model hetero-aggregates of SiO_2 and Fe_2O_3 measured with SMPS.

This work was supported by the German Research Foundation (DFG) under the grant WE 2330/30-2 within the Priority Program 2289 "Hetero-Aggregates".

Pokhrel, S. et al. (2025) KONA **42**, 170-187
Potenza, M. et al. (2017) Nanoscale **9**, 2778
EOS: https://www.eosinstruments.com/

Template-Free Tuning of Magnetic Nanoparticle Self-Assemblies through External Fields

Mehran Sedrpooshan[1,2], Alexander Omelyanchik[3,4], Pierfrancesco Maltoni[3,4], Davide Peddis[3,4], Adam M. Burke[1], Maria E. Messing[1,2], Rasmus Westerström[1]

[1]Department of Physics and NanoLund, Lund University, 118, 221 00, Lund, Sweden

[2]Department of Microtechnology and Nanoscience, Chalmers University of Technology, Gothenburg 412 96, Sweden

[3]Department of Chemistry and Industrial Chemistry & INSTM RU, nM2-Lab, University of Genoa, 16146 Genoa, Italy [4]Institute of Structure of Matter (ISM), nM2-Lab, National Research Council (CNR), 00015 Rome, Monterotondo Scalo, Italy

Presenting author email: mehranse@chalmers.se

Organizing magnetic nanoparticles (NPs) into hierarchical structures is a promising strategy for creating functional materials with anisotropic properties. In particular, linear nanochains (NCs) composed of magnetic NPs have attracted significant interest due to their potential applications in actuation, magnetically-responsive optical components, biomedicine, sensing, electromagnetic shielding, plasmonics, and catalysis. The functional performance of these systems critically depends on both the NC length and their spatial distribution, making controlled assembly a key challenge.

Conventional self-assembly approaches typically rely on colloidal suspensions subjected to external magnetic fields, either in solution or during deposition onto substrates. While these methods are simple and scalable, they often result in uncontrolled aggregation and densely packed chain bundles as the solvent evaporates, resulting in limited control over chain length and lateral spacing. Advanced strategies such as lithographic templating or patterned magnetic field gradients improve spatial control but significantly increase process complexity and reduce scalability.

Aerosol-based assembly provides an attractive solvent-free alternative, enabling continuous NP production and integration. However, magnetic-field-assisted aerosol assembly has so far suffered from similar limitations, frequently yielding large, poorly controlled chain bundles. Recent advances in electrically chargied aerosol particles have enabled precise control over particle deposition, suggesting new opportunities for tailoring magnetic NP assemblies without templates(1, 2).

In this work, we demonstrate a template-free aerosol-based approach for controlling both the average length and interchain spacing of magnetic nanochains (Figure 1 (a,b)). By tuning the ratio of applied electric and magnetic fields during the deposition of charged magnetic NPs, we achieve systematic control over nanochain morphology and spatial distribution as shown in Figure1 (c-e). This method preserves the simplicity and scalability of aerosol assembly while enabling a level of structural tunability not previously reported. Additionally, we investigate how the magnetic field profile influences chain formation and show that local out-of-plane magnetic field components play a crucial role in directing nanochains to assemble parallel to the substrate.

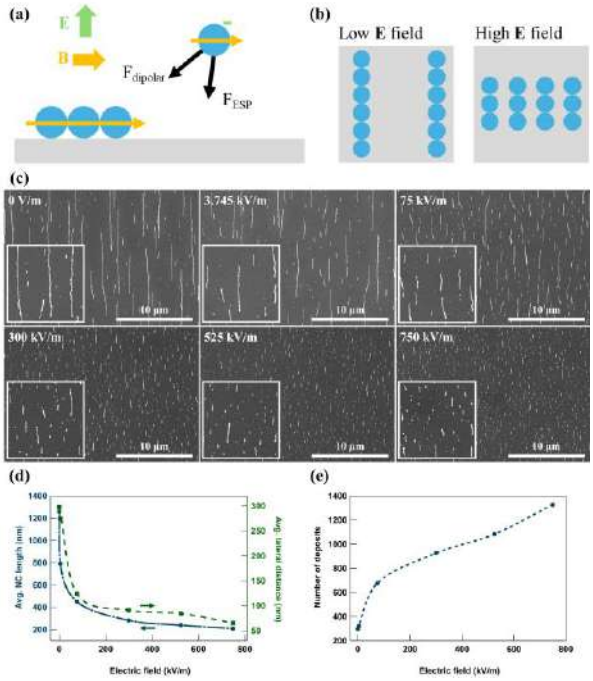

Figure 1. A simplified schematic of (a) electric (ESP) and magnetic (dipolar) forces upon nanoparticle deposition and (b) NCs deposited under low and high E fields. (c) SEM images of NCs deposited under different E fields. (d) average length and lateral separation, and (e) number of separate structures per E field.

This work was supported by European Union's H2020 MSCA (Grant No. 945378) (GenerationNano), the Swedish Research Council (Grant No. 2019-04970), the Swedish Energy Agency (Grant No. 50689-1), the Crafoord Foundation, and NanoLund, Lund Nano Lab-Myfab.

1. Preger C, Josefsson M, Westerström R, Messing ME. Bottom-up field-directed self-assembly of magnetic nanoparticles into ordered nano-and macrostructures. Nanotechnology. 2021;32(19):195603.

2. Sedrpooshan M, Bulbucan C, Ternero P, Maltoni P, Preger C, Finizio S, et al. Template-free generation and integration of functional 1D magnetic nanostructures. Nanoscale. 2023;15(45):18500-10.

Forced charge transfer to nanoparticles in particle-wall collisions to produce functional hetero-aggregates

Alexander Plack[1*] and Alfred P. Weber[1]

[1]Clausthal University of Technology, Institute of Particle Technology, 38678, Clausthal-Zellerfeld, Germany

Keywords: nanoparticle mechanics, work function, surface potential.

Presenting author email: alexander.plack@tu-clausthal.de

Efficient charging of aerosol nanoparticles is a challenging task. The diffusional attachment of gas ions is mostly limited to one or two elementary charges and suffers from low charging efficiency, which is further reduced with decreasing particle size. Higher charging levels may be attained by using elaborate photoemission setups which, however, limit, both the polarity and the efficiency. Here, a new method is presented to charge nanoparticles in a controlled and uniform way by employing particle-wall collisions. It consists of low pressure impaction of nanoparticles onto a wall with an applied voltage. The charge of the rebounding particles can be controlled by the impaction velocity and by the applied voltage. In this way, negative, neutral, and positive particles can be obtained for any nanoparticle material. The technique has an analytical side and an application side. Since the charge transfer depends on the difference in the work functions of the particle and the wall, the corresponding effective work function can be deduced from the charge of the rebounding particles. This is the first method to measure the particle work function during ultrashort stressing events such as impaction, which lasts only a few tens of picoseconds. On the other hand, by using two inclined impaction plates, two oppositely charged aerosol jets can be directed against each other.

The transferred charge q during collision can be described with the condenser model (Javadi et al. 2024),

$$q = k_c\, C\left(d_p, v_i\right)\left(\frac{\phi_p - \phi_w}{e} + \gamma\, V_{ex}\right) \qquad (1)$$

where k_c is the charge transfer coefficient, C is the capacitance of the particle-wall contact system (C prop. to the contact area S), e is the elementary charge, and ϕ_p and ϕ_w are the work functions of the particle and the wall, respectively (see Eq. (1)). The external voltage applied to the wall is given as V_{ex}. By varying V_{ex}, the particle charge after rebound can be adjusted from negative, to neutral, and to positive. The coefficient γ accounts for the electric field strength, i.e. it reflects the distance to the next grounded electrode. The capacitance C depends on the contact area which in turn is determined by the particle size d_p and the impaction velocity v_i. The impaction velocity in a low pressure impactor is calculated according to Rennecke and Weber (2013). In Fig. 1 it is shown how the charge of rebounding Cu NP can be adjusted with the applied voltage. The current measured with a Faraday Cup Electrometer (FCE) is proportional to the particle charge when particle losses are neglected. Such losses are indeed observed since the current does not scale linearly with the voltage as expected from Eq. (1).

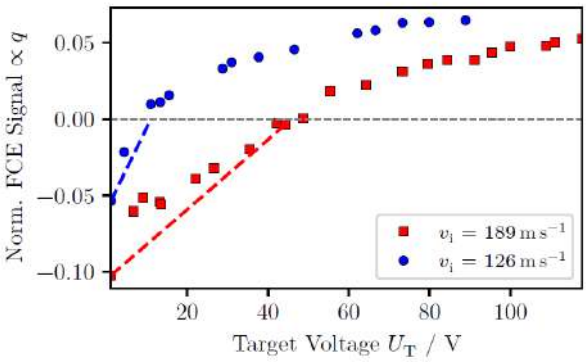

Figure 1. Influence of applied voltage on charge of impacting Cu NP on an Au target.

It becomes clear that by adjusting the applied voltage V_{ex} (U_T in Fig. 1) the two particle jets (see Fig. 2) can be given opposite charges, which greatly enhances the probability of mutual collisions between different aerosol particles A and B. In fact, the collision probability β_{AB} scales with $\beta_{AB} \propto n_A\, n_B$, where n is the number of elementary charges of A-particles ($q_A = n_A\, e$) and B-particles ($q_B = n_B\, e$).

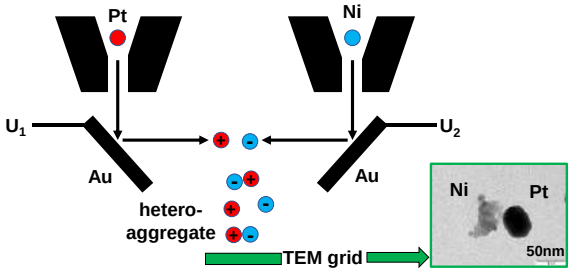

Figure 2. Schematic setup of the two-jet system to produce hetero-aggregates, the TEM micrograph shows an example of a Ni-Pt-hetero-aggregate obtained.

This work was supported by the German Research Foundation (DFG) under grant WE 2330/30-2 within the Priority Program 2289 "Hetero-Aggregates".

Javadi, M. et al. (2024) Chem. Ing. Tech. **96**, 950-957

Rennecke, S. and Weber, A.P. (2013) *J. of Aerosol Science.* **55**, 89-103

Cone-Jet Stability and Surface Morphology of Electrosprayed Titania Films

A. Parisi[1], R. Griffo[2], C. Carotenuto[2], and F. Di Natale[1]

[1]Department of Chemical, Material and Industrial Production Engineering, University of Naples Federico II, Naples, 80125, Italy

[2]Department of Engineering, University of Campania "L. Vanvitelli", Aversa, 81031, Italy

Keywords: electrospray deposition, titania films, cone-jet stability, energy applications, surface morphology

Presenting author email: arianna.parisi@unina.it

Titanium dioxide (TiO_2) thin films have demonstrated great versatility and suitability in several technological areas, from photocatalysis and solar cells to protective coatings and gas sensors, as well as for biosensor interfaces. TiO_2 particles can also be functionalized with other precious metals, like gold, through a process like photochemical deposition or nanoparticle integration, allowing charge separation, plasmonic effects, and extension of the absorption spectrum. It was understood that the surface architectural arrangements of thin films at the micro- and nanoscale play an important role in their functional behaviour, together with the stability, photoactivating properties, and electronic configuration of primary TiO_2 particles.

Electrospray deposition provides an emergent approach for the scalable synthesis of nanostructured films of titania with controlled morphologies. In the technique, the colloidal suspension of TiO_2 particles within an electrolytic solution is electrostatically sprayed within an electric field to create a charged cone-jet current, producing a spray of micrometric droplets of the suspension. When droplets evaporate, nanometric clusters of TiO_2 particles form. Unlike other deposition methods, electrospray offers precision in size selection of particles and droplets while reducing material losses during the process and providing room-temperature synthesis over various substrates.

In the combined process of droplet formation, solvent evaporation, and cluster assembly during flight, the resulting morphology of the formed films can be controlled. By fine-tuning of process parameters, such as applied voltage, liquid flow rates, needle-collector spacing, and electrode configurations – conventional mode, inverse conventional mode, induction mode, and bipolar mode – precise control of film thickness, morphology, and surface area can be attained.

This work presents a thorough mapping of the electrospray stability domains for TiO_2 suspensions over a broad range of operating parameters and electrode configurations (Figure 1). The stability diagrams verify that cone-jet formation is mainly controlled by the electric field at the liquid meniscus, with needle-collector spacing, electrode polarity, and induction having a role in stability.

Scanning Electron Microscopy shows that film morphologies vary from dense structures of granules to highly porous structures of "cauliflower type". The broad cone-jet regions yield uniform and mechanically strong films if operated in their cone-jet mode, but porous and thinly formed films result if operated near cone-jet stability boundaries.

Wettability measurements reveal apparent superhydrophilicity for all films, with spreading dynamics strongly dependent on the electrospray configuration. Conventional-mode coatings exhibit ultra-fast spreading, consistent with highly porous and loosely packed morphologies. Films fabricated in inverse and induction modes show slower contact-angle dynamics and partial surface instability during wetting, associated with intermediate microstructures. In contrast, bipolar-mode films combine complete wetting with enhanced mechanical robustness, enabled by a more compact and interconnected architecture. The work demonstrates how cone-jet stability maps enable rational tuning of electrospray conditions to control film morphology and functional surface properties for photocatalysis, sensing, and energy applications.

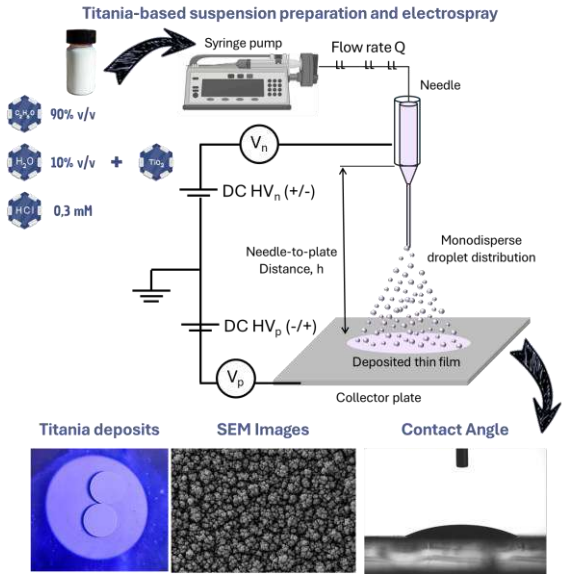

Figure 1. Electrospray deposition: experimental setup, film morphology, and wettability.

Tang, J., & Gomez, A. (2017). *Aerosol Sci. Technol.*, 51(6), 755–765.

Castillo, J. L., Martin, S., Rodriguez-Perez, D., Higuera, F. J. and Garcia-Ybarra, P. L. (2018). *J. Aerosol Sci.* 125, 148-163.

Cone-Jet Mode in Bipolar Electrosprays

J.L. Castillo[1], A. Parisi[2], S. Martin[1] and P.L. Garcia-Ybarra[1]

[1]Departmento de Fisica Matematica y de Fluidos, UNED, Las Rozas de Madrid, 28232, Spain
[2]Dipartimento di Ingegneria Chimica, dei Materiali e della Produzione Industriale, Università degli Studi di Napoli Federico II, Naples, 80125, Italy
Keywords: electrospray, cone-jet mode, liquid atomization, particle deposits.

Presenting author email: jcastillo@ccia.uned.es

Electrospraying liquid suspensions is a trustworthy method to get aerosolized particles with precluded size and composition. This technique can be employed for surface coating or thin film applications (Castillo *et al*, 2014) where the required result is the formation of granular deposits with tailored morphologies (porosity and surface roughness) and a narrow range in the size of the building blocks.

The atomization of the liquid by electrospray arises from the ejection of a suspension from a needle in the presence of a strong electric field at the needle tip. Under suitable conditions, the electrospray remains stable in the so-called cone-jet mode with a liquid cone anchored at the needle rim and a thin jet emerging from the cone tip to steadily accommodate the prescribed liquid flow rate. Downwards, the emitted jet breaks up generating a cloud of almost monodisperse charged tiny liquid droplets drifted by the electric field and the solid residue (after liquid evaporation in the droplet) may be collected on a plate facing the needle.

The classical electrospray configuration consists of an electrified needle (kept at a constant voltage, $V_{n,0}$) and a grounded plate ($V_p = 0$). Then, for a given needle-plate distance, there is a stability island (in the needle voltage-flow rate parameter space) where a steady cone-jet is achieved. However, there is a maximum flow rate beyond which this steady mode cannot be maintained.

A bipolar electrospray adds an additional degree of freedom to the system by applying a voltage to the plate (V_p usually opposite to the needle voltage). Thus, the voltage drop is increased as well as the efficiency of the collection of the charged particles. This dual voltage configuration allows the extension of the cone-jet mode to even larger flow rates.

In the case of an "ideal" bipolar electrospray with an infinitely large collector plate facing the needle, the needle set to a voltage V_n and the plate at a different voltage V_p, both electrically isolated from the rest, the voltage difference $(V_n - V_p)$ (irrespectively of the particular values of V_n and V_p) will play the role of $V_{n,0}$ in the case of a grounded plate. That is, the results for the grounded plate will be directly transferable to the "ideal" bipolar electrospray, just changing $V_{n,0}$ by $(V_n - V_p)$. However, this is not the case in a "real" bipolar electrospray due to the influence of other grounded elements in the setup which affect the electrical field at the needle exit.

In the present study (Parisi *et al*, 2026) the stability domain is completed by investigating all the possible combinations of the polarity of the applied voltages. Even when the voltage polarity of the support is the same as the needle voltage polarity, for not too large plate voltages, the electric field still brings some particles to the support. Whereas when the magnitude of the plate voltage increases the charged droplets are deviated by the local electric field in the vicinity of the plate and the particles are no longer collected there. The influence of the needle-substrate distance on the electrospray cone-jet stability domain and the efficiency in the collection of the electrosprayed particles (even in the case of substrates with the same voltage polarity as the needle voltage) are analyzed.

The results show a significant impact of the needle-to-plate distance on the cone-jet mode stability domain affecting the maximum flow rate achieved in this mode. Additionally, the polarity of the voltages applied to the needle and the collector plate have a large impact on the particle collection efficiency. By integrating stability domains at different needle-to-plate distances and voltage polarities, complex interactions among these factors are elucidated, and an extended stability domain is obtained. Overall, the study offers valuable insights for optimizing electrospray processes for nanoparticle suspensions and depositions, with potential applications in preparation of layered materials.

This work was supported by the Spanish Research Agency, MCIN/AEI / 10.13039/501100011033. Ministerio de Ciencia, Investigación y Universidades (Spain), under project, PID2022-139082NB-C55, partially supported by European Regional Development Funds (ERDF).

Castillo, J. L., Martin, S., Rodriguez-Perez, D., Higuera, F. J., Garcia-Ybarra, P. L. (2018) *Journal of Aerosol Science*, **125**, 148–163.

Parisi, A., Martin, S., Garcia-Ybarra, P.L., Castillo, J.L. (2026) *Journal of Aerosol Science* (under preparation).

Controlled Morphology of Microparticles Formed by Evaporation of Aerosol Droplets Containing Nanoparticles with Varying Glass Transition Temperatures

S. K. Haughton[1], P. Georgiou[2], L.K. Mahato[1], F. Crawford[1], S, P. Armes[2], and J. P. Reid[1]

[1]School of Chemistry, University of Bristol, Bristol, BS8 1TS, UK
[2]Department of Chemistry, University of Sheffield, Sheffield, S3 7HF, UK
Keywords: supraparticles, evaporation, nanoparticles, polymers, glass transition temperature

Presenting author email: sorrel.haughton@bristol.ac.uk

Final morphology of spray-dried microparticles is an important factor in determining the particle's chemical and physical properties, which in turn is important for particle design in applications such as spray-dried pharmaceuticals, cosmetics and food products. The morphology of the dried particle governs its surface area and density, which in turn affects the suitability for application; for example, low density particles are useful for inhaled drug formulations.

Aerosol assisted self-assembly of aqueous, nanoparticle-laden droplets allows this control over the final morphology. However, current literature focusses on sessile or pendant microliter sized droplets, rather than the free, picolitre droplets most commonly seen in spray-dryers (Liu *et al*, 2022), (Thybo *et al*, 2008). The studies that do use free droplets mainly study the impact of the surrounding gas phase, rather than internal effects such as the hardness of the nanoparticle. In this work the evaporation of free, picolitre sized droplets was probed using an electrodynamic balance (EDB), scanning electron microscopy (SEM) and atomic force microscopy (AFM). The effect of relative humidity (RH) and the nanoparticle's mechanical strength on the final microparticle's morphology was investigated using four monodisperse nanoparticle samples with glass transition temperatures (T_g) ranging from -30.4 °C to 93.3 °C. These four samples provide a direct comparison of the effect of RH and T_g on the nanoparticle packing and shell formation during the drying of colloidal droplets.

Figure 1 shows that decreasing the RH led to increased evaporation rate and buckling in the final nanoparticles. At these dilute concentrations the nanoparticles' properties had no impact on the evaporation kinetics, but decreasing the T_g of the nanoparticles led to softer dried particles which exhibited a greater degree of buckling. The AFM results (Figure 2) confirm this, showing an increase in the Young's modulus of the supraparticle surface as T_g was increased. The AFM also showed that the nanoparticles merged at low T_g, and voids formed in the soft surface. In comparison, the particles comprised of the high T_g nanoparticles show distinct, separate nanoparticles on the surface. These results show that the Young's modulus of the nanoparticle affects the strength of the resulting dried microparticle, which in turn affects the morphology. This signifies a move towards increased control over a microparticle's final morphology.

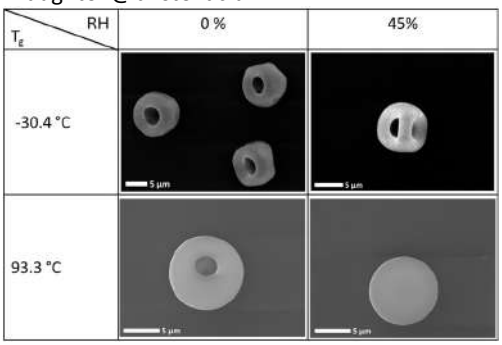

Figure 1. SEM images of dried microparticles formed from the evaporation of aerosol droplets containing nanoparticles with two different glass transition temperatures at 0% and 45% RH.

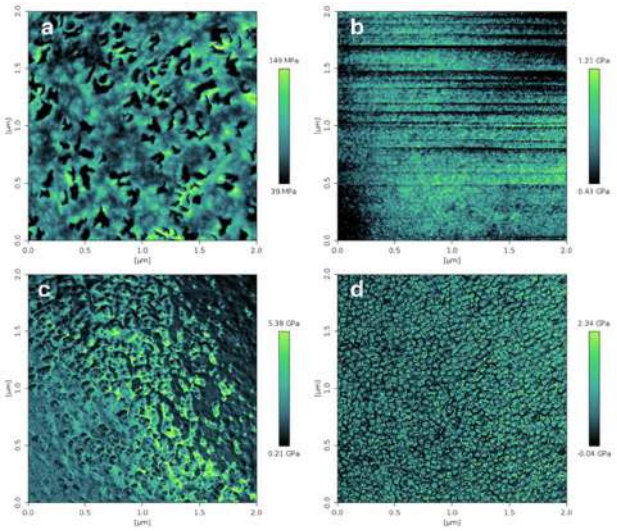

Figure 2. AFM images showing the Young's modulus of the surface of supraparticles made up of nanoparticles with a glass transition temperature of a) -30 °C b) 12 °C c) 52 °C and d) 93 °C. The particles were formed at 0% RH.

This work is supported financially by, EPSRC CDT in Aerosol Science (EP/S023593/1), EPSRC (EP/W022206/1, EP/W022214) and Future Formulation (EP/N025245/1).

Nandiyanto and Okuyama (2011) *Advanced Powder Technology*, **22**, 1-19.
Liu *et al* (2022) *Journal of Colloid and Interface Science*, **607**, 1661-1670
Thybo *et al* (2008) *Pharm Dev Technol*, **13**, 93-104
Miles *et al* (2024) *Langmuir.* **40**, 734-743.

Electro-Assisted Flow Blurring for High-Throughput Generation and Charging of Newtonian Droplets

L. Modesto-López[1] & A. Gañán-Calvo[1,2]

[1]Department of Aerospace Engineering and Fluid Mechanics, Universidad de Sevilla, Sevilla, 41092, Spain
[2]Laboratory of Engineering for Energy and Environmental Sustainability, Universidad de Sevilla, 41092, Spain
Keywords: Flow Blurring; pneumatic atomization; electrostatic charging; droplet breakup; high-throughput sprays.

Presenting author email: Lmodesto@us.es

Aerosol processes for materials manufacturing, spray transport, and interfacial studies require droplet generators that combine high liquid throughput with predictable breakup and tunable droplet size distributions. Flow Blurring (FB) atomization (Gañán-Calvo, 2005) is an energetically efficient pneumatic technique that produces fine sprays and remains robust as liquid flow rates increase as depicted in Figure 1 (Hermosín-Reyes, 2019; Serrano, 2019). In contrast, electrical control of droplets, desirable for enhanced dispersion, deposition, steering, and charge-driven collection, is often implemented via electrohydrodynamic (EHD) atomization at the expense of strongly reduced throughput.

Here we investigate electro-assisted Flow Blurring (E-FB) as a modular strategy that separates droplet formation from electrical manipulation (Modesto-López, 2019, 2022, 2023). The approach couples an FB atomizer operating in its established droplet-dominated regime with downstream electrode-assisted charge injection, aiming to impart charge while preserving FB breakup dynamics. The study focuses on low-viscosity Newtonian liquids, selected to cover a broad range of electrical conductivity and to evaluate charging performance under realistic aerosol-processing conditions.

Primary breakup near the outlet is characterized by high-speed imaging, and droplet populations are quantified through volume-based size distributions obtained from image-based droplet sizing. Electrical behavior is assessed from spray and collector current measurements under controlled voltages, enabling estimation of charge transfer stability. The FB operation is explored by varying the gas-to-liquid mass ratio (GLR) as a governing parameter for droplet size. Increasing GLR yields a systematic reduction in characteristic diameters, consistent with FB droplet-regime trends and providing a well-defined baseline for electrical manipulation.

Across the tested liquids, E-FB achieves stable charge injection over wide conductivity conditions, from low-conductivity ethanol to conductive aqueous solutions, including acid-doped water, without indications of a transition to EHD-dominated breakup. Size distributions and near-nozzle observations show that electrostatic assistance enhances dispersion and electrical addressability while maintaining the FB droplet formation pathway, indicating that electrical forcing acts predominantly downstream of breakup. Importantly, liquid flow rates from sub-mL/min up to several tens of mL/min are sustained, enabling electrically controllable Newtonian droplet aerosols at throughputs far beyond typical EHD operation.

E-FB provides a scalable platform with independent tuning of droplet generation via GLR and electrical charging conditions for applications such as electrostatic spraying, targeted deposition, and electrically assisted aerosol diagnostics.

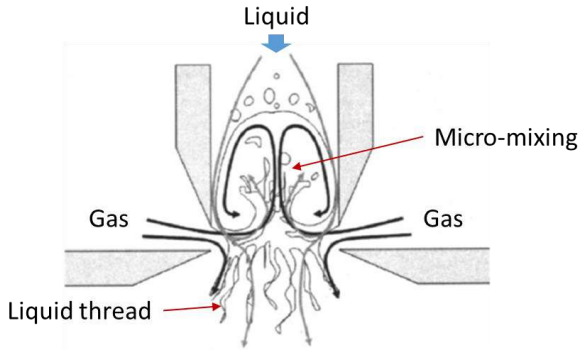

Figure 1. Schematic cross-section of typical FB device.

This work is part of project PID2022-140951OB-C21 financed by MCIN/AEI/10.13039/501100011033.

Gañán-Calvo, A. M. (2005) Appl. Phys. Lett. 86, 214101.
Hermosín-Reyes, M. et al. (2019) J. Aerosol Sci., 137, 105429.
Modesto-López, L. et al. (2019) ACS Omega 4(2), 2693-2701.
Modesto-López, L., and Olmedo-Pradas, J. (2022) ACS Omega, 7(15), 12549-12555.
Modesto-López, L., and Gañán-Calvo, A. M. (2023) Sci. Rep. 13, 12639.
Serrano, J. et al. (2019) Energy 168, 737-752.

Evaporation kinetics and dried microparticle morphology of aqueous aerosol droplet containing nanoparticles

Lukesh K. Mahato[1], Panagiotis Georgiou[2], Barnaby E. A. Miles[1], Sorrel K. Haughton[1], Spyridon Varlas[2], Rachael E. H. Miles[1], Steven P. Armes[2] & Jonathan P. Reid[1]

[1]School of Chemistry, University of Bristol, Bristol, BS8 1TS, UK
[2]Department of Chemistry, University of Sheffield, Sheffield, S3 7HF, UK
Keywords: Evaporation, Aerosol droplet, Agglomeration, Nanoparticle.

Presenting author email: J.P.Reid@bristol.ac.uk

Understanding the agglomeration of nanoparticles through evaporation-induced assembly is a key process, highly desirable for manufacturers in powder technology, such as those in pharmaceuticals, food products, cosmetics, and fine chemicals. Predicting the morphology of the dried agglomerate particles can also facilitate understanding of the dried particle's optical properties and mechanical strength. Typically, morphology is influenced by the drying conditions and the diffusional properties of the nanoparticles. The drying conditions can be altered by varying relative humidity and temperature, and diffusional motion is affected by temperature, nanoparticle size and the viscosity of the liquid droplet (Mahato et al. 2025).

In this study, we investigate aerosol droplet of 25 µm initial radius with particle evaporating down to 3-7 µm radius. For that, we evaporate aerosol droplets containing monodisperse or bi-disperse copolymer nanoparticles of different sizes, glass transition temperatures and shapes, at a relative humidity (RH) between 0 and 45% and a temperature of 21ºC. We obtained the dried agglomerate microparticles using the falling droplet column (FDC) technique. Additionally, we use the electrodynamic balance (EDB) to measure the evaporation rate of the drying colloidal aqueous aerosol droplet. To prepare the sterically stabilized diblock copolymer nanoparticles of desired sizes (32 to 238 nm) and shapes, we used the polymerization-induced self-assembly (PISA) technique (miles et al. 2023).

We observe that as the evaporation rate (*K*) increases, the degree of buckling of dried agglomerate microparticle increases (i.e. the shape transitions from spherical to deformed to dimpled to donut shapes), consistent with changes in the commonly used Peclet number (*Pe*) for explaining the dried microparticle morphology. Moreover, the degree of buckling of dried microparticle increases with increases in the diffusional motion of the nanoparticles while keeping *K* constant. A similar observation is found for a binary mixture of nanoparticles (Figure 1). Among the tested nanoparticle shapes (spherical, worms, vesicles, and crosslinked vesicles) the degree of buckling is higher for spheres than for worms, vesicles, and cross-linked vesicles when the mass of nanoparticles in each droplet is kept constant. The degree of buckling is enhanced with *K* for all the tested shapes of nanoparticles, similar to both monodisperse and bidisperse nanoparticles. Interestingly, wrinkle-shaped supa-particles are formed with the vesicles and cross-linked vesicles nanoparticles.

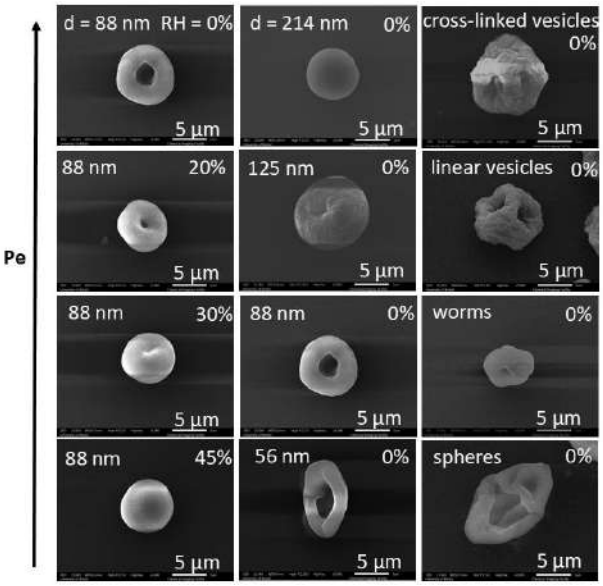

Figure 1. Dried agglomerate particles obtained after the evaporation of aqueous aerosol droplet containing nanoparticles. Left, middle, and right columns represent nanoparticles of same size drying at different RH, different size at same RH and different shapes at same RH, respectively. d denotes average nanoparticle diameter.

This work is supported financially by EPSRC (EP/W022206/1, EP/W022214), EPSRC CDT in aerosol science (EP/S023593/1), and Future Formulation (EP/N025245/1).

Mahato L.K., Varlas S., Miles B.E., Chan D.H., Hardy D.A., Eloi J.C., Harniman R.L., Miles R.E., Armes S.P. and Reid J.P. (2020) *Journal of Colloid and Interface Science* **682**, 251-262.

Miles B.E., Chan D.H., Varlas S., Mahato L.K., Archer J., Miles R.E., Armes S.P. and Reid J.P. (2023) *Langmuir* **40(1),** 734-743.

Nanoparticulate Coatings by Electrospray

D. Parajuli[1], P. Martínez-Cánovas[1], A. Oulad-Ali[1], E. Bodnár[1], Y. Pérez [1], R. Garcia-Valls[1], S. Satarova[2], V. Bloemen[2], K. Moreira[3], L. Agostinho[3], N. Sochorakis[1], and J. Rosell-Llompart[1,4]

[1]Department of Chemical Engineering, University Rovira i Virgili, Tarragona, E-43007, Spain
[2]Department of Materials Engineering, KU Leuven, Leuven, B-3000, Belgium
[3]Lectoraat Water Technology, NHL Stenden, Leeuwarden, 8917 DD, The Netherlands
[4]Catalan Institution for Research and Advanced Studies ICREA, Barcelona, E-08010, Spain
Keywords: electrospray, polymer, coating, nanoparticles, deposition.

Presenting author email: joan.rosell@urv.cat

The electrospray (ES) route to make particles and thin coatings is now well established but its advantages have not been appreciated enough by industrial sectors that could benefit from it. Here, we present an overview of our past to very recent work on the formation of nanoparticulate continuous coatings by ES, connecting the morphologies to underlying physics mechanisms, solute-solvent systems, and configurations.

ES generates electrically charged droplets through formation of a Taylor-cone, jet emission, and jet breaking up into primary and secondary droplets (Rosell-Llompart *et al.*, 2018). The droplets transform into solid structures (Bodnár *et al.*, 2018) while following non-overlapping trajectories, usually with negligible inertia. The structure of the films depends on different factors, as analyzed by Higuera (2018) among others.

The non-crossing nature of electro-phoretic trajectories is dramatically revealed in mutually excluding deposition spots from multiple simultaneously operating spray needles (Sochorakis, 2018). However, for electrically insulating particulate films, charge accumulates on the growing deposit, leading to a progressive expansion of the spray plume and deposition spot (Fig. 1a,b). Additionally, electric micro-discharges are encountered during prolonged deposition of EC at low ambient humidity.

Electrospraying suspensions of insulating PTFE nanoparticles yields locally-uniform particulate layers that can be sintered into continuous hydrophobic films, including on highly curved substrates such as capillary needles (Fig. 1c). Titania nanoparticulate beds formed by electrospraying of an organometallic precursor are highly uniform over large areas; however, fractures are observed under certain conditions, the origin of which still remains unresolved (Fig. 1d). Cross-linked chitosan nanoparticles made by coaxial electrospraying form fractal (cauliflower-like) deposition patterns (Fig. 1e). Electrospraying low-concentration EC solutions at high ambient humidity resulted in continuous wet deposition forming Breath Figures (Fig. 1f).

Finally, electrospray deposition of polyvinyl-pyrrolidone (PVP) microparticles is applied to complex, non-conductive, 3D architectures, including melt-electrowritten polymer scaffolds, illustrating the power and flexibility of the method.

Overall, these results highlight how aerosol generation, charged cloud transport, and deposition are closely coupled and should be considered together when designing ES droplet and particle-based coating processes. From an aerosol and particle technology perspective, this work highlights electrospray as a powerful physically guided route towards particulate and continuous nanoparticulate coatings with controlled and predictable morphology.

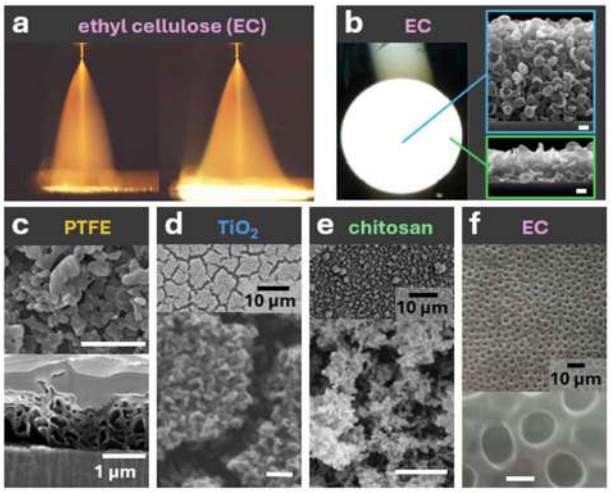

Figure 1. (a) Electrospray spray plume time evolution, (b) deposition spot, and (c-f) deposition patterns.

This work was supported by the Spanish Government and EU's ERDF and by the Catalan Government under various grants, including PID2021-129064NB-I00 and 2021SGR-00978.

Bodnár, E., Grifoll, J., Rosell-Llompart, J. (2018) *J Aerosol Science.* **125**, 93-118.
Higuera F.J. (2018) *J Aerosol Sci.* **118**, 45-58.
Rosell-Llompart, J., Grifoll, J., Loscertales, I.G. (2018) *J Aerosol Science.* **125**, 2-31.
Sochorakis, N. (2018) PhD thesis. Universitat Rovira i Virgili. hdl.handle.net/10803/664720

Nucleic acid-marked nanoplastics produced by electrohydrodynamic atomization (EHDA) for applications in water technology

K. S. Moreira[1*], C. Soppe[1,2], Y. Nauta[1,2], N. Sochorakis [3] , A. P. Fuchs [4] , L. L. F. Agostinho[1]
[1]Lectoraat Water Technology, NHL Stenden, Leeuwarden, 8917 DD, The Netherlands
[2]Van Hall Larenstein, Leeuwarden, 8934 CJ, The Netherlands
[3]ReCover ltd, Nicosia, 2121, Chipre
[4]Carinthia University of Applied Sciences, Klagenfurt, 9020, Austria

Keywords: Electrospray, Marked nanoparticles, Nucleic acid, Nanoplastics ,PCR-LAMP

Presenting author email: kelly.schneider.moreira@nhlstenden.com

Environmental nano- and microplastics (NMPs) are highly diverse, making their detection and risk assessment challenging. Nanoplastics are particularly hard to study due to absent commercial standards and poor compatibility with naturally degraded fragments (Sousa V. S., Teixeira, M. R., 2020). Metal-doped NMPs have been used for detection, but their low metal content limits sensitivity. In contrast, nucleic acid detection methods like PCR and LAMP, which advanced during the COVID-19 pandemic, offer high sensitivity in compact formats. Doping NMPs with nucleic acids provides a promising strategy to improve nanoplastics research via PCR-LAMP detection.

In this work, we employed Electrohydrodynamic Atomization (EHDA) also known as electrospray (Agostinho, L. L. F. et al, 2018), to produce nucleic acid-marked micro/nanoplastic particles (NMPs), enabling their detection through PCR-LAMP technology.

The particles were produced via coaxial electrospray (Figure 1), which is a technique that uses two concentric nozzles to allow two liquids to be sprayed simultaneously. The inner solution contains the traceable E.Coli DNA while the outer solution comprises of the polymer polystyrene.

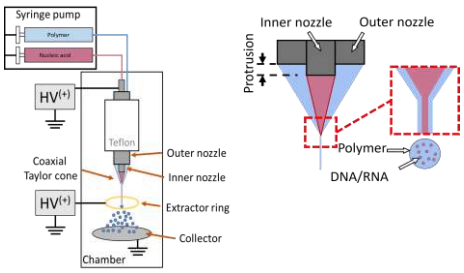

Figure 1 - Coaxial EHDA setup.

The particle characterization and detection was done using Scanning Electronic Microscopy and Energy Dispersive X-ray spectroscopy (SEM-EDX). For the PCR analysis, the OmniLAMP® device developed by *Visuri* will be used for the PCR-LAMP testing to detect nucleic acid-marked nanoplastics.

For the particle production, key setup parameters, such as inner and outer solution flow rates, collection time, EHDA nozzle-to-collector distance, and applied potential, were varied. Figure 2 shows particles produced using the most stable coaxial configuration and the LAMP-PCR reaction results after amplification. In the presence of target DNA, amplification caused a color change from pink to yellow.

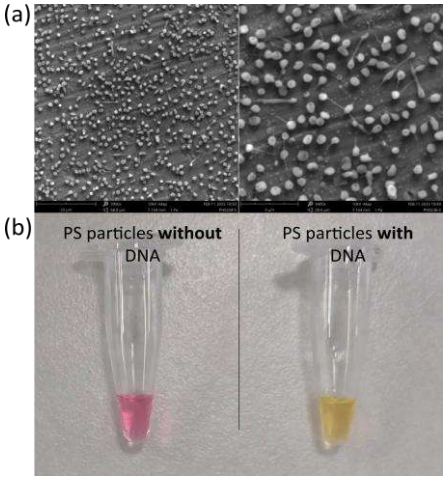

Figure 2 - (a) SEM images of produced NMPs. (b) LAMP-PCR reaction tubes after amplification.

The coaxial EHDA system successfully produced well-dispersed PS microparticles marked with DNA, with diameters ranging from 1 to 2 µm. Importantly, the DNA-marked particles were readily detectable using LAMP-PCR technology. By using DNA as a molecular tracer, these particles, combined with LAMP-PCR detection methods, can support the development of innovative analytical tools for monitoring and removing NMPs in wastewater treatment systems and environmental settings.

This work was conducted with the financial support of SIA Regieorgaan.

Sousa V. S., Teixeira, M. R., (2020) Sci. Total Enon. 707, 136077.
Agostinho, L. L. F. et al. Journal of Aerosol Science, v. 125, p. 237–250, 1 nov. 2018.

Wet Electrostatic Scrubbing for fine and ultrafine particulate matter control in industrial and engine exhausts

A. Parisi[1], L.P. Di Bonito[1], C. Carotenuto[2] and F. Di Natale[1]

[1]Department of Chemical, Material and Industrial Production Engineering, University of Naples Federico II, Naples, 80125, Italy
[2]Department of Engineering, University of Campania "L. Vanvitelli", Aversa, 81031, Italy
Keywords: Fine and ultrafine particles, Pollution Control, Gas cleaning technique.

Presenting author email: francesco.dinatale@unina.it

Fine ($PM_{2.5}$) and ultrafine particulate matter (UFP, <100 nm) emissions remain a critical issue for air quality management in both stationary industrial sources and mobile applications. Due to their small size, low inertia, and strong coupling with the carrier gas, these particles are particularly difficult to remove using conventional abatement technologies based solely on inertial impaction, filtration, or Brownian diffusion (Hinds, 1999).

As emission regulations become increasingly stringent, shifting from mass-based limits to particle number control and extend toward ultrafine size ranges, there is a growing need for advanced and adaptable particle control solutions.

This work aims to present Wet Electrostatic Scrubbing (WES) as a flexible and scalable electro-hydrodynamic technology for the removal of fine and ultrafine particles and to illustrate its applicability through representative examples spanning different industrial sectors and engine exhaust treatment.

WES combines the intrinsic robustness of wet scrubbing with electrostatic enhancement by introducing electrically charged droplets and/or ionization of the gas phase within the contact chamber. The resulting electric fields promote particle capture through Coulombic attraction, image-charge forces, and dielectrophoretic effects, significantly increasing particle-collector collision probabilities, particularly in the submicron size range where conventional wet scrubbers and fabric filters are less effective.

The study discusses the application of WES to industrial flue gas treatment, including combustion-based processes, metallurgical operations, and chemical plants. In these contexts, WES has demonstrated high removal efficiencies for $PM_{2.5}$ and UFP while maintaining low pressure drops and operational stability under high temperatures, variable gas compositions, and elevated particulate loadings. The liquid phase enables stable particle capture and washout, while also allowing the simultaneous absorption of soluble gaseous pollutants. These characteristics make WES particularly suitable for retrofitting existing wet scrubbers and for installations where dry electrostatic precipitators or high-efficiency filters may face operational or economic constraints (Parisi et al., 2025).

Further examples address the promising use of WES for the treatment of exhaust gases from internal combustion engines. When integrated downstream of exhaust cooling and conditioning stages, WES systems can effectively capture soot aggregates, ash particles, and nucleation-mode aerosols that are difficult to control with conventional particulate filters, especially under transient engine operating conditions. The electrostatic enhancement allows high collection efficiencies to be achieved without the high backpressure penalties associated with dense filtration media, making WES attractive for heavy-duty engines and non-road mobile machinery. The adaptability of electric field strength and droplet charge density further enables optimization across a wide range of engine loads and exhaust compositions.

Overall, this contribution demonstrates the WES as a multipurpose particle control technology that bridges aerosol science and process engineering. By presenting applications across multiple sectors, the work highlights the versatility of WES and its potential role as an enabling technology for advanced particulate mitigation strategies targeting fine and ultrafine aerosols under current and future emission standards (Seinfeld & Pandis, 2016).

Hinds, W. C. (1999). *Aerosol technology: Properties, behavior, and measurement of airborne* particles (2nd ed.), Wiley.

Parisi, A., Di Bonito, L. P., Carotenuto, C., & Di Natale, F. (2025) *Journal of Electrostatics*, 137, 104133.

Seinfeld, J. H., & Pandis, S. N. (2016). *Atmospheric chemistry and physics: From air pollution to climate change (3rd ed.)*, Wiley.

Numerical simulations of ns pulsed laser cavity-based aerosol gold nanoparticle size reduction and necking control via evaporation and sintering

J. Morán[1]

[1]Department of Mechanical Engineering, University of Ottawa, Ottawa, K1N 6N5, Canada
Keywords: Sintering, Gold nanoparticles, Self-diffusion, Necking, Agglomerate.

Presenting author email: jose.moran@uottawa.ca

Size and morphology control (essential for nanotechnology) of aerosol aggregates of nanoparticles notably metal or metal oxides is commonly achieved through monomer sintering in tube furnaces (Lähde *et al* (2014)). Even though this method is accurate, repetitive and simple, it is also energy intensive/inefficient and does not allow precise control of nanoparticle size and partial necking or overlapping particularly for intermediate primary particle diameters (5-60 nm). Alternatively, lasers can be used to efficiently deliver energy at individual aerosol particles with resolution down to µm and ns (space and time).

A numerical code was developed to simulate gold aerosol nanoparticle dimmers moving through a custom-design cavity (48 cm length; 6 mm ID; 1 L/min N_2 aerosol flow; ambient temperature and pressure) in which nanoparticles (Au dimmers; monomer diameter from 5 to 60 nm; 10^{13} m^{-3} uniform number concentration) are exposed to multiple ns laser pulses (Gaussian temporal profile; 7 ns FWHM; 10 Hz; 532 and 1064 nm wavelength) like those commonly used in light-induced incandescence (LII) measurements. The design (Fig. 1a) is similar to the experimental implementation from De Iuliis *et al* (2011) to study soot LII signal under multiple laser pulses. However, no numerical simulations exist for such system. Here, an energy balance equation is solved to account for the particle light absorption, cooling via evaporation, and via conduction with the surrounding gas (Sipkens *et al* (2022)). Light-absorption is determined considering the particle mass-equivalent diameter and laser wavelength based on the Mie theory. The model also considers a Beer-Lambert correction of the laser fluence reduction due to light-extinction across the cavity. This heat transfer model is coupled with a mass balance equation considering nanoparticle evaporation. Finally, another two equations are solved to determine the neck radius and shrinkage between the two monomers and their overlapping level considering grain boundary diffusion as the dominant sintering mechanism. We have proposed a new self-diffusion coefficient model for gold atoms valid for all temperatures below and above the melting point. This model was calibrated based on all-atoms molecular dynamics simulations. Unlike other methods from the literature, this approach allows the prediction of partial necking found at temperatures below the melting point and continuous transition from solid, liquid-like to liquid-phase.

Figure 1(b-c) show the time evolving mass-equivalent diameter and overlapping coefficient of monodisperse dimmers (30 nm primary particle diameter) at different laser fluences through the cavity where a new laser pulse arrives every 100 ms. Laser wavelength is 532 nm near the plasmonic resonance peak. This evidence clear combinations of laser fluence and residence times for particles in the cavity leading to different particle size and sintering-induced monomer overlapping. Single pulses can lead to partial sintering. This new nanoparticle post-processing system may be potentially combined with different nanoparticle synthesis methods such as flames or spark-ablation to produce precisely controlled nanoparticles in terms of both size and necking/overlapping in gas-phase.

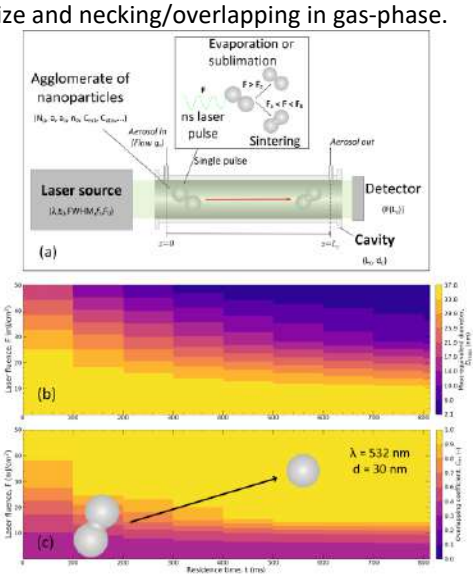

Figure 1. Model of the nanoparticle processing laser-cavity. Mass and monomer overlapping time evolution.

This work was supported by NSERC Canada, under grant RGPIN-2025-04803.

De Iuliis, S., Cignoli, F., Maffi, S. and Zizak, G., (2011) *Applied Physics B*, 104(2), 321-330.

Lähde, A., Koshevoy, I., Karhunen, T., et al. (2014) *Journal of Nanoparticle Research*, 16(11), 2716.

Sipkens, T.A., Menser, J., Dreier, T., et al. (2022) *Applied Physics B*, 128(4), 72.

Single-Droplet Techniques for Analysis of Evaporation Kinetics and Particle Morphology in Spray Dryers

B. E. A. Miles[1], L. Mahato[1], R. E. H. Miles[1], E. Costard[2], J. Schröder[2], A. Dubbelboer[2] and J. P. Reid[1]
[1]School of Chemistry, University of Bristol, Bristol, BS8 1TS
[2]Danone Research & Innovation, Uppsalalaan 12, 3584 CT Utrecht, the Netherlands
Keywords: drying kinetics, spray drying, morphology, formulation

Presenting author email: J.P.Reid@bristol.ac.uk

Investigation into the impact of droplet drying kinetics on the morphology of the resultant dried particle is crucial for understanding the spray drying process. Spray dried food powders require a flowability sufficient for the needs of both industry and consumers. Spherical particles with minimal surface irregularities are generally preferred (Eijkelboom et al. 2023), as particles with irregular shapes have a detrimental effect on the powder flow properties, affecting the dosing, mixing, and coating of the product (M. Capece et al. 2015). Understanding the impact of the drying conditions on the resultant powder properties can help increase the spray dryer efficiency and product quality (Eijkelboom et al. 2024).

Experiments in spray dryers have struggled to monitor the drying of the individual droplets directly, whereas single droplet drying (SDD) experiments have been shown to be successful in relating the drying behaviour of single droplets to the resultant particle morphology (Miles et al. 2024). However, SDD techniques struggle to represent the droplet size and temperature profile differences seen in spray dryers (Eijkelboom et al. 2023), so more work is needed to demonstrate if they are relevant for helping increase our understanding of the drying process in spray dryers.

Here, we present novel investigations into the drying kinetics of a aqueous solution droplets of a range of fat free, dairy-based powders, the impact of their drying behaviour on the final particle morphology and comparative generation of particles in an SDD technique against a small-scale Büchi B290 spray dryer.

An electrodynamic balance (EDB) was used to characterise the evaporation behaviour of the skimmed milk powders which, coupled with the SADKAT model (Robinson and Hardy (2022)) and the diffusion model reported by Siemons et al. 2019, allowed us to predict the SDD conditions that would reproduce the drying conditions experienced by droplets in a Büchi spray dryer. Using a falling droplet column (FDC) we then collected samples of particles that had been generated under equivalent drying conditions to those in a Büchi spray dryer (Miles et al. 2025). Scanning Electron Microscopy analysis of the particles showed we had successfully generated comparable morphologies in the SDD and spray dryer samples (Figure 1).

We also show the effect of the casein to whey ratio, total protein content and carbohydrate content on the drying behaviour and final particle morphology of model system droplets.

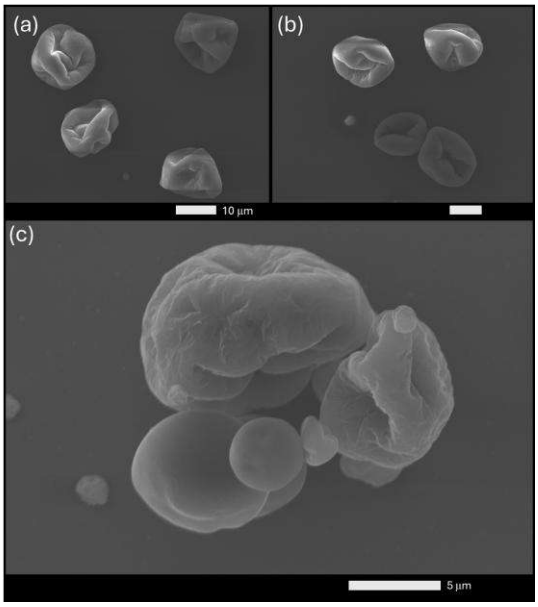

Figure 1. SEM images of fat free, dairy-based model system particles generated under different environmental conditions to obtain similar morphologies. (a) 0.05 MFS solution at 5% RH, 293 K in an FDC. (b) 0.05 MFS solution at 45% RH, 293 K in an FDC, (C) 0.25 MFS solution at 0% RH, 371 – 453 K in a Büchi B290 spray dryer.

N. M. Eijkelboom, A. P. van Boven, I. Siemons, P. F. C. Wilms, R. M. Boom, R. Kohlus and M. A. I. Schutyser, *J. Food Eng.*, (2023), **337**, No. 111222.
M. Capece, R. Ho, J. Strong and P. Gao, *Powder Technol.*, (2015), **286**, 561-571.
N. M. Eijkelboom, E. Hooiveld, J. Kingma, R. M. Boom, P. F. C. Wilms and M. A. I. Schutyser, *I. J. Dairy Tech.*, (2024), **77**, 1003-1016.
B. E. A. Miles, D. H. H. Chan, S. Varlas, L. K. Mahato, J. Archer, R. E. H. Miles, S. P. Armes and J. P. Reid, *Langmuir*, (2024), **40**, 734-743
Robinson, J. & Hardy, D. SADKAT: First stable release. Preprint at https://doi.org/10.5281/ZENODO.7174555 (2022)
I. Siemons, R. M. Boom, R. G. M. van der Sman and M. A. I. Schutyser, *Food Hydrocolloids*, (2019), **97**, 105219.
B. E. A. Miles, E. Winter, S. Mirembe, D. Hardy, L. K. Mahato, R. E. H. Miles and J. P. Reid, *JPCA*, (2025), **129**, 762-773

Thermally stable and spherical silver particles as a calibration transfer standard for nanoparticle measurement technologies

P.S. Bauer[1], A. Nowak[2], M. Dollner[1], V. Berger[1], A. Makelko[2], J. Roshal[2], H.J. Schulz[1], J. Swanson[1,3], A. Boies[1,4]

[1]Catalytic Instruments GmbH & Co.KG, 83026 Rosenheim, Germany
[2]Physikalisch-Technische Bundesanstalt (PTB), Braunschweig, 38116, Germany
[3]Minnesota State University, Mankato, MN 56001, United States
[4]Stanford University, Department of Engineering, Stanford, CA 94305, United States
Keywords: calibration, spherical particles, silver aerosol, PNC, CPC.

Presenting author email: paulus.bauer@catalytic-instruments.com

Many nanoparticle measurement technologies, such as Particle Number Counters (PNCs) or Volatile Particle Removers (VPRs), require a stable and well-characterized aerosol source for calibration. Several regulations (e.g., UN Regulation No. 168, Euro 7) and ambient air quality guidelines (e.g., EU Directive 2024/2881, EN 16976:2024) exist; however, different calibration aerosols, such as solid soot, emery oil, and silver particles, are currently used. This diversity leads to a lack of comparability among measurement results. Consequently, there is a need for an aerosol source capable of generating solid, inert, insoluble, and thermally stable spherical particles.

Silver particles generally satisfy all of these requirements. PTB and Catalytic Instruments are working closely together to optimize the Silver Particle Generator (SPG) (Hammer *et al*, 2022) to fulfil a broad spectrum of calibration protocols, e.g., for ambient and automotive specifications. The goal is to establish a calibration aerosol that could serve as transfer standard across different communities and various nanoparticle measurement technologies.

Since October 2025, several tests have been performed at PTB to investigate the long-term stability and day-to-day variability of the SPG. One important operating point is a particle size distribution with a Geometric Mean Diameter (GMD) at 6 nm which is used in several counting-efficiency calibration procedures. This GMD exhibits an apparent long-term stability of approximately 0.5 nm over two months. During this time, fluctuations in particle size were observed to correlate with variations in ambient pressure.

In addition, the SPG settings will be optimized to fulfil the CEN-CPC (PNC) calibration protocol (EN 16976:2024) for linearity and counting efficiency testing. We would like to pursue various strategies to calibrate PNCs, including shifting the size distribution by altering the temperature settings of the SPG or using a newly developed dilution method. An initial CPC calibration test was performed by varying the SPG temperature, demonstrating good stability, a straightforward setup, and minimal time effort. The smooth operation of the SPG is the ability for controlling the heater temperature in precise 1°C steps that allows a stable production of narrow size distributions of spherical silver particles but also enables the ability to shift these distributions. The resulting silver particles cover diameters up to 100 nm at concentrations between 10^3 and 10^6 cm^{-3}.

Spherical silver particles are commonly created by sintering agglomerated silver particles (Karlsson *et al*, 2005; Ku and Maynard, 2006; Tuch et al, 2016). However, the biggest challenge is to make spherical particles in a high concentration range for all applications/calibration procedure without secondary coagulation after the sintering process, which would compromise the sphericity again. With this project we will demonstrate the feasibility of producing spherical silver particles beyond 100 nm in diameter. This provides the basis to establish a harmonized calibration standard across different communities. Next to the improvements of the SPG performance, a PTB-developed dilution unit and a coagulation chamber will be optimized to guarantee spherical silver particles at high concentrations even beyond 100 nm.

The project has received funding from PTB's TransMet (Transfer of Metrological Technology) programme, with the objective of fostering the research capabilities and competitive edge of small and medium-sized enterprises (SMEs) in Germany.

EN 16976 (2024)

Directive (EU) 2024/2881 of the European Parliament and of the Council of 23 October 2024

Hammer, T., Irwin, M., Swanson, J., Berger, V., Sonkamble, U., Boies, A., Schulz, H., and Vasilatou, K. (2022). *J. Aerosol Sci.* **163**:105978.

Karlsson, M.N.A., Deppert, K., Karlsson, L.S., Magnusson, M.H., Malm, J.-O., and Srinivasan, N.S. (2005). *J. Nanoparticle Res.* **7** (1):43.

Ku, B.K. and Maynard, A.D. (2006). *J. Aerosol Sci.* **37** (4):452

Tuch, T., Weinhold, K., Merkel, M., Nowak, A., Klein, T., Quincey, P., Stolzenburg, M., and Wiedensohler, A. (2016). *Aerosol Sci. Technol.* **50** (4):331.

UN Regulation No. 168 (2024)

Aerosol Metal-Organic Frameworks (MOFs) Synthesis

Igor Novosselov[1], Ji Feng[1] and Almond Lau[1]

[1]Mechanical Engineering Department, University of Washington, Seattle, WA98195, USA
Keywords: metal-organic frameworks (MOFs), nanoparticles, continuous-flow synthesis, scalable synthesis
Presenting author email: ivn@uw.edu

Metal-organic Frameworks (MOFs) are very promising materials for gas sensing, catalysis, energy storage, water purification and drug delivery due to their high porosity, tunable pore sizes, adequate chemical and thermal stability, and various structures and compositions. Downsizing MOFs to the nanoscale brings superior properties over their bulk analogs, such as high surface-to-volume ratio, rich exposed metals and ligands, short diffusion path for reactants, which all contribute to improved performances. While great efforts have been made to reduce the particle sizes by controlling the reaction kinetics or terminating the particle growth with additives, large-scale synthesis of MOF nanoparticles with simple methods remains a challenge. We report the supercritical CO_2 assisted continuous-flow synthesis of MOF nanoparticles. As shown in Figure 1, the reactor features an easily modifiable extension section that enables control of the reaction residence time.

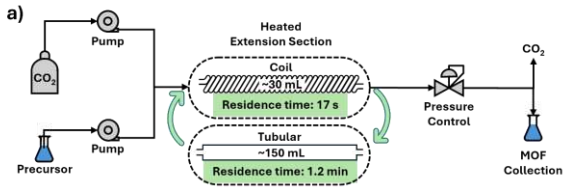

Figure 1. Simplified reactor schematic.

Synthesis of copper (Cu)-based MOFs

Operating in a single-phase ethanol-scCO_2 mixture, the method yields pure and thermal stable HKUST-1 nanoparticles with median sizes of 98-212 nm and BET surface area of 1613-1887 m^2/g in the residence time of just 3 seconds without any additives. A typical dry yield of 53.7 wt% is achieved with 0.1 M copper precursor at 75 °C and 13 MPa. Size analysis of the products obtained at different copper concentrations shows the influence of supersaturation and fluid phase behavior to the nanoparticle formation. Fractal dimension analysis indicates that the growth is caused by aggregation of primary nanocrystals, indicating a non-classical crystal growth mechanism.

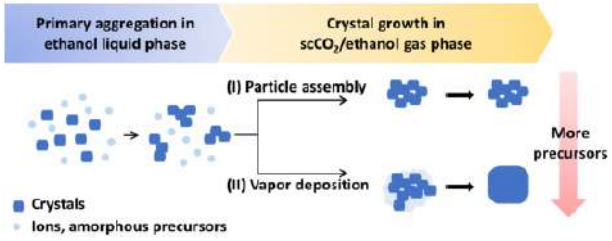

Figure 2. Schematic illustration of the non-classical particle growth.

Figure 2 shows two growth pathways: (1) particle-particle assembly, where particles aggregate forming "Tetris-like" compact structures; and (2) vapor deposition, where ions and amorphous oligomers self-assemble in the nascent aggregates, filling up the hollow structures in the aggregates.

Synthesis of zirconium (Zr)-based MOFs

Zr-MOFs are highly stable and structurally versatile porous structures with catalytic metal sites. Defective UiO-66 is well-studied for this application in chemical adsorption; however, the challenge remains in their large-scale production. In contrast to HKUST-1, which forms rapidly through direct coordination between metal ions and organic linkers, the formation of Zr-MOFs involves a more complex process with slower kinetics, beginning with the assembly of Zr_6 metal-oxo clusters that are subsequently coordinated with organic linkers. This slow reaction kinetic makes it difficult to obtain high-quality crystals under reduced residence times, as evidenced by decreasing residence time often leads to poor crystalline Zr-MOFs, resulting in reduced surface area and compromised performance in target applications.

We synthesized high-quality UiO-66, UiO-66-NH_2 and MOF-808 with ~1.2 min residence time. The role of scCO_2 is understood to promote the condensation of Zr-oxo clusters for fast nucleation, and the role of AA is to control the particle morphology from aggregates to single crystals (Figure 3).

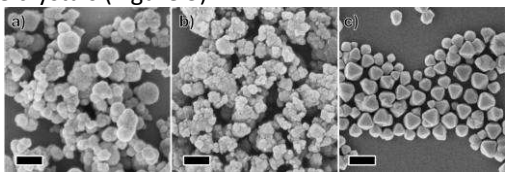

Figure 3. Morphology of Zr-MOF particles synthesized under different conditions. The AA/Zr^{4+} molar ratios are (a) 17.5, (b) 70, and (c) 105. The scale bars are 250 nm.

This work was supported by the US Defense Threat Reduction Agency under grant HDTRA12410010

J. Feng, A. Lau, I.V. Novosselov, HKUST-1 MOF nanoparticles: a non-classical crystallization route in supercritical CO_2, Nanoscale, 2024,16, 22142-22151.

A. Lau, J. Feng, V. Sushkevich, I.V. Novosselov, Supercritical CO_2-Assisted Rapid Crystallization of Zirconium-Based MOFs, in preparation.

A. Lau, J. Feng, C. Sorensen, I. V. Novosselov, Supercritical CO_2 Synthesized UiO-66-NH_2-Coated GO Composites - a Viable Photocatalyst, in preparation.

submission id: 20203492

Flame Spray Pyrolysis Engineering of Interfacial Quantum States in H_2-Photocatalytic Semiconductors: control of Photophysics via Precision Engineering

Yiannis Deligiannakis*, Loukas Belles

Department of Physics, University of Ioannina, 45110, Ioannina, Greece
Keywords: *Flame Spray Pyrolysis, Quantum Size, Photocatalysis, H_2, CO_2,*
email: **ideligia@uoi.gr**

Flame Spray Pyrolsyis (FSP) is established aerosol technology for scalable production of functional semiconductors. Targeting highly-efficient Green photocatalytic H_2 production form H_2O splitting, entails addressing several milestone challenges: among them the currently-viewed particle-lattice-structure does not suffice to describe/control all key-functional milestones. Interfacial Quantum States (IQS) i.e. interfacial configurations that determine the interface {periodic lattice} and {environment}, is an extension of our perception of the nanocrystal phase-space. Herein we have used FSP-technology to engineer IQS in two cases [i] Cu-subnanoclusters interfaced with periodic $NaTaO_3$ nano-lattice[1] [ii] in TiO_2(B)- subnanoclusters interfaced with TiO_2-Quantum dots[2].

The materials have been produced via a two-phase FSP-process where operating *in tandem* where an FSP-reaction chamber particle formation evolves in a Low-T-Compartment of controlled gas-environment. This Low-T-FSP configuration operates sequentially to a classical FSP-nozzle (High-T-FSP).

Cu-$NaTaO_3$: using HT-LT-FSP setup we have engineered Interfacial Quantum States (IQS) of Cu-subnanoclusters interfaced with $NaTaO_3$. $NaTaO_3$ is a perovskite-oxide that requires high-combustion enthalpy for its formation[3]. The process for $NaTaO_3$ formation nanoparticle formation (12nm) was achieved via optimisation of the process in the HT-FSP compartment. Then the so-formed $NaTaO_3$ NPs were decorated with subnanoclusters of Cu-atoms, sprayed under low-enthalpy conditions in the LT-FSP compartments. In this way a library of Cu:$NaTaO_3$ nanostructures were produced with Cu-loadings corresponding to either isolated Cu-atoms or Cu-subnanoclusters or CuO-particles[1].

Photocatalytic H_2-production from H_2O, shows that the optimal Cu:$NaTaO_3$ nanostructure was Cu-subnanoclusters:$NaTaO_3$, *rather that the -currently believed {Cu-single atoms-semiconductor}* configuration. A detailed XPS, Raman, DRS, EPR analysis[1] revealed that the configuration {Cu-subnanoclusters-on-semiconductor} provides the optimal Interfacial Quantum States of Cu that boost the transfer of the photoinduced -electron from $NaTaO_3$ to the H2-forming interface[1].

TiO_2(B/TiO_2(QD) : using our HT-LT-FSP setup we have engineered Interfacial Quantum States of TiO_2(B) nano islands interfaced with TiO_2-Quantum-Dots (3nm). TiO2(B) is a metastable TiO2-pahse preferable at low-T in the phase diagram[2]. The process for TiO_2(B) nano islands formation was achieved via optimisation of the process in the Low-T-FSP compartment.

Photocatalytic H_2-production from H_2O, shows that the optimal {TiO_2/TiO_2(B)} Quantum Dot Hybrids constitute the best -so far in literature- H2-phtocatlysts that achieves H_2 production of >150mmol H2/per gr/h.[2] A detailed XPS, Raman, DRS, EPR analysis[2] revealed that the configuration of {TiO_2/TiO_2(B)} Quantum Dot Hybrids provides the optimal Interfacial Quantum States of Cu that boost the transfer of the photoinduced -electron from TiO2(anatase) to TiO2(B) and to the H_2-forming interface[2].

These two examples demonstrate, for the first time, that semi amorphous-cocatalysts interfaced with crystalline -nanolattices are able to produce Interfacial Quantum States that -when optimised- allow unprecedented boost of photocatalytic H_2-production. Application of this now concept IQS via anchoring of semi amorphous co-factors to crystalline nanolattices can be achieved via FSP-technology, by taking advantage of control of the combustion-enthalpy profile. In a more general context, we discuss the use of hybrid HT/LT-FSP as an asset-technology applicable to many possible nano heterostructures where the interface of {non-periodic lattice}-{periodic lattice} is the generator of Interfacial Quantum States.

REFERENCES

[1] Spyrou A, Zindrou, Sidiropoulos. C., Deligiannaksi, Y *Atomic Cu2+ Clusters vs Single Cu2+ Atoms as Optimal Cocatalysts on NaTaO3 for Enhanced Noble-Metal-Free H2O/H2 Photocatalysis* **ACS Catalysis,** 15, 13595, 2025

[2] Dimitriou, C., Belles, L, Boukos, N. Deligiannakis, y *2/TiO2(B)} Quantum Dot Hybrids: A Comprehensible Route toward High-Performance [>0.1 mol gr-1 h-1] Photocatalytic H2 Production from H2O* **ACS Catalysis,** 14, pp. 17919, 2024

[3] Psathas, P. Moularas, C, Smylakys, S, Deligiannaksi, Y. Highly Crystalline Nanosized NaTaO3/NiO Heterojunctions Engineered by Double-Nozzle Flame Spray Pyrolysis for Solar-to-H2 Conversion: Toward Industrial-Scale Synthesis **ACS Appl Nanomaterials** 6, 2658, 2023.

Acknowledgment

The research work was supported by the Hellenic Foundation for Research and Innovation (HFRI) under the 5th Call for HFRI PhD Fellowships (Fellowship Number: **19136**).

Aerosol synthesis of carbon nano onions and its role as sensing layer in In_2O_3/CNOs composite for sensitive H_2S detection at room temperature

J. Shettar[1], M. Tanveer[2], A. Lähde [2], R. Ghosh[1]
[1]Department of Electrical, Electronics and Communication Engineering, Indian Institute of Technology, Dharwad – 580011, Karnataka, India
[2]Department of Environmental and Biological Sciences, University of Eastern Finland, P.O. Box 1627, 70211 Kuopio, Finland
Keywords: Flame spray pyrolysis, Carbon nano onions, core to shell morphology, H_2S sensing, Resistive sensor.
Presenting author email: muhammad.tanveer@uef.fi

Sensing layer plays an important role in resistive sensors as it directly affects sensitivity, selectivity, speed, and energy efficiency of the sensors. Carbon nano onions (CNOs) are an emerging class of carbon nanostructures and attract attention of researchers owing to their unique morphologies and structural features. CNOs offer high surface to volume ratio, thereby maximizing the available sites for the gas adsorption. Also, porous structure of CNOs improves the diffusion and transport of gas analytes to the active sites and thereby enhances the response times (S.D Lawaniya, et al. 2024). This study deals with synthesis of CNOs via flame spray pyrolysis (FSP) and its deployment as In_2O_3/CNOs composite for sensitive H_2S detection at room temperature.

Carbon nano-onions were produced using xylene in a closed FSP system under controlled and oxygen deficient environment. The changes involved in different synthesis stages resulted in core to as shell morphology of CNOs, contributing to variation of particle size. The growth process was controlled by the temperature gradient and residence time in the flame. As produced CNOs were composed of organic carbon (OC) and their prolonged exposure to high temperature conditions in closed FSP resulted in gradual reorganization and evolution of core to shell morphology. As obtained CNOs contained organic carbon and unburned residues, which were removed with Soxhlet extraction method. Following this, as obtained black CNOs were pyrolyzed in tube furnace at 500 °C for 3 h under nitrogen environment to further improve the conversion to elemental carbon and thereby its graphitic nature. (M. Tanveer et al. 2025). As produced CNOs were mixed at different ratios with In_2O_3 that was synthesized through hydrothermal treatment to obtain the optimum composition of In_2O_3/CNOs composite.

The morphology and structural features of the as produced In_2O_3/CNOs composite material was analyzed employing TEM analysis. Figure 1a shows that as obtained composite particles were in nanoscale which is essential for achieving a high surface-to-volume ratio and in turn, improved sensing performance. Figure 1 (c) presents the XRD pattern of the In_2O_3 /CNO (2:1) composite, clearly showing diffraction features corresponding to both In_2O_3 and CNO. The sharp peaks are attributed to crystalline In_2O_3, while the broad humps arise from the graphitic, amorphous carbon structure of the CNOs.

Figure 2 presents the gas sensing response of the composite under different ratios at room temperature. Figure 2 (a) shows response for ratio 1:1 (In_2O_3 /CNO) which exhibits weak response and poor recovery

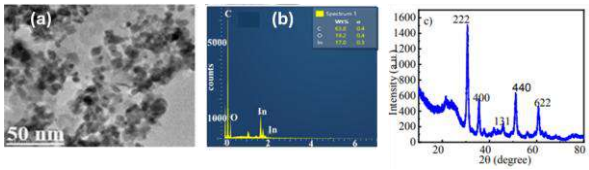

Figure 1. (a, b) TEM image and EDS spectrum of composite (c) XRD spectrum of the composite.

indicating limited interaction between the gas molecules and the sensing surface Figure 2(b) shows higher proportion of CNO with ratio 1:2 and it presents a low and sluggish response with incomplete recovery. Finally, figure 2(c) exhibits response for ratio 2:1, indicating high and reversible response with complete recovery across all tested concentrations.

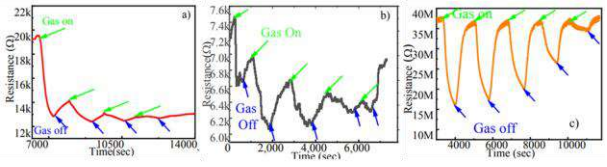

Figure 2. The resistance transients of (a) In_2O_3/CNOs (1:1) (b) In_2O_3/CNOs (1:2) (c) In_2O_3/CNOs (2:1).

Response time, recovery times and selectivity of the sensor against different gases were also analyzed. Moreover, the mechanism involved in gas sensing is also explored in this study. Keeping in view the results it is believed that this research can lead to the development of highly efficient, low power consuming, and portable sensors for H_2S.

This work was supported by Board of Research in Nuclear Sciences with grant ID 59/14/08/2024-BRNS/726 and Jane ja Aatos Erkon Säätiö (Versa-MOF 6833-57e45).

S.D Lawaniya, et al. (2024), *Sci Rep. 14, 7904*
M. Tanveer, et al. (2025) *Nanotechnology 36, 445603.*

A novel on-line single aerosol-particle laser mass spectrometer for simultaneous inorganic and molecular organic chemical aerosol characterization: Technology and application

J. Passig[1], E. Rosewig[1], H. Hakim[1], M. Ihalainen[2], O. Sippula[2], A. Virtanen[2], R Irsig[3], A.Walte[3], R. Zimmermann[1,2]*

[1] Chair of Analytical Chemistry, University of Rostock, Rostock, Germany
[2] Departments of Chemistry and Sustainable Technology & Environmental and Biological Sciences, University of Eastern Finland, Joensuu & Kuopio, Finland
[3] Photonion GmbH, Schwerin, Germany

Keywords: Aerosol Single Particle Mass Spectrometer, New Laser Ionization Approach, Wildfire and marine aerosols, Polycyclic Aromatic Hydrocarbons

* Presenting author email: ralf.zimmermann@uni-rostock.de

By emitting large amounts of CO2, reactive trace gases and particulate matter (aerosols), wild fires and anthropogenic combustion emissions strongly affect air quality, human health and climate. Atmospheric aging and particle-gas phase distribution of these emissions are extremely complex and variable. Moreover, the photochemical changes are highly relevant to climate and health by determining the particle's optical- and radiative-effects, cloud condensation-activity and biological/toxic effects. To better understand the impact of wildfire emissions (and of other pollution-sources like ship emissions) it's very important to analyse the internal and external mixing-state of relevant components in the aerosol particle distribution (1).

The new technology of field-deployable resonance-enhanced single particle mass spectrometry (2,3,4) is giving unsurpassed access to single particle chemical distribution-information, has been applied e.g., to wildfire emissions, generating intriguing results. In classical on-line single particle mass spectrometry (SPMS), aerosol particles from ambient air are introduced directly by an aerodynamic-lens into the SPMS analyser. Individual particle sizes and their ion source-arrival times are determined by laser-velocimetry and intense UV-laser pulses are triggered to hit selected individual particles for laser desorption/ionization (LDI). Formed anions and cations from individual aerosol particles are detected in a bipolar time-of-flight MS setup. Beyond this, we recently introduced a multi-step laser ionization scheme in SPMS, exploiting on-the-fly IR-laser desorption and resonance ionization of transition metals (using 248 nm atomic iron transition) as well as of the toxic Polycyclic Aromatic Hydrocarbons (PAH, using Resonance Enhanced Multiphoton Ionization). This allows to detect efficiently the most important air trace-toxicants (PAH, transition metals) together with more abundant species (soot, minerals, ammonium sulphate etc.) on single particle-basis. Using this new resonant-ionization SPMS-method, metals and PAHs can be detected in real-time (2,4) at much lower quantities and less dependent from the matrix (e.g., sea salt, organics etc.) on particles, opening the avenue to detect the carcinogenic PAHs on single-particle basis. We investigated ambient air (Baltic Sea), revealing sources and carriers of PAHs. The results suggest PAHs as molecular markers to retrieve pollution sources and aerosol transformation-processes in complex environments. Indeed, we observed aerosol aging-processes via PAH-signatures. In addition to local ship emissions also biomass burning particles were observed. In another study, particles from smoke from wildfire simulation burns were investigated. Typical vegetation from e.g., the boreal forest and African savannah was used as model fuel. Fresh and photochemically aged wildfire emissions were investigated. For climate- and health-relevant PAH we found high concentrations of the softwood combustion-marker retene in boreal forest burnings as well as its rapid degradation during aging. The toxic, larger unsubstituted PAHs show higher stability against photooxidation. Particles with the highest PAH-loads are observed in the long-range transported size mode even after prolonged aging, in accordance with the ambient air study (3). For the water-soluble components, we could show the time-resolved glyoxal/methylglyoxal-formation during photochemical chamber-aging. Interestingly, a non-uniform mixing of water-soluble glyoxal/methylglyoxal and non-polar PAH was observed (i.e., 2 particle-classes with different chemical composition). Counterintuitively, atmospheric aging reduces cloud condensation nucleation-activity (CCN) of wildfire aerosol-particles, are explainable by the observed sulphatisation of potassium-chloride to the less hygroscopic potassium-sulphate during aging. The CCN-activity of the aerosols, however, has a large impact on the climate impact of wildfire emissions. A further application focuses on the particle emission from large ship diesel engines. Ship emissions are highly relevant for climate (i.e., light absorbing and cloud formation activity) health as well. The impact of fuels and abatement technology is discussed. Finally, also security relevant aerosols, such as aerosolized particles from drugs of abuse (e.g. cocaine of fentanyl) or explosives (e.g. TNT) are addressed by SPMS.

(1) N. Riemer et al. (2019) Rev. Geophys. 57, 187ff.
(2) J. Passig et al. (2020) Atmos. Chem. Phys. 20, 7139ff.
(3) J. Passig et al. (2022) Atmos. Chem. Phys., 22,1495ff.
(4) J. Schade et al. (2019) Anal. Chem. 91,10282ff.

A Real-World Benchmarking Method for Intercomparing Airflow Cytometer Coarse Particle Concentration Measurements

E. Graf[1], R. Abt[1], A. Schwendimann[1], E. Niederberger[1]

[1]Swisens AG, Emmen, 6032, Switzerland
Keywords: Standardization, Bioaerosol Monitoring, SwisensPoleno
Presenting author email: erny.niederberger@swisens.ch

Automatic bioaerosol measurement instruments are increasingly used for operational monitoring and research applications, creating a need for standardized performance evaluation and intercomparison under real-world conditions. While laboratory studies have shown good reproducibility between identical instruments (Vasilatou et al., 2025), fewer studies have examined whether this agreement persists in complex ambient environments. In this study, four SwisensPoleno Jupiter instruments were co-located for several consecutive days at an outdoor site in Emmen, central Switzerland for comparison. The instruments operated continuously and independently during a November campaign that targeted ambient aerosols in general, not only bioaerosols. For the intercomparison, a subset of coarse mode particles with equivalent area diameter ≥ 16 µm and solidity ≥ 0.9 was selected using holographic imaging. This pre-filtering, typically applied for pollen classification defines "pollen candidates" but includes all sorts of other coarse aerosol particles.

Absolute "pollen candidates" concentrations showed very close agreement across all instruments throughout the campaign (Figure 1). Temporal variability, including rapid concentration changes and peak events, was consistently captured by all instruments with only small absolute deviations. Inter-instrument correlation analysis revealed very strong agreement, with Kendall's τ correlation coefficients exceeding 0.91 for all instrument pairs (Figure 2).

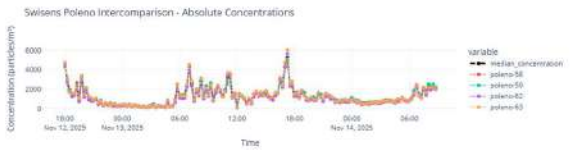

Figure 1. Concentrations measurements (particles / m3) of four SwisensPoleno Jupiter show relatively small absolute errors and high correlation of "pollen candidate" coarse particles.

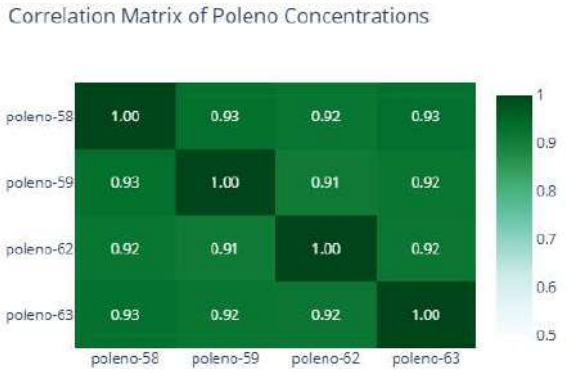

Figure 2. The four SwisensPoleno Jupiter instruments show very strong Kendall t correlation (> 0.91) for pollen candidates.

These results are consistent with laboratory calibration findings on counting efficiencies reported by Vasilatou et al. (2025). Overall, the intercomparison demonstrates high agreement in both correlation and absolute concentrations, supporting the reliability of such instruments for monitoring networks and contributing to ongoing efforts toward standardized evaluation and harmonization of automatic bioaerosol measurement instruments.

This work was part of the SYLVA project (HE-CL6-GOV-IA-2022-101086109) and has received funding Innosuisse (Project Nr. 107.676 IP-ICT) and from the EU.

Vasilatou, K.; Giannakoudaki, C.; Abt, R.; Auderset, K.; Crouzy, B.; Erb, S.; Erdogdu, A. O.; Graf, E.; Iida, K.; Lieberherr, G.; Sakurai, H.; Schmale, J.; Wälchli, C.; Horender, S. Toward Accurate Real-Time Bioaerosol Monitoring in the Particle Size Range 1 µm–70 µm. ACS ES&T Air 2025, 2 (12), 2979–2990. https://doi.org/10.1021/acsestair.5c00282

Better Accuracy & Automation of the CERMS for Calibrating Black Carbon Mass Analysers

J.P.R. Symonds[1], R. Mehri[2], J.S. Olfert[3], G. Smallwood[2], B. Smith[2], C.D. Nickolaus[1], E. Goktepe[1], K.St.J. Reavell[1], M. Parker[4], M. Johnson[4]

[1]Cambustion, Cambridge, CB1 8DH, U.K.
[2]National Research Council Canada, Ottawa, K1A 0R6, Canada
[3]Department of Mechanical Engineering, University of Alberta, Edmonton, T6G 1H9, Canada
[4]Rolls-Royce PLC, Derby, DE24 8BJ, U.K.
Keywords: metrology, black carbon, mass, laser induced incandescence

Presenting author email: jps@cambustion.com

The CPMA Electrometer Reference Mass System (CERMS, Symonds *et al*., 2013) uses a Centrifugal Particle Mass Analyser (CPMA) in conjunction with a unipolar charger and an aerosol electrometer (AE) as a calibration standard for instruments which measure particle mass concentration. Particles from any source are charged and then classified by mass-to-charge ratio in the CPMA. Particles at the single charge mass setpoint will gain 1 elementary charge, particles at twice that mass will gain 2 elementary charges, and so on. In this way each quantum of mass can be thought of as being tagged with one charge. By measuring the charge concentration downstream of the CPMA with the AE and multiplying it by the mass setpoint, the mass concentration exiting the CPMA can be directly calculated. By splitting the flow exiting the CPMA into an Instrument Under Test (IUT) the CERMS can be used as a calibration source for the IUT of known mass concentration.

The CERMS is an appealing method as it depends only upon easily traceable physical properties of the CPMA and AE, namely the CPMA voltage, speed and classifier radii, the AE current and the flow through it. Mehri *et al.* (2025) showed that the least reproducible element is the CPMA mass (10% between 3 systems) and given the ease of delivering accurate speed and voltage, the root cause here is likely to be uncertainty in the classifier dimensions, where gap between two independent cylinders must be precisely controlled. The recent development of mass certified polystyrene latex spheres (PSL) by AIST in Japan has enabled an “end to end” calibration of the CPMA for the first time, without needing to convert sizing standards to mass using an assumed density.

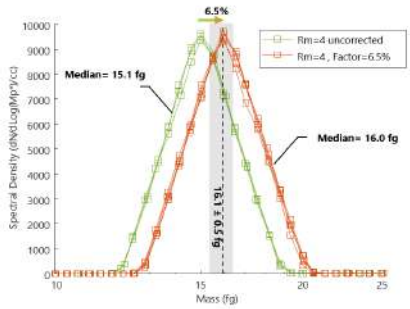

Figure 1. Calibration of a CPMA using mass PSL

The mass certified PSL (at 16.1 fg) is diluted, nebulised and dried and passed through a neutraliser and DMA to impart charge. The CPMA under calibration is scanned into a CPC. Data is fitted using a model of the transfer function of the CPMA. Figure 1 shows the result from one CPMA where a 6.5% deviation from the standard was observed. The CPMA is adjusted in software to change the assumed radii of the cylinders.

When calibrating a mass concentration instrument using the CERMS, it is usually required to deliver a range of mass concentrations to be able to fit a calibration function to the data. We show this is best achieved by firstly finding the peak mass concentration output of the CERMS by scanning the CPMA and then setting the CPMA to that particle mass value. Secondly a diluter is used after the particle source to progressively apply dilution to attenuate the mass concentration and therefore obtain a sweep to test the linearity of the IUT. The Cambustion AD60 is a continuously variable rotating disk diluter and this can be used under closed-loop control based on the CPMA-AE mass output to give a dynamic range of around two orders of magnitude. Software has been written to automate this entire process, and Figure 2 shows an example of this being used to check the calibration of an Artium LII 300 Laser Induced Incandescence instrument in under 10 minutes.

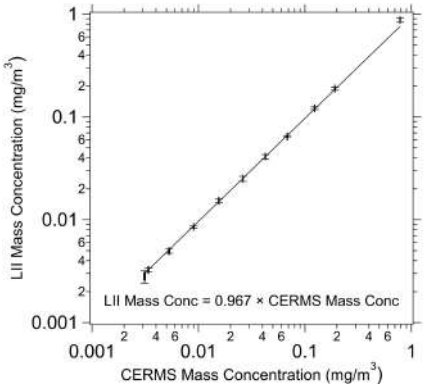

Figure 2. LII calibration using nebulised CB

Mehri R., Nishida R.T., Sipkens T.A. *et al*. (2025) *Aerosol Science and Technology*.
Symonds, J.P.R., Reavell, K.StJ., Olfert, J.S. (2013) *Aerosol Science and Technology.* **47**, i–iv.

Comparison of ELPI+ with SMPS and APS on various laboratory generated aerosols

A. Arffman[1], P. Juuti[1], J. Haapanen[1], P. Roztočil[2], M. Nikka[1], O. Vainio[1], P. Otáhal[3], E. Fialová[3,4], L. Balco[5], and J. Ondráček[2]

[1]Dekati Ltd., Kangasala, FI-36240, Finland
[2]Research Group of Aerosol Chemistry and Physics, ICPF CAS, Prague, 165 00, Czech Republic
[3]National Institute for NBC Protection, Milín, 262 31, Czech Republic
[4]Department of Geological Sciences, Faculty of Science, Masaryk University, 60200 Brno, Czech Republic
[5]Biowell s.r.o., Bratislava, 851 01, Slovakia

Keywords: ELPI+, OFR, effective density, aerodynamic size, SMPS.

Presenting author email: anssi.arffman@dekati.fi

Particle size distribution (PSD) measurement instruments can rely on different physical phenomena for detection and size classification of aerosol particles. Inherently, this leads to slightly different results even when instruments are measuring hypothetically ideal aerosol samples. This is why the relation between the different instruments is important to address and compare. In this study we intercompare three of the widely known instruments: Electrical Low Pressure Impactor [1] (ELPI+), Scanning Mobility Particle Sizer [3] (SMPS), and Aerodynamic Particle Sizer [4] (APS). Details of the instruments can be found from references or e.g. textbooks considering aerosol measurement, and only a very concise introduction is given here.

The ELPI+ measures aerosol aerodynamic PSD in real-time by inertially size classifying particles into aerodynamic size bins and uses electrical detection of particle concentrations. In this study, the ELPI+ ([2], Dekati Ltd.) was used with HR-ELPI+ data inversion. The SMPS instrument size classifies particles according to their electrical mobility and then detects particle concentrations of different size particles with a condensation particle counter (CPC). The SMPS instrument used in this study was EC 3082 with DMAs 3080 and 3081A (all TSI Inc.). The APS instrument (3321, TSI Inc.) measures the particle's time-of-flight through an accelerating nozzle. This way it provides an aerodynamic size spectrum, but in general, it measures only particle sizes larger than appr. 0.5 µm and the concentration range is lower compared to the ELPI+ or SMPS.

Studied particle materials were monodisperse PSL spheres, ammonium sulphate (AS), diethylhexylsebacate (DEHS), dry soot, soot with secondary organic condensates (SOA), sodium chloride (NaCl), and silver (Ag). PSL, AS, NaCl particles were generated by dispersing/dissolving materials into proper solvents and nebulized and dried. Soot particles were generated with the miniature inverted soot generator (MISG, Argonaut Scientific). After the generation, the soot aerosol was diluted with an eDiluter Pro (Dekati Ltd.) and then conducted to an oxidation flow reactor (DOFR, Dekati Ltd.) to oxidize precursor vapors that then can condense inside the OFR onto the soot particles or alternatively were measured without the OFR processing. Ag and DEHS particles were generated with an evaporation-condensation process, and the effective density of particles was investigated by combining the ELPI and the SMPS results.

Figure 1 shows example of results for the dry soot and OFR aged soot + a-pinene. The deviation between the HR-ELPI+ and SMPS is large for dry soot particles as the effective density is well below unit density. In the case of the OFR aged soot + a-pinene, low vapor pressure organic vapors formed in the OFR condense onto soot particles and the particle mass and aerodynamic size increases shown by the HR-ELPI+ whereas the mobility size is rather inert for the condensates as shown by the SMPS.

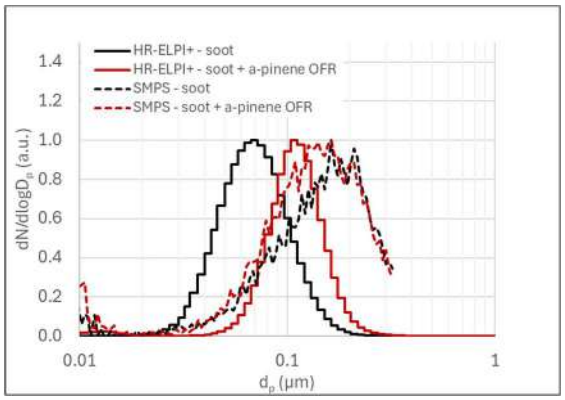

Figure 1. The dry soot and OFR aged soot with a-pinene precursor measured with the HR-ELPI+ and the SMPS.

[1] Keskinen, J., Pietarinen, K., & Lehtimäki, M. (1992). *Journal of Aerosol Science, 23*, 353-360.
[2] Järvinen, A., Aitomaa, M., Rostedt, A., Keskinen, J., & Yli-Ojanperä, J. (2014). *Journal of Aerosol Science, 69*, 150-159.
[3] Wang, S.C., & Flagan, R.C. (1989). *Aerosol Science and Technology, 13*, 230-240.
[4] Agarwal, J. K. (1981). *The Inhalation, Toxicology and Technology Symposium*, B. K. J. Leong, ed., Ann Arbor Science Publishers, Ann Arbor, MI, 207–231

Experimental Validation of High-Efficiency Stairmand and Swift Cyclones Using Optical Particle Spectrometry

R. Durand, F. Ghione Roasio, R. Guido, E. Norata, S. Zago and P. Tronville

Department of Energy, Politecnico di Torino, Turin, 10129, Italy
Keywords: cyclone separator, Stairmand, Swift, fractional efficiency, optical particle spectrometer.

Presenting author email: paolo.tronville@polito.it

Several industrial applications employ high-efficiency cyclone designs (e.g., Stairmand and Swift). These inertial separators are commonly designed using semi-empirical models for removal efficiency. However, open validation datasets — especially for Swift-type cyclones — remain scarce.

We manufactured two small-scale reverse-flow cyclones (Stairmand-HE, D=38 mm; Swift-HE, D=40 mm) by selective laser sintering and tested them in a dedicated aerosol rig. HEPA-filtered air was mixed with a synthetic DEHS aerosol generated by a Laskin nozzle. Upstream and downstream size distributions were measured sequentially with two optical particle spectrometers (TSI OPS 3330 and TSI LAS 3340A). We used a correlation-ratio test to correct for system asymmetry/line losses. We converted optical diameters to equivalent aerodynamic diameters in accordance with ISO Technical Specification 19713-1.

Fractional efficiency curves shifted to smaller diameters as the flow rate treated by the cyclones increased. Using LAS 3340A data, the estimated cut size d_{50} decreased from ~2.20 µm at 3 $m^3\ h^{-1}$ to ~0.67 µm (Stairmand) and ~0.56 µm (Swift) at 10 $m^3\ h^{-1}$. At the design flow rate (8 $m^3\ h^{-1}$), Swift-HE outperformed Stairmand-HE in the 0.7–1.6 µm range (η = 66% vs 54% at 0.7–1.0 µm; η = 87% vs 74% at 1.0–1.3 µm). Pressure drop increased approximately quadratically with flow (0.22–2.75 kPa across the tested range), with Swift-HE showing consistently higher Δp.

Table 1. Summary of measured cut size and pressure drop (LAS 3340A).

Q ($m^3\ h^{-1}$)	d_{50} (µm) Stairmand / Swift	Δp (kPa) Stairmand / Swift
3	2.20 / 2.19	0.22 / 0.25
6	1.16 / 0.95	0.87 / 0.99
8	0.79 / 0.72	1.55 / 1.83
10	0.67 / 0.56	2.35 / 2.75

Comparison with the widely used Iozia–Leith semi-empirical model reproduced the overall trend in removal efficiency with flow rate. It matched Stairmand-HE reasonably well at moderate flows, but systematically underpredicted Swift-HE performance as flow increased. For particles larger than ~3 µm, interpretation requires care, as deposition in tubing/adapters reduces upstream concentration, underscoring the need for correlation-ratio correction and uncertainty analysis.

These measurements provide a modern benchmark dataset for validating cyclone efficiency correlations and CFD simulations for standard high-efficiency geometries, as well as for quantifying the impact of additive manufacturing tolerances on performance.

Figure 1. Cyclones produced by additive manufacturing (bottom) and test rig for measuring their performance.

This study was carried out within the MICS (Made in Italy–Circular and Sustainable) Extended Partnership and received funding fromNext-GenerationEU (Italian PNRR–M4C2, Invest1.3–D.D.1551.11-10-2022, PE00000004).

Erol, H.I. *et al* (2019) *Heat and Mass Transfer*. **55**, 2341–2354.

Hoffmann, A.C., Stein, L.E. (2010) *Gas Cyclones and Swirl Tubes - Principles, Design and Operation*, Springer.

Iozia, D.L., Leith, D. (1989) *Aerosol Science and Technology*. **10**, 491–500.

Iozia, D.L., Leith, D. (1990) *Aerosol Science and Technology*. **12**, 598–606.

Leith, D., Mehta, D. (1973) *Atmospheric Environment*. **7**, 527–549.

Ramachandran G. *et al* (1991) *Aerosol Science and Technology*. **15**, 135–148.

Mass, Size and Density Fingerprints of Engineered Particles

J.P.R. Symonds[1,2], F. Friebel[2], J. Wieder[2] and K.St.J. Reavell[1,2]

[1]Cambustion Limited, Cambridge, CB1 8DH, U.K.
[2]femtoG A.G., 8057 Zürich, Switzerland
Keywords: engineered nanoparticles, mass, size, density, instrumentation, titania

Presenting author email: jps@cambustion.com

The application of online analysis techniques rooted in aerosol science to the study of engineered particles is of increasing interest. Provided particles can be suspended in the aerosol phase, the use of one or more classifiers such as the Differential Mobility Analyser (DMA), Aerodynamic Aerosol Classifier (AAC) and Centrifugal Particle Mass Analyser (CPMA) to gain insight into size, mass, density and structure is established. However, classifiers which rely on the particles being charged such as the DMA and CPMA (but notably not the AAC) are limited in size range due to the need to charge the particles and correct for multiple charging artefacts, a process which depends upon particle morphology.

The Mass and Mobility Aerosol Spectrometer (M^2AS, Walker & Reavell 2020, Figure 1) circumvents this issue by measuring the actual charge state of particles during a CPMA scan and using that information to perform the charge correction. The mean charge is determined using the ratio of measurements from aerosol electrometry and a particle counter. A unipolar charger is used to ensure that the charge distribution is narrow (and hence the mean charge can be assumed to be representative), and to extend the range of the CPMA to several microns. To fully correct the mass scan for the transfer function of the CPMA, information on mobility size is required. Rather than running a lengthy separate scan, a new instrument called the Mobility Separator-Electrometer (MSE, Hassim *et al.* 2025) is used which determines the mobility simultaneously during the CPMA scan. It divides the incoming aerosol into two flows which are split according to electrical mobility between two electrometers which are kept in balance. The sum of the currents from both electrometers is used for the charge correction. The M^2AS gives mass spectral density, size spectral density & density.

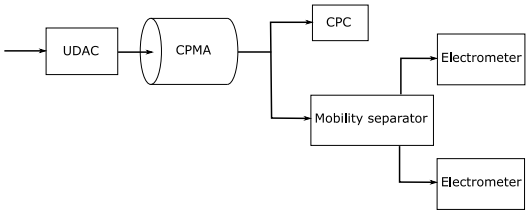

Figure 1. Mass and Mobility Aerosol Spectrometer

Recently the M^2AS has been applied to the analysis of engineered particles by femtoG AG. In a system known as the PowMaster, prior to analysis the particles are suspended in water and deagglomerated using ultrasound. The suspension is then diluted and the isolated particles extracted via spray-dispersion.

There are many engineered materials that consist of more than one material and have a complex structure. One example is titanium dioxide based white pigments. Those particles typically exhibit a core-shell structure where the TiO_2 particles are encapsulated by a layer of dense and/or porous silica. This surface-treatment reduces their photocatalytic activity, improves their dispersibility and results in a whiter paint.

For the material's performance, it is crucial that enough shell material is deposited onto the core particle and stays attached. We applied mechanical stress (similar to levels imparted in processing) by using progressive ultrasound. PowMaster analysis shows increasing shearing off of the shell material (Figure 2).

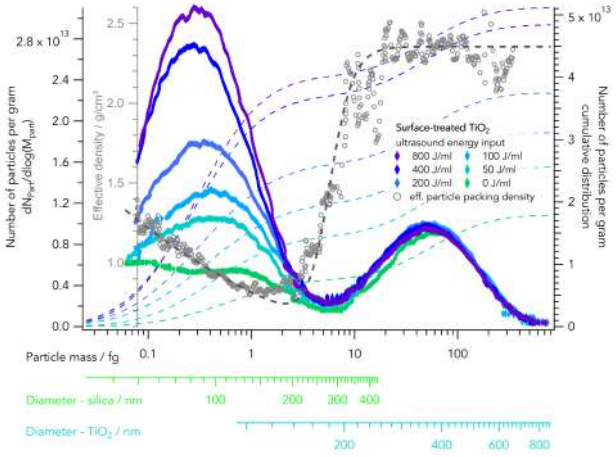

Figure 2. Mass spectral density of surface treated TiO_2 with increasing ultrasonic energy showing delamination

This compromises the material's function, costs more (as more coating is required) and raises questions regarding nanomaterial safety regulation as the delaminated particles are generally < 100 nm. Furthermore, this effect cannot be detected with established sizing methods (e.g. laser diffraction, sedimentation analysis) as the sheared- off silica particles have a different structure, density and refractive index than the TiO_2-core particles.

Walker, D., Reavell, K.St.J. (2020) in *Cambridge Particle Meeting*

Hassim, J., Hochgreb, S., Reavell, K.St.J. (2025) *Aerosol Science and Technology.* **59**, 267–291

SEMS Transfer functions for accurate signal inversion

Mark A. Kanaparthi[1], and Suresh Dhaniyala[2]

[1]Department of Physics and Engineering, Franics Marion University, Florence, SC, 29506, USA
[2]Department of Mechanical and Aeronautical Engineering, Clarkson University, Potsdam, NY, 13699, USA
Keywords: SEMS Transfer Function

Presenting author email: mark.kanaparthi@fmarion.edu

Particle size distributions obtained with a Scanning Electrical-Mobility Spectrometer (SEMS) are based on the response of charged particles in an applied electric field. A complete operation of SEMS instrument for particle sizing involves the exposure of charged particles to an exponentially increasing voltage (up-scan) followed by an exponentially decreasing voltage (down-scan). Accurate calculation of particle size distributions from SEMS measurements requires knowledge of the instrument transfer function or Kernel as a function of its operating conditions and subsequently, the inversion of an integral equation. A semi-theoretical transfer function calculation approach based on particle arrival-times was shown to accurately characterize fast up-scan SEMS operation. In this paper, we extend the arrival-time calculation approach for SEMS down-scan operation. The combination of a decreasing voltage over time and a parabolic velocity field results in particle trajectories that are fundamentally different from the up-scan operation. However, when smearing due to downstream transport of particles to the detector is considered, the down-scan transfer functions are seen to be a mirror image of the up-scan transfer functions in the mobility space (Figure 1). This suggests that the inversion algorithms optimized for fast up-scan operation could also be applicable for fast down-scan operation. The combination of near real-time up-scan and down-scan transfer functions should enable fast, and accurate size distribution measurements under a range of operating conditions.

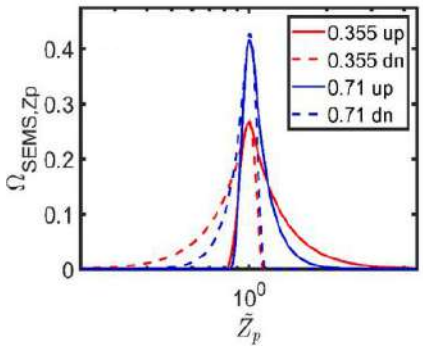

Figure 1: The smeared mobility TF of up-scan and down scan for different scan times (normalized to the average residence time).

As SEMS typically uses a sequentially scanning mechanism with a flat hold in between subsequent scans, it is understood that the initial stage of the upscan is contaminated by the downscan and vice versa. But, the impact of the previous scan on the present scan is poorly understood. This lacuna in understading the contaminated region of the scan leads to, in most cases, an erroneous inversion result.

In our presentation, we show how the present scan is impacted by the previous scan with an understanding of the impact of the hold time on subsequent scan operations. The results will enable researchers to determine the portion of the scan that can be used for signal data inversion, which is unaffected by the previous scan.

In addition, we show how different segments of the upscan and the downscan can be used to obtain a size distribution with a wider size range.

This work was supported by National Science Foundation (NSF Grant Number: AGS-1126361)
Mark A. Kanaparthi, Suresh Dhaniyala,
Fast SEMS size distribution measurements under down-scan operation, Journal of Aerosol Science, Volume 169, 2023, 106133, ISSN 0021-8502,
https://doi.org/10.1016/j.jaerosci.2022.106133.

Solid or Liquid? Substances to use in a CPC to make ultrafine particles detectable

P.Weber[1], S. Kirchhoff[1], O. F. Bischof[1,2], A. Petzold[1] and U. Bundke[1]

[1]Forschungszentrum Jülich GmbH, Institute of Climate and Energy Systems 3 – Troposphere (ICE-3)
[2]TSI GmbH, Particle Instruments, Aachen, Germany

Keywords: Condensation Particle Counter, Working Fluid, Aerosol Measurement

Presenting author email: p.weber@fz-juelich.de

Condensation particle counters (CPCs) are indispensable tools in aerosol science.

From industrial environments to urban centers, aerosol nanoparticles present significant risks to both manufacturing integrity and public health. This has necessitated the development of advanced monitoring technologies capable of high-precision detection without the use of hazardous working fluids, such as butanol.

The detection efficiency and lower size limit of a CPC are fundamentally governed by the thermodynamic properties of the working fluid—specifically its vapor pressure and surface tension. These physicochemical characteristics dictate the supersaturation levels required to initiate heterogeneous nucleation on the sampled nanoparticles. Thus, the performance of a CPC is governed by its operational conditions, internal parameters, and the working fluid used. These internal parameters include the temperature at which the working fluid evaporates in the saturator and condenses on the particles in the condenser, as well as the temperature difference between the two.

We have identified dimethyl sulfoxide (DMSO) as a natural, safe and sustainable alternative to butanol. With only minor modifications to current alcohol-based CPCs, we demonstrated that it can be used as a reliable working fluid. Two studies (Weber et al 2023; Kirchhoff et al 2025) examined DMSO in depth as a working fluid. As these studies focused primarily on its use onboard aircraft, there was an emphasis on low pressure measurements. Here, we present similar data for near standard atmospheric conditions. Additional advantages include very low consumption, very high achievable oversaturation and, as a potential result, a lower particle size detection limit (cut-off).

Furthermore, we would like to present a novel instrument development that is in its initial prototype stage, the sublimation particle counter (SPC). This instrument does not require any liquid operating materials yet is still based on the principle of particle growth through material deposition.

Ongoing experiments are investigating the possibility of altering the cut-off efficiency by adjusting the temperature settings and the design of the instrument. We will demonstrate how the performance of the SPC and DMSO-CPC varies at different temperatures, comparing it with a CPC operating with butanol (5.411, Grimm Aerosol Technik GmbH, Muldestausee, Germany), an electrometer (Model 5.705, Grimm) and a Water-CPC (3789 TSI Incorporated, Shorview, MN, USA).

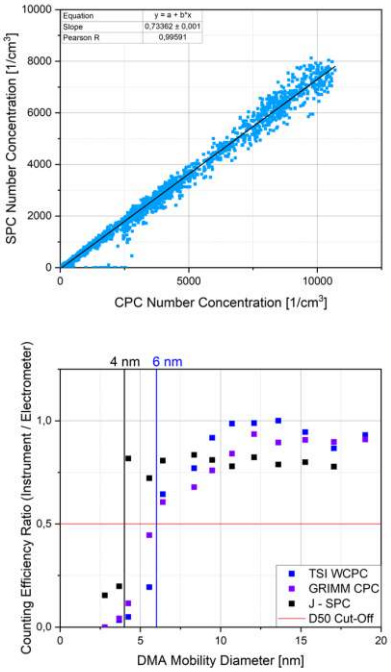

Figure 1. Counting efficiencies curves of the SPC compared to different CPC using NaCl Particles.

This work was supported by the Forschungszentrum Jülich Innovation Fund, Associated Patents are pending.

Sarah Kirchhoff et al. egusphere-2026-127 [in submission]

Weber, P., Bischof, O. F., Fischer, B., Berg, M., Schmitt, J., Steiner, G., Keck, L., Petzold, A., and Bundke, U., 2023. *A new working fluid for condensation particle counters for use in sensitive working environments*, Aerosol Research, 1, 1–12, https://doi.org/10.5194/ar-1-1-2023

A new single-channel portable water CPC

L. Bustin[1], D. Troolin[2], T. Tritscher[1], O.F. Bischof[1], Rzeszutek M.[3], Jagoda P. [3], Nędzka M. [3], Bartyzel J. [3], N. Bock[2]

[1]TSI GmbH, Neuköllner Strasse 4, 52068 Aachen, Germany
[2]Research and Analytical Instruments, TSI Inc., St. Paul, MN, 55126, USA
[3]AGH University of Science and Technology, Cracow, Poland

Keywords: UFP monitoring, mobile measurement, WCPC

Presenting author email: lucia.bustin@tsi.com

The water-based condensation particle counter (WCPC) has been in wide use since about 2004 when a continuous flow CPC that uses water as its condensation fluid was introduced by Hering and Stolzenburg (2004).

Since then, a number of commercial instruments based on this technology have been introduced for continuous measurement of ultrafine particles. In this work, we describe a new compact and portable, single-channel WCPC (model 3001) that brings WCPC technology to mobile measurements. We also describe measurements taken with the dual-channel version of this compact, portable WCPC (model 3002) aboard an aerial drone for atmospheric air quality measurements.

3001 Performance characterization

The 3001 and 3002 use the same core technology at the TSI model 3789 versatile water CPC in a miniaturized format.

The detection efficiency of the single-channel partable WCPC (Model 3001) was characterized through the implementation of the setup shown in Fig 1. Five 3001 units were tested simultaneously on monodisperse NaCl particles generated in a tube furnace and classified by a 3082 classifier and 3085 differential mobility analyzer (DMA).

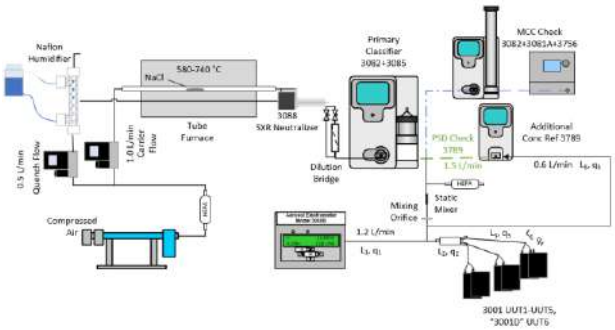

Figure 1: Setup to characterize five 3001 OmniCount units for counting efficiency using NaCl aerosol.

The results were compared with a 3068B aerosol electromter and compiled. The detection efficiencies, and the resulting curve fit, can be seen in Fig. 2. The detection efficiency is greater than 50% for all units at 10nm.

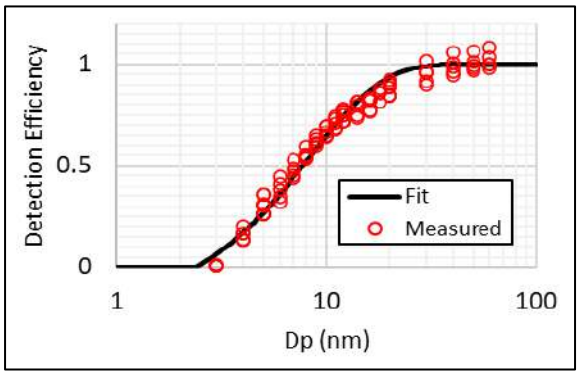

Figure 2. Particle detection efficiency.

3002 Aerial drone meaurements

A dual channel 3002 was attached to a drone and measurements of particle concentrations in the atmosphere were taken on the campus of the AGH University of Krakow.

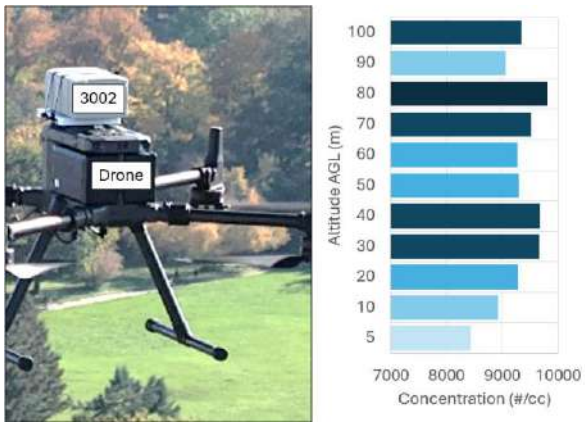

Figure 3. A 3002 attached to an aerial drone taking concentratrion measurements at altitude.

The 3001 WCPC characterization as well as the drone measurement results will be discussed in more detail in the conference presentation.

Hering, S. V., & Stolzenburg, M. R. (2004). Continuous, Laminar Flow Water-based Particle Condensation Device and Method. *U.S. Patent* 6,712,881, issued March 30, 2004.

Behavior of Particle Deposits on Pipelines under Wind Cross-Flow Conditions

Nikoleta Ioannidou[1] and Konstantinos E Kakosimos[1]

[1] Department of Chemical Engineering, Aristotle University of Thessaloniki, Thessaloniki, 54124, Greece

Keywords: particle entraiment, wind tunnel, cylindrical surfaces, quantitative image analysis

Presenting author email: nikoletai@cheng.auth.gr

Understanding particle behavior on curved surfaces, such as pipes, can be critical for industrial applications (Nasir *et al*., 2012; Vashisth *et al*., 2008), especially concerning dust explosions (Eckhoff *et al*., 2021) yet existing research predominantly focused on flat surface interactions (Yook *et al.,* 2010; Adamczyk *et al.,* 2024), with notable exceptions the study of deposit growth dynamics on cylinders in cross-flow (Konstandopoulos, *et al*., 1998; Kostoglou *et al.*, 2000). This study presents the methodology and preliminary results of a quantitative analysis of particle deposition on and resuspension from cylindrical surfaces under dynamic wind loading conditions.

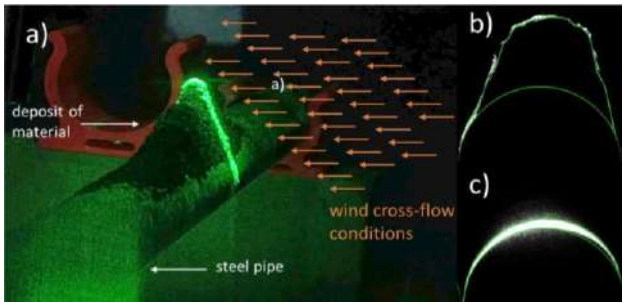

Figure 1. a) Indicative photo of a dust sample loaded on ½" pipe illuminated by the laser-sheet; and processed images with the automated dust-pile profile detection/ quantification b) before, and c) after the test.

Experiments took place in a wind tunnel (with testing volume of 1000x400x400 mm^3, and air velocity uniformity of 15%, established using a DISA 55M01 hot-wire anemometer) using commercial galvanized steel pipes of two internal diameters (1/2" (12.7 mm) and 1" (25.4 mm)). Three particle samples with distinct Geldart Classifications were investigated: calcium oxide (CaO, type A), two types of biochar (type A), and wheat flour (type A). Various quantities of particles were loaded on the pipe by the fixed funnel method (Müller *et al.,* 2021), followed by dynamic air velocity ramping from 0-10 m/s over 10 minutes (Fig. 1a). The ramp rate and velocity range were explored over screening test.

Each test was recorded with a camera (TIS, 1280 × 960 px, 30 FPS) capturing a side (lateral) view of the sample. The collected images were processed using an automated image analysis framework employing Canny edge detection with bright-spot masking and coordinate transformation (in-house developed in Python 3.13.13 with OpenCV 4.13.0) and Savitzky-Golay smoothing (SciPy 1.17.0) to ensure robust profile (Fig. 1b and c) extraction despite optical noise. Multiple metrics include particle loadings and pile profile area, maximum height, full-width-half-maximum (FWHM), and angle of repose with sub-pixel precision (0.5mm).

Critical air velocities for complete collapse of the particle pile were highly material-dependent (Table 1). These findings suggest that particle properties play a more significant role than surface curvature effects within the investigated size range. Additionally, larger initial particle loadings correlated with lower critical removal wind speeds.

Table 1. Critical entrainment air velocity.

	1 inch pipe		½ inch pipe	
Material	**Mean (m/s)**	**std (m/s)**	**Mean (m/s)**	**std (m/s)**
BioChar	9.54	0.96	-	-
BioChar V2	11.80	1.03	9.95	1.77
CaO	15.26	1.50	12.04	1.47
Plain Flour	13.18	2.59	12.51	2.03

An ongoing dimensional analysis aims to consolidate the preliminary findings in order to provide quantitative insight into industrial applications. Nonetheless, the developed automated methodology enables characterization of particle-surface interactions with precision, offering potential for broader applications in powder handling, pharmaceutical processing, and environmental particle transport.

Boor, B.E., et al. (2013). Wind Tunnel Study on Aerodynamic Particle Resuspension. *Aerosol Science & Technology*. **47**, 848-857.

Eckhoff, R. K., & Li, G. (2021). Industrial Dust Explosions. A Brief Review. *Applied Sciences*. ***11***(4), 1669.

Konstandopoulos A. G., et al. (1998). Shape evolution of particulate deposits growing on cylinders in cross flow. *World Congress on Particle Technology* 3, No. **284**, IChem.E, Brighton, England.

Kostoglou M., et al. (2000). Particulate deposit shape evolution on cylinders in cross-flow at high stokes numbers. *Aerosol Science*. **31**, 427-436.

Müller, D., Fimbinger, E., Brand, C. (2021) *Powder Technology*. **383**, 598-605.

Nasir, H., et al. (2012). Computational guidelines and an empirical model for particle deposition in curved pipes using an Eulerian-Lagrangian approach. *Powder Technology*. **53**, 1-20.

Vashisth, S., et al. (2008). A review on the potential applications of curved geometries in process industry. *Industrial & Engineering Chemistry Research*. **43**, 3291-3337.

Yook, S.J., et al. (2010). Deposition Velocity onto an Inverted Flat Surface in a Laminar Parallel Flow. *Aerosol Science and Technology*. **44**, 919-929.

Fabrication of filter paper-based SERS substrates via spark ablation and their applications

V. Horváth[1], M. Darwish[1], Zs. Geretovszky[1] and A. Kohut[1]

[1]Department of Optics and Quantum Electronics, University of Szeged, Szeged, 6720, Hungary

Keywords: spark ablation, plasmonic nanoparticles, surface-enhanced Raman spectroscopy, food safety.

Presenting author email: kohut.attila@szte.hu

As modern society heavily relies on various – potentially harmful – chemicals in production lines, it is increasingly important for quality control and safety regulations to keep up and to find accessible means to reliably assess the composition of end products, especially those potentially affecting consumer health. Well-established, highly sophisticated techniques are available in laboratory settings for trace chemical analysis, however, cheap and field deployable strategies enabling high-throughput screening still attract a lot of interest. Surface-enhanced Raman spectroscopy (SERS), combining chemical identification with high sensitivity and handheld instrumentation, offers an appealing approach for the above task. The experimental apparatus for Raman spectroscopic measurements is well-developed, capable of routine applications outside the laboratory, however, the availability of suitable SERS substrates facilitating low-concentration measurements is still questionable. There are various strategies for the fabrication of SERS substrates with different properties that come with different levels of sophistication, performance, and cost. In our view, there is not a "one-size-fits-all" solution in this field and aerosol-based fabrication methods – and spark ablation in particular – are highly suitable in many aspects. We present our results related to the fabrication of SERS substrates via spark ablation based on ordinary laboratory paper filters, the optimization of the substrate performance and a few examples for their applications in detecting traces of pesticides in real samples.

Spark ablation is based on the periodic spark plasma-initiated erosion of two bulk electrodes in a controlled atmosphere, resulting in highly pure nanoparticles with tunable size, composition and crystal structure (Schmidt-Ott, 2019). Since it is an atmospheric pressure process, the resulting aerosol is compatible with standard filtration techniques, thus nanoparticles can simply and effectively be collected in filter media. We have shown the possibility of using particle-loaded filters as SERS substrates with tunable enhancement properties without any additional post-processing steps (Kohut *et al* (2020)). We have also explored the effects of generation conditions – including carrier gas composition, sparking frequency, deposition time – and filter properties – such as effective pore size and material – on the substrate performance and optimized the fabrication process to achieve sub-ppm limit of detection (LOD) for pesticides, such as thiram and thiabendazole (TBZ) (Kohut 2023, Horváth *et al* 2025). To test the applicability of these substrates in food safety for the trace chemical analysis of pesticides outside specialized laboratories, we studied the LOD of TBZ in a real, untreated apple juice matrix. As qualitatively shown in Figure 1, the SERS signal follows the decreasing TBZ concentration down to ca. 0.1 ppm. A deeper analysis also revealed that the filter performance allows for the quantitative TBZ detection with good accuracy (relative standard deviation in the range of 8-10%).

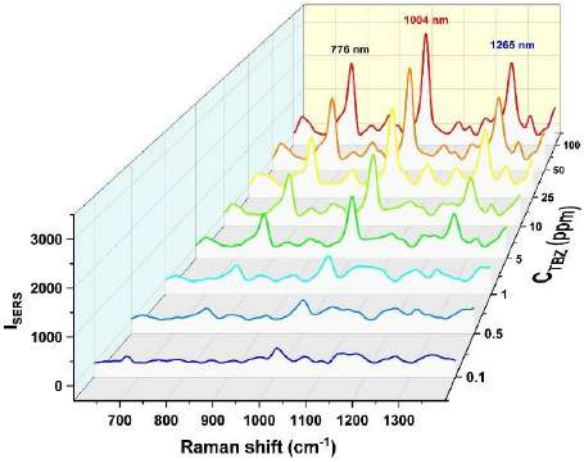

Figure 1. SERS spectrum of different concentrations (0.1-100 ppm) of TBZ in apple juice.

We also show that the filter medium, serving as the base of the SERS substrates, compatible with the effective sampling of gas-phase analytes, further increasing the range of potential applications.

Funding for this work was provided from the National Research, Development and Innovation Fund under the 2022-2.1.1-NL Creation of National Laboratories, Complex Development funding scheme (project 2022-2.1.1-NL-2022-00012).

Schmidt-Ott, A. (ed.) (2019) *Spark Ablation*, Jenny Stanford Publishing.

Kohut *et al* (2020) *Applied Surface Science* **531**, 147268.

Kohut, A. (2023) *Journal of Aerosol Science* **531**, 147268.

Horváth *et al* (2025) *ACS Applied Nano Materials* **8**, 17934–17951.

Key aspects of sizing and counting particles using a Time-Of-Flight technique

A. Kort[1], A. Koched[2], F. Gensdarmes[1], P. Wiszniowski[1], C. Bodiot[1], T. Tritscher[3]

[1] Autorité de Sûreté Nucléaire et de Radioprotection (ASNR), PSN-RES/SCA/LPMA, F-91400, Saclay, France
[2] TSI France Inc, Hôtel Technologique BP100, Technopole de Chateau Gombert, 13382 Cedex 13 Marseille, France
[3] TSI GmbH, Neuköllner Strasse 4, 52068 Aachen, Germany

Keywords: time of flight, aerodynamic diameter, particle size distribution

amel.kort@asnr.fr

Real particles often deviate from the ideal assumptions of spherical shape and standard density (1000 kg m^{-3}), which can influence particle-sizing techniques. The equivalent aerodynamic diameter is defined as the diameter of a sphere with standard density that settles at the same terminal velocity as the particle of interest and can be measured with a Time-Of-Flight (TOF) technique using an Aerodynamic Particle Sizer (APS™ TSI Incorporated, USA). In this study, six instruments model 3321 were considered to test their performances.

The key aspects of counting and sizing using this instrument include verification of sample and sheath flow rates, zero-count measurements, sizing validation using traceable monodisperse calibration particles and finally unit-to unit variability of the Particle Size Distribution (PSD) for polydisperse particles. Drifts in the operating settings of the units were detected and the impact of this drift on the sizing results was discussed. In this work two type of powders were tested: a polydisperse bimodal SPM-102™ (Al_2O_3) powder and a multimodal Ballotini™ (hollow glass spheres) powder with complex optical properties. All the results of these different aspects will be presented during the conference. In this abstract we will focus on the PSD measurement (sizing) of the Ballotini™ powder.

The test bench used for the tests is a closed loop air duct, into which the aerosol is injected using a rotating brush generator (RBG 1000™, PALAS®) and mixed with a particle free dilution stream air flow set to 250 m^3/h. A bipolar Electrostatic Aerosol Neutralizer (EAN 581™, TOPAS® GmbH) was added to the setup.
The particles end up in a mixing chamber including multiple vertical sampling probes positioned at different locations (Brochot, 2012). The six APS™ units were positioned underneath the test bench connected to dedicated sampling probes. An evaluation of particle losses in the sampling lines was performed experimentally and confirmed that neither the size distribution nor the total concentration of the particles measured were affected by losses or size modification.

The PSDs, averaged over a duration of 15 min of acquisition time, for the Ballotini™ powder are shown in Figure 1. All PSDs show an aerosol with a wide range of sizes up to 10 µm. However, the sizing results for the hollow glass spheres show unit-to-unit discrepancies.

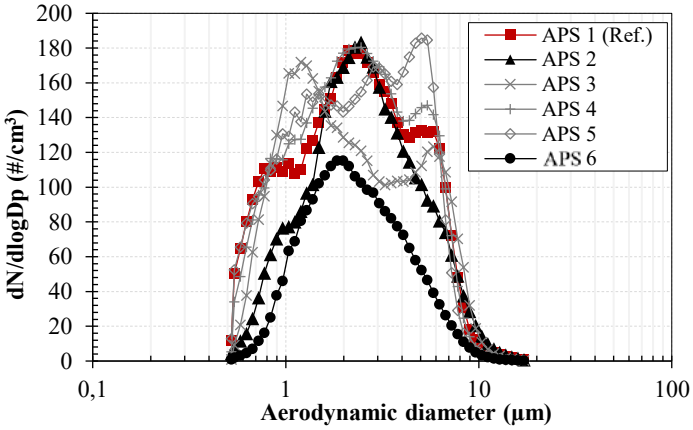

Figure 1. Time averaged PSDs of the Ballotini™ hollow glass spheres as measured by all APS™ units.

The number of modes detected varies from unit to unit. In fact, APS 1 (reference unit) and 4 show a good overlap of the distribution with a main mode detected at 2 µm, a second mode at 6 µm and a third one at 0.8 µm. APS 5 also shows three different modes at 5 µm, 3 µm and 1.5 µm. However, the PSD measured by APS 3 is found skewed in the opposite side compared to APS 1, 4 and 5 with two modes at 1.5 µm and 6 µm. APS 2 and 6 measure different distributions and concentration levels compared to the other units with a quasi-monomodal symmetric PSDs showing a main mode around 2 to 2.5 µm close to the main mode detected by the reference unit APS 1.

The sizing results confirm that drifts in the APS™ operational parameters can alter the response of the TOF measurement principle, thereby reducing its effective independence from the physical properties of the particle. Such effects can introduce systematic sizing biases, which may be further exacerbated when measuring non-spherical particles or particles with complex shape morphologies and optical properties.

Brochot C.PhD Thesis , *University of Lorraine, IRSN, LRGP, INRS, 2012.*

Forensic Aerosol and Particle Technology: Can PDMS Droplets Cause a Fireball?

, Athanasios G. Konstandopoulos[1,2], Ekaterini C. Vagia[2], Chrysa M. Oikonomidou[1,2]

[1]Aerosol & Particle Technology Laboratory, Aristotle University, Thessaloniki, 54124, Greece
[2]SYNEST PC, 19-21 G. Gennimata Str, Thessaloniki, 55535, Greece
Keywords: PDMS droplet combustion, fireball forensics, aerosol kinetics, Tempi railroad crash.

Presenting author email: agk@auth.gr, agk@sy-nest.com

The Tempi railroad crash (Wikipedia, 2026) involved the collision of two electrically powered trains, following which, within fractions of a second, a rapidly developing fireball appeared after, raising the question of whether PDMS-based transformer oil aerosol, released from damaged railway transformers could have acted as the causative fuel. Here, we simulate the kinetics of PDMS thermal-degradation behavior directly from our own experimental thermogravimetric curves as well as the literature (Camino et al, 2001) obtained in both nitrogen and air over matched heating rates. The kinetic model describes all data sets very well (Figure 1) and it was embedded in a coupled droplet heat-transfer and decomposition model, together with transport-based screening models for volatile release, near-droplet cloud formation, and post-source continuation. The analysis incorporates material properties of the actual PDMS oil (Baysilone M50 EL) at operating temperature and explores droplet diameters from 0.1 to 5 mm under quiescent and impact-induced high-flow conditions. The calculations show that mm-scale PDMS droplets are too slow to reach near-complete decomposition within the observed O(10^{-1}) s time window, even at very high ambient temperatures; only very fine droplets of about 100–200 µm approach this timescale, and only in very hot (>900 °C) environments. Extending the analysis from single droplets to sprays shows that transient cloud accumulation becomes conditionally plausible only if a dense droplet population enters an already very hot, weakly ventilated, small local volume. However, when the external hot source is removed, robust self-sustained combustion is not supported. The results therefore do not support PDMS transformer oil as a primary standalone explanation for the Tempi fireball. At most, PDMS may be viewed as a conditional secondary contributor under already established extreme thermal conditions by the fireball, the cause/origin of which needs to be searched elsewhere. More broadly, the work demonstrates how aerosol and particle technology, combined with experiment-based kinetics, can constrain forensic fire scenarios.

.

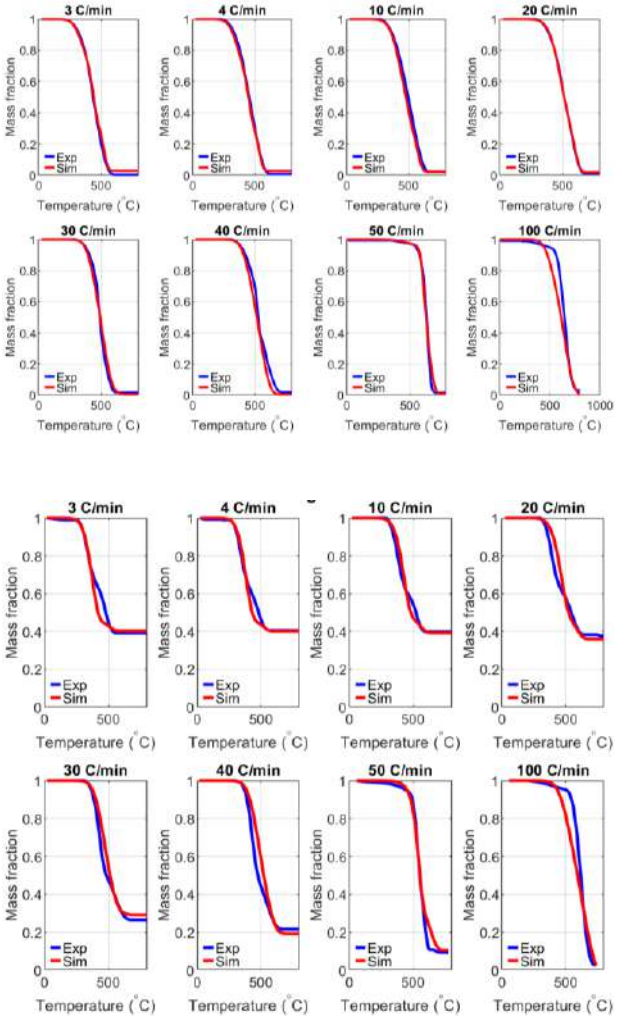

Figure 1. Thermogravimetric measurements of PDMS pyrolysis in N_2 (top) and oxidation in air (bottom) vs kinetic model simulations.

This work is dedicated to the memory of the victims of the Tempi railroad crash.

Wikipedia (2026) Accessed on March 30, 2026, https://en.wikipedia.org/wiki/Tempi_train_crash.

Camino, G. Lomakin, S.M. Lazzari, M. (2001) Polymer **42** 2395-2402.

Diffusion dynamics of tiny nanoparticles in air

D.G. Tsalikis[1], and S.E. Pratsinis[1,2]

[1]Institute of Nuclear and Radiological Sciences and Technology, Energy and Safety, NCSR Demokritos, GR-15341, Greece

[2]Department of Mechanical and Process Engineering, ETH Zürich, CH-8092, Switzerland

Keywords: diffusion, nanoparticles, simulation, molecular collisions.

Presenting author email: tsalikis.d@gmail.com

Modeling O_2 and N_2 as diatomic molecules with realistic geometries and force fields reveals that their trajectories are not rectilinear sequences as predicted by the classical kinetic theory of gases. Gas molecules can separate but quickly re-collide multiple times without interacting with other molecules in between (Tsalikis et al., 2023). This leads to multibody, grazing and orbiting-like collisions, as envisioned by Hirschfelder et al. (1964).

Building on this new quantitative understanding of gas dynamics (Tsalikis et al., 2023), the diffusivity of tiny silica nanoparticles (NPs) in air was examined using fully atomistic (FA) molecular dynamics (MD) that accounted for detailed attractions between NPs and air molecules as well as the diatomic structure of the latter (Karadima et al., 2025). Simulations were performed with a fully atomistic force field for the NPs (Barbier et al., 2004) and ambient air (Tsalikis et al., 2023) under dilute conditions, with a nanoparticle volume fraction less than 10^{-4}. Additional simulations were conducted modeling air and NPs as hard spheres (HS-MD) undergoing only elastic collisions, consistent with classical kinetic theory, at exactly the same conditions and compositions as the FA-MD ones.

Analysis of the FA-MD trajectories reveals that as NPs approach the size of air molecules, their transport becomes increasingly affected by inelastic collisions with them (i.e., grazing and orbiting-like collisions) that were abundant between NPs and air, similar to those foreseen by Hirschfelder et al. (1964) and quantified for the first time by Tsalikis et al. (2023) for gas-molecule collisions. The NP Brownian – rotational movement was particularly fascinating, however! Figure 1 illustrates the motion of a 1.5 nm-diameter NP diffusing in air. The white line shows the trajectory of the NP's centre of mass, while the grey line depicts the motion of one of its surface silicon (Si) atoms, thereby elucidating the NP's rotational motion. The NP changes direction due to repeated collisions with air molecules, highlighted in four snapshots. Multi-body collisions are also observed at these times (e.g., t = 0.72, 1.22, and 1.42 ns). Additionally, air molecules (colorful dumbbells in Fig. 1) can "adsorb" onto the NP's surface for several hundred picoseconds before detaching. For example, in Figure 1, an N_2 molecule (blue) collides with the NP at t = 1.22 ns and stays "adsorbed" for 0.2 ns.

The diffusivities obtained from the HS simulations align closely with those predicted by the Epstein (Epstein, 1924) and Stokes-Cunningham-Millikan (SCM) equations (Jung et al., 2012), thereby further validating the current simulations. In contrast, diffusivities from FA MD simulations are systematically 50–60% lower than those predicted by the SCM equation (Karadima et al., 2025). For sub-5 nm nanoparticles, diffusion coefficients calculated via HS molecular dynamics show consistent deviations from SCM estimates, corroborating Tammet, (1995). Additional simulations, in which atomic-scale details and intermolecular attractions were omitted, and nanoparticles and air molecules were modeled as perfect elastic spheres, resulted in diffusivities that also closely matched predictions from the SCM and the Epstein equation.

Figure 1. The trajectory of a 1.5 nm silica NP (in red and yellow bonds) diffusing in air with snapshots at 0.13, 0.72, 1.22 and 1.42 ns with colliding gas molecules (yellow, red, blue, and orange dumbbells).

This project has received funding from the European Research Council (ERC) under the European Union's [Horizon 2020/Horizon Europe] research and innovation programme (grant agreement No. 101200261).

References

Barbier, D., Brown, D., Grillet, A.C., Neyertz, S. (2004) *Macromolecules* **37**, 4695-4710.

Epstein, P.S. (1924) *Phys. Rev.* **23**, 710-733.

Hirschfelder, J.O., Curtiss, C.F., Bird, R.B. (1964) *Molecular theory of gases and liquids*. Wiley.

Jung, H., Mulholland, G.W., Pui, D.Y.H., Kim, J.H. (2012) *J. Aerosol Sci.* **51**, 24-34.

Karadima, K., Tsalikis, D.G., Mavrantzas, V.G., Pratsinis, S.E. (2025) *J. Phys. Chem- A.* **129,** 5127−5136.

Tammet, H. (1995) *J. Aerosol Sci.* **26**, 459–475

Tsalikis, D.G., Mavrantzas, V.G., Pratsinis, S.E. (2023) *Phys. Fluids* **35**, 097131.

Electrodynamic Particle Suspension in a Gap Between Grid Electrodes

K. Mehrabi, F. J. Higuera

Department of Fluid Mechanics, Universidad Politécnica de Madrid, 28040 Madrid, Spain
Keywords: Electrodynamic suspension, continuum regime, grid electrodes, linear stability.

Presenting author email: karim.mehrabi@upm.es

Electrodynamic particle suspension is a technique for generating suspensions of electrically conducting particles using electric rather than aerodynamic forces. The suspension forms in the gap between two horizontal grid electrodes when a DC voltage exceeds an onset at which the electric force on a particle resting on the lower electrode (Maxwell, 1881) overcomes its weight and adhesion. The particle then detaches and moves upward across the gap. Upon reaching the upper electrode, it may either pass through the grid, with a probability defining the grid transparency, or strike the metal and acquire the electrode potential. This reverses the electric force, causing the particle to fall back to the lower electrode and repeat the cycle. Particle losses through the upper electrode are continuously replenished by newly suspended particles deposited on or entering through the lower electrode. An upward gas stream injected through the lower electrode and withdrawn through the upper one assists in carrying suspended particles out of the gap.

With many particles suspended, the electric field induced by their charge opposes the applied field in the lower part of the gap, reducing the net field at the lower electrode to the minimum required for resuspension. This balance determines the number of suspended particles per unit electrode area as a function of the applied voltage.

Particles carrying different charges move at different velocities and collide, redistributing charge in a manner dependent on the local electric field. At sufficiently high voltages, the mean free path between collisions becomes small compared with the interelectrode distance, and the suspension approaches a local equilibrium over most of the gap. In this regime, the charge distribution depends on the local electric field and on the particle number and charge densities conserved in collisions, while the suspension also approaches quasi-neutrality. The large-scale dynamics are described by hydrodynamic equations for the conserved quantities (Higuera 2018; Ling and Higuera 2022), coupled with a Poisson equation for the electric potential and mass and momentum conservation equations for the gas.

Stationary solutions were computed and their linear stability analyzed. As shown by the stability map (Fig. 1), the suspension is stable at low voltages but becomes unstable above a critical threshold. This limit is expressed as a critical voltage $V_c = f(E_m)$. For a given electric field, operating points above the stability limit lead to transient electrohydrodynamic plumes. The results show that there is no solution for voltages below $E_m L$, where L is the gap width.

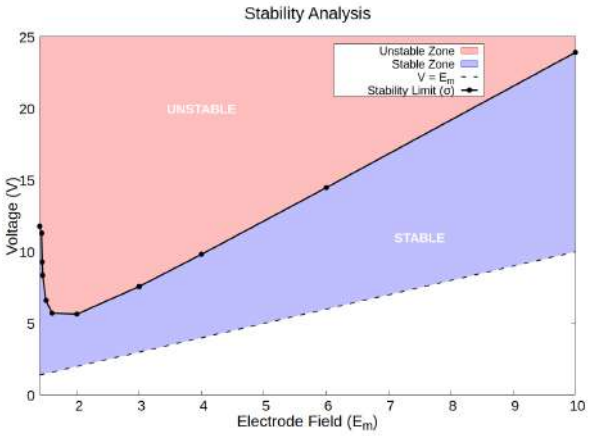

Figure 1. Stability map

This work was supported by the Spanish MCIN/AEI/10.13039 under grant PID2023-150329NB-C22.

Higuera, F. J. (2018), *J. Fluid Mech*. **854**, 261-291.

Ling, H. and Higuera, F. J. (2022), *J. Aerosol Sci.* **163**, 105985.

Maxwell, J. C. (1881), *A Treatise on Electricity and Magnetism,* Oxford University Press.

New slip model for spherical particle-wall rolling detachment by airflow

A. Sellier[1], A. Louchami[1,2] and F. Gensdarmes[2]

[1]LadhyX, Ecole Polytechnique, 91129 Palaiseau Cedex, France [2]Autorité de Sûreté Nucléaire et de Radioprotection (ASNR), PSN-RES/SCA/LPMA, F-91400, Saclay, France
Keywords: slip, sphere, resuspension, airflow.

Presenting author email: francois.gensdarmes@asnr.fr

Particle resuspension by turbulent airflow is usually described by models which use classical expression derived by O'Neill (1968) to calculate the drag and the torque on a spherical particle in contact with a wall when held fixed in a shear flow. Such approach does not take account of slip both on the sphere and the wall. Yu & Hu (2021) integrated such slip condition in the Rock'nRoll model using the Navier (1823) slip model on the wall and the Cunningham factor to correct both the drag and the torque on the particle. Nevertheless, these corrections are not supported by fluid mechanics considerations. Thus a new model for a slip motionless sphere at contact with a plane slip wall and immersed in a shear flow is here proposed (see figure 1 insert).

The sphere has a radius R, a centre C with distance $h = \tilde{h} \cdot R$ to the wall. The slip on the surfaces is described by the Navier condition with slip lengths $\lambda_w = \tilde{\lambda}_w \cdot R$ on the wall and $\lambda_p = \tilde{\lambda}_p \cdot R$ on the sphere. The creeping flow excerts on the particle a drag force and a torque about its centre with magnitude $F_d = 6\pi\mu\dot{\gamma}R^2(\tilde{h} + \tilde{\lambda}_p) \times f$ and $\Gamma(C) = 4\pi\mu\dot{\gamma}R^3 \times c$, respectively. Here $\dot{\gamma}$ is the shear rate, μ is the dynamic viscosity, f and c are key friction coefficients. The Faxén generalized formulae derived by Keh & Chen (1996) show that far from the wall ($\tilde{h} = \infty$) $f_\infty = (1 + 2\tilde{\lambda}_w)/(1 + 3\tilde{\lambda}_w)$ and $c_\infty = 1/(1 + 3\tilde{\lambda}_w)$. The friction coefficients f^* and c^* for no slip on the sphere ($\tilde{\lambda}_p = 0$) at contact with a slip wall are calculated here by the bipolar coordinates method and thereby interpolated by handy formulae. The slip on the sphere at the contact with the wall ($\tilde{h} = 1$) is here considered by the formulae $f = f^* \times f_\infty \left[\frac{16+9f_\infty}{25}\right]$ and $c = \frac{c^*}{1+3\tilde{\lambda}_s}$ (Sellier *et al.*). We showed that such a simple model is in perfect agreement when extrapolating results obtained by Luo & Pozrikidis (2008) using a quite involved boundary layer method.

Particle detachment occurs when $\Gamma_t = R \cdot F_d + \Gamma(C) > a \cdot F_{ad}$ where a is the distance of roughness asperities and F_{ad} the adhesion force. Finally, we express the ratio β between the hydrodynamic total moment exerted on the sphere with and without slip on the sphere and the wall $\beta = \frac{\Gamma_t}{\Gamma_t(\tilde{\lambda}_w=0,\ \tilde{\lambda}_p=0)}$. This ratio is plotted in figure 1 for equal dimensionless slip lengths on the wall and the particle $\tilde{\lambda}_w = \tilde{\lambda}_p$. The Yu & Hu approach is also represented for comparison using the accommodation coefficient, σ = 0.93, deduced from their paper. Note that Maxwell (1879) relates dimensionless slip length for a plane $\tilde{\lambda}_w$ to the Knudsen number Kn as a function of σ ($\tilde{\lambda}_w = Kn$ for $\sigma = 1$).

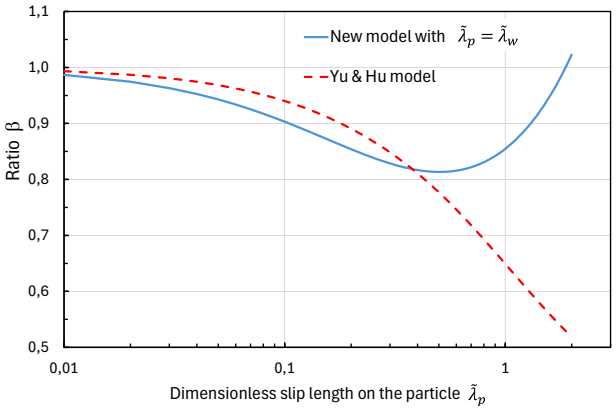

Figure 1. β versus the non-dimensional slip length

The new model predicts a decrease of β when increasing $\tilde{\lambda}_p$ below 0.5 which means that slip reduces the global hydrodynamic efforts on the particle. For slip length value above 0.5, the β ratio surprisingly increases. This can be explained by an increase of the ambient velocity at the sphere center, due to slip length on the wall, and by a reduction in the torque contribution due to slip on the particle. This trend is not predicted by the Yu & Hu approach because the slip effect on the torque value is not well assessed.

Keh, H., and Chen, S. (1996) *European Journal of Mechanics B-Fluids*, 15, 791-807.
Luo, H. and Pozrikidis, C. (2008) *J. Eng. Math.*, 62, 1-21.
Maxwell, J. C. (1879) *Philos. Trans. R. Soc.*, 170, 231-256.
Navier, C. L. (1823) Mémoires de l'Académie Royale des Sciences de l'Institut de France. pp. 389-440.
O'Neill, M. E. (1968) *Chem. Eng. Sci.*, 23, 1293-1298.
Sellier, A. *et al*. In preparation, *to be submitted J. Fluid Mechanics.*
Yu, D. and Hu, F. (2021) *J. Aerosol Sci.*, 151, 105675.

On the relation between turbulent parameters and aerosol deposition

J. Malet[1], J. Wiese[1]

[1]ASNR, PSN-RES/SCA/LEMAC, F-91400 Saclay, France
Keywords: aerosol, deposition, turbulence

Presenting author email: Jeanne.malet@asnr.fr

Aerosol transport and deposition result from the interaction between turbulent carrier flows and inertial particles, particularly in complex geometries such as bends or T-junctions. In these configurations, curvature-induced secondary flows, flow separation, and strong near-wall velocity gradients profoundly modify particle trajectories and deposition mechanisms. Despite extensive literature, large discrepancies up to three orders of magnitude (Mehel *et al.* 2010) remain between reported deposition data, especially for bend flows. Recently, Wang *et al.* (2024) revisited the deposition experiments in bends originally performed by Pui *et al.* (1987) and reported differences of up to a factor of two.

Many influencing parameters have been discussed in the literature, but detailed turbulence-related quantities are rarely analysed in aerosol studies. Experiments often rely on small-scale geometries, such as aerosol sampling tubes, where access to turbulent flow is limited and turbulence validation is difficult. Moreover, such measurements require instrumentation generally unavailable in aerosol laboratories. Another reason is that the numerical tools commonly used for analysis often do not provide access to advanced turbulence modelling or detailed turbulence diagnostics beyond global quantities.

In the present work, a large-scale approach is deliberately adopted to enable experimental validation of turbulent flows. This makes it possible to exploit physically meaningful CFD results based on a Reynolds Stress Model (RSM), which allows access to detailed flow and turbulence parameters beyond turbulent kinetic energy, to interpret experimental aerosol deposition.

In the present work, a large-scale approach is adopted to enable experimental validation of turbulent flows. This allows physically meaningful CFD results using a Reynolds Stress Model (RSM), providing detailed turbulence parameters beyond turbulent kinetic energy to interpret aerosol deposition. Experiments are conducted in a large rectangular duct at bulk Reynolds numbers of ~10^5, including smooth-curvature bends, sharp-edged bends, and a bend with a deflector. Nearly monodisperse NaCl aerosols (2–6 µm) are injected, and local deposition is measured directly on duct walls, preserving surface and boundary layer characteristics.

The experiments reveal significantly higher deposition in sharp-edged bends than in smooth-curvature bends, with strongly non-uniform deposition patterns. Associated flow measurement are presented, with detailed characterisation down to boundary layer, as presented on the figure below, in order to give strong confidence to the modelling.

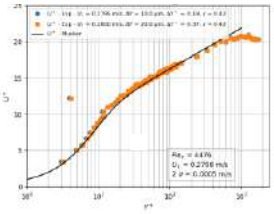

Figure 1. Vertical boundary layer velocity profile in a straight duct portion of the facility

To analyse these results, CFD simulations are performed using a single second-order RANS turbulence model (Reynolds Stress Model) with refined near-wall resolution. The flow is examined through turbulence-related quantities such as friction velocity, turbulent kinetic energy, Reynolds stress components, vorticity and turbulence anisotropy. Sharp-edged bends exhibit extended recirculation zones, high turbulent kinetic energy levels and strong anisotropy, particularly on the extrados and in separated regions, while the presence of a deflector substantially modifies these features. Example of vorticity fields are given in figure 2.

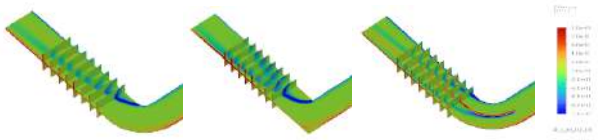

Figure 2. Vorticity fields for different bend shapes

Comparison with experiments indicates that increased deposition correlates with anisotropy and secondary flows rather than global turbulence intensity. Consequently, deposition in such singular flows cannot be fully described by correlations based solely on non-dimensional deposition velocity v_{dep}^{+} versus particle relaxation time τ_p^{+}; a physically consistent description must include local flow topology and turbulence structure.

Pui, D. Y. H., et al. (1987). Aerosol Science and Technology, 7

Wang *et al.* (2024) Aerosol Science and Technology

Mehel *et al.* (2010) Journal of Aerosol Science, 41

Physicochemical characterization and vapor adsorption behavior of jet-like soot particles

Yiheng Liang[1,2], Jon Bell[1], Una Trivanovic[3], Katharina Volz[4], Evelyn Fuhrmann[4], Luca Artiglia[5], Markus Ammann[5], and Jacinta Edebeli[1]

[1]Centre for Aviation, ZHAW Zürich University of Applied Sciences, Winterthur 8401, Switzerland
[2]Department of Environmental Systems Science, ETH Zürich, Zürich 8092, Switzerland
[3]Federal Institute of Metrology METAS, Bern 3003, Switzerland
[4]Malvern Panalytical, Unterschleißheim 85716, Germany
[5]Laboratory of Atmospheric Chemistry, PSI Center for Energy and Environmental Sciences, Villigen 5232, Switzerland
Keyword: jet soot, adsorption, surface chemistry, vapor-particle interactions.

Presenting author email: lian@zhaw.ch

Contrail formation in aircraft exhaust plumes is strongly influenced by the interactions between jet engine soot and co-emitted vapor species, which control water uptake, ice nucleation, and early soot aging. These interactions are governed by the interplay between soot physicochemical and adsorbate properties, making comprehensive characterisation essential for understanding vapor–soot partitioning and the early stages of soot aging in aircraft exhaust plumes (Liati et al., 2014). In this study, jet-like soot particles were synthesised by enclosed spray combustion of jet fuel and systematically characterized to explore the relationships between soot structure, surface chemistry, and the adsorption behavior of polar water vapor and non/weakly polar aromatic volatile organic compounds (VOCs) with increasing molecular volume.

Three jet-like soot samples were prepared with significant variations in surface area, pore structure, and oxygen functional groups. The structural properties were characterized by N_2 physisorption at 77 K, yielding specific surface area (SSA, 85.5 – 324.7 $m^2 g^{-1}$) and pore size distributions showing both micro- and meso-porosity attributed to voids between primary particles. Average primary particle diameters (12 – 19 nm) were measured by transmission electron microscopy (Trivanovic et al., 2022). Surface chemical composition was analysed by X-ray photoelectron spectroscopy (XPS), focusing on C1s and O1s core levels to quantify oxygen-containing functional groups (C–O, C=O, and COOH), while microcrystallite structure was assessed using X-ray diffraction.

Single-component adsorption isotherm of water vapor, benzene, toluene, and o-xylene were measured over 25 – 45 °C and relative pressures of 0.001 – 0.9 p/p°. For aromatic VOCs, the adsorbed amount correlated strongly with SSA across the studies pressure range, indicating adsorption governed primarily by soot surface area. Thermodynamic analysis yielded adsorption enthalpies (-ΔH) of 39.6-53.5 kJ mol^{-1}, consistent with physisorption. In contrast, water vapor adsorption showed weaker SSA dependence at low relative pressures, followed by a sharp increase at p/p° = 0.4, consistent with the Dubinin-Serpinsky model. This behavior correlated strongly with oxygen-containing functional groups concentration identified by XPS, suggesting that water uptake involves initial cluster formation around oxygen functional groups at p/p° < 0.4 , followed by H_2O layering in larger pores at p/p° > 0.4 , which is surface area controlled.

Adsorption kinetics were examined using a stretched exponential model to probe vapor diffusion mechanisms. Aromatic VOCs exhibited relatively rapid uptake, with an average uptake rate constant k = 0.016 s^{-1} and kinetic exponents β of 0.90-1.00, indicating near single-timescale kinetics dominated by external mass transfer through interparticle void. Water vapor uptake was significantly slower (average k = 0.001 s^{-1}) and characterized by lower β values (0.50-0.75), reflecting diffusion limitations associated with intraparticle pore diffusion towards oxygen-containing surface sites. These kinetic differences highlight distinct adsorption mechanisms for polar and non-polar species on jet soot.

Overall, this study establishes clear links between soot surface area, surface chemistry, adsorption thermodynamics and kinetics, and their roles in controlling vapor uptake and diffusion behavior. The results provide an experimental basis for future detailed soot modeling and improved representation of soot aging processes in aircraft exhaust plumes.

This work was supported by the Swiss Federal Office of Civil Aviation in the framework of the 'ADVISAR' project (2021-035), as well as the ZHAW SoE PhD grant.

Liati, A., Brem, B. T., Durdina, L., Vögtli, M., Arroyo, Y., Dimopoulos, P., Wang, J. (2014) Electron microscopic study of soot particulate matter emissions from aircraft turbine engines. Environmental Science and Technology. 48, 10975–10983.

Trivanovic, U., Kelesidis, G. A., Pratsinis, S. E. (2022) High-throughput generation of aircraft-like soot. Aerosol Science and Technology. 56, 732–743.

Inhalable carbon fibres – CF aerosol generation, characterisation, and numerical simulation of deposition on cell surfaces exposed at air-liquid interface

S. Mülhopt[1], M. Hauser[1], M. Wexler[1], J. Mahl[1], W. Baumann[1], S. Klein[1], B. Gutmann[2], C. Schlager[2], T. Krebs[2], and D. Stapf[1]

[1]Institute for Technical Chemistry, Karlsruhe Institute of Technology, Karlsruhe, 76021, Germany
[2]Vitrocell Systems GmbH, Waldkirch, 79183, Germany
Keywords: ALI, air-liquid interface, WHO fibres, aerodynamic diameter

Presenting author email: muelhopt@kit.edu

Carbon fibres (CF) and CF-reinforced plastics (CFRP) are innovative materials, which are increasingly produced, used and therefore recovered and disposed. In these processes particles and fibres which could fulfil the criteria of the World Health Organisation (WHO) to be potentially carcinogenic (so-called WHO fibres, critical aspect ratio > 3:1, length ≥ 5 µm and diameter ≤ 3µm) can possibly be released. This raises serious concerns about potentially harmful effects upon inhalation. Therefore, in this study investigations of CF under thermal and mechanical stress are carried out.

Polyacrylonitrile based carbon fibres were treated in a defined process to reproducibly generate aerosols. For this purpose, the CF were cut by hand, thermally treated in nitrogen or air and comminuted in a planetary ball mill. This bulk material was dispersed into dry air by a segmented belt aerosol generator. The resulting CF aerosol passed a PM_{10} inlet when introducing to an exposure station. Inside the exposure station, the inhalable fraction of the CF material was delivered to the air-liquid interface (ALI) of human lung cells, where toxicological investigations were carried out, i.e., directly on the apical surface of cell cultures, in order to simulate lung-like conditions. Lung epithelial, macrophage and fibroblast cell cultures in mono- and co-culture were used for toxicological evaluation of respirable CF fragments focussing on determination of cytotoxicity, gene expression analyses and determination of pro-inflammatory, profibrotic and genotoxic potential (Friesen et al., 2023).

The aerosol inside the exposure system was sampled on filters to determine the exposure dose. For assessing the cell surface dose on the one hand the online dose measurement employing a quartz crystal microbalance was used, on the other hand empty cell culture inserts were exposed. Both samples, the membranes from the inserts as well as the filters from the aerosol phase were analysed by digital microscopy.

The images of the fibre fragments were analysed regarding length and thickness using two methods, the Feret diameters on one hand and the rectangle model on the other hand. These values derived from the images were used to calculate the aerodynamic equivalent diameter and to sort the objects in size classes resulting in histograms for the three fractions fibres fulfilling the WHO criteria, fibres of other geometries and particles. The deposition efficiency was determined by calculating the ratio of the deposited dose to the exposure dose class by class. The deposition behaviour of the three fractions of the carbon fibre aerosol was measured on the one hand and simulated by numerical methods on the other.

For the numerical simulation of fibre deposition, the shape factor X was implemented into the calculation of the drag force. Simulations were performed for fibre diameters ranging from some nanometres to a few microns with aspect ratios between 1 and 20. Model validation is conducted through comparison with experimental data.

Carbon fibres in the aerodynamic equivalent diameter theoretically achieve deposition efficiencies in the range of around 1 % (e.g., $\omega_0(d_{ae} = 1.08\ \mu m) = 0.91\ \%$) to 80 % (e.g., $\omega_0(d_{ae} = 10.8\ \mu m) = 82.4\ \%$). When using an electrostatic field, the deposition efficiencies can be increased up to $\omega_0 = 100\ \%$, depending on the size and particle charge.
In comparison, the measured deposition efficiencies show lower values and will be discussed regarding influences of sampling and image analyses.

Parts of this work were financed by the Federal Ministry of Education and Research under project number FK03XP0195 and by the project FINEST funded by the Investment and Networking Fund of the Helmholtz Association under grant agreement no. KA2-HSC-10 which is gratefully acknowledged.

Friesen, A., et al. (2023): *Int. J. Mol. Sci.* 24 (3), S. 1927. DOI: 10.3390/ijms24031927.

Resolving Particle Size Distributions into Biomass-Burning and Fossil-Fuel Sources in Subarctic Alaska Using Integrated Observations and Machine Learning

L. A. Zanandreis[a], R. Betha[a] and S. Kanagaratnam[a]

[a] Department of Civil, Environmental, and Construction Engineering, Texas Tech University, Box 41023, Lubbock, TX 79409-1023.

Keywords: Particle Size Distribution, Winter Air Quality, Absorption Ångström Exponent, Biomass-Burning, Machine Learning.

Conference topic: Fundamentals of APT.
Presenting author email: lzanandr@ttu.edu

Wintertime air quality in Interior Alaska is severely degraded by residential heating emissions and persistent meteorological inversions, as shown in Figure 1 (Simpson et al., 2024; Pohorsky et al., 2025). Quantifying the relative influence of biomass-burning and fossil-fuel combustion remains challenging because aerosol microphysics, mixing state, and meteorology are tightly coupled under stagnant winter conditions (Schmale et al., 2018; Ijaz et al., 2025). In this study, we present four consecutive winter campaigns in North Pole, Alaska, featuring high-resolution aerosol particle size distributions (PSD) measured using a Scanning Electrical Mobility Spectrometer (SEMS), collocated with an Aethalometer and a Total Carbon Analyzer.

The Absorption Ångström Exponent (AAE) is used as an optical proxy to distinguish fossil-fuel–leaning conditions with AAE less than 1.6 from biomass-burning–leaning conditions with AAE greater than 1.6, allowing evaluation of how PSD structure and size–optics relationships evolve across winters (Sandradewi et al., 2008; Zotter et al., 2017). Across all campaigns, particle populations exhibit a robust U-shaped diurnal pattern in geometric mean diameter (Dg), with larger growth- and aging-dominated particles at night and smaller modes near midday, consistent with daytime boundary-layer deepening and dilution observed during winter pollution episodes in the Fairbanks North Star Borough (Robinson et al., 2023; Pohorsky et al., 2025). Combined analyses show that Dg decreases with increasing number-to-volume ratio (N/V), while AAE increases with Dg, linking particle growth toward larger diameters with enhanced short-wavelength absorption during biomass-burning–influenced periods (Sandradewi et al., 2008; Ijaz et al., 2025).

To operationalize source-regime detection, we trained an XGBoost classifier using PSD bins, meteorological variables, and temporal features to predict binary AAE regimes (Ma et al., 2020). The model achieved strong performance (ROC AUC ≈ 0.89–0.90; PR AUC ≈ 0.96) and improved balanced accuracy through threshold optimization (up to ≈ 0.83), enabling scalable probabilistic labeling of winter pollution episodes for exposure assessment and mitigation planning. Overall, these results demonstrate how integrated size-resolved and optical measurements can constrain dominant wintertime aerosol regimes in subarctic environments.

Figure 1. Image of high concentrations of local emissions trapped below a low altitude inversion layer (North Pole, Alaska).

This work was supported by by the National Science Foundation (NSF) under Award Numbers 2127431 and 2127430.

Ma, J., et al. (2020) Aerosol and Air Quality Research. 20, 1854 to 1869.

Ijaz, A., et al. (2025) Atmospheric Chemistry and Physics. 25, 11789 to 11811.

Pohorsky, R., et al. (2025) Atmospheric Chemistry and Physics. 25, 3687 to 3716.

Robinson, E. S., et al. (2023) Environmental Science: Atmospheres. 3, 568 to 580.

Sandradewi, J., et al. (2008) Environmental Science and Technology. 42, 3316 to 3323.

Simpson, W. R., et al. (2024) Environmental Science and Technology Air. 1, 200 to 222.

Zotter, P., et al. (2017) Atmospheric Chemistry and Physics. 17, 4229 to 4249.

Bridging Measurement and Theory with a General Aerosol Microphysical Model

Fraser Crawford[1], Jonathan P. Reid[2] and Walther Schwarzacher[3]

[1]School of Physics, University of Bristol, Bristol, BS8 1TS, UK
[2]School of Chemistry, University of Bristol, Bristol, BS8 1TS, UK
[3]Syed Babar Ali School of Science and Engineering, LUMS, Lahore, Pakistan
Keywords: Modelling, Locking, Microphysics, Electrodynamic Balance

Presenting author email: fraser.crawford.2019@bristol.ac.uk

Aerosols serve as unique environments for chemical and engineering applications owing to their small volume and comparatively large surface area. Understanding evolving aerosol particles proves to be difficult due to the combination of advection, diffusion, concentration and adsorption processes that are quickly progressing during evaporation and growth. A large number of industrial applications using aerosol technology, such as spray drying, rely on these combined effects, with many studies dedicated to understanding the sensitivity of the system to each's physical variables. Microphysical models serve as a useful intermediary between the complex observed behaviour and the individual theoretical processes taking place.

In this work, a general microphysical model framework is presented. This model accounts for the diffusion of temperature and material within the droplet using a finite volume approach based on Mignot *et al* (2024). Model predictions of the droplet surface state informs evaporation and likewise physical properties such as viscosity can be found as a function of position within the droplet. The model is designed such that additional processes can be coupled easily into the droplet's evolution, such as additional transport mechanisms. The model is utilised for exploring how insoluble nanoparticles gather at a droplet's surface during evaporation and how they combine together to form a rigid shell. This process is known as nanoparticle locking.

To provide a real basis for model parameters, a previously reported dataset of locking point radii and times of silica nanoparticle suspensions from Archer *et al* (2020) and new polymer nanoparticle suspension measurements were used. These measurements were conducted within an electrodynamic balance where the droplet radius over time was measured using laser light scattered by the droplet. The locking time was taken as the time where the standard deviation of the measured radius over many droplets suddenly increased.

It is found that Fickian diffusion alone is not able to describe the transport of nanoparticles in rapidly evaporating water droplets. This leads to the implementation of a novel particle displacement scheme where dense packings of particles at the droplet surface may push one-another deeper into the droplet, enhancing mixing. Measurements also suggest that droplets in higher air flow speed environments lock at a smaller radius, counter to expectation from examining the Péclet numbers, implying additional mixing is taking place. A parametrisation based on Hill's spherical vortex is used to model this enhanced transport (Sirignano, 1999), seeing good agreement between simulation results and the measurement.

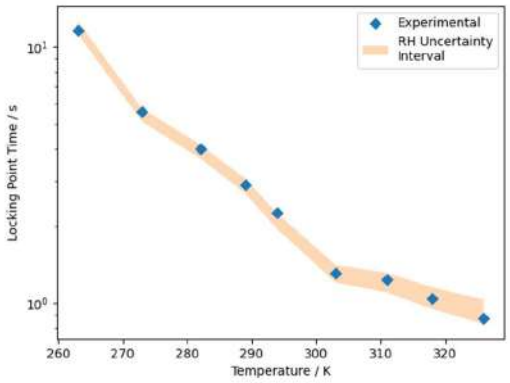

Figure 1. Locking point time vs. Temperature for initially ~30 µm radius droplets of 0.6% v/v colloidal silica in water, exposed to dry air. Measured locking times are given by the blue diamonds from Archer *et al* (2020) and the model output over the measurement's relative humidity uncertainty in orange.

This work is supported by the Engineering and Physical Sciences Research Council Centre for Doctoral Training in Aerosol Science, grant code EP/S023593/1.

Mignot, B., Mahmud, T., Heggs, P. J., & Ghadiri, M. (2024) *Aerosol Science and Technology* ***58*****(8)**, 942–956.

Archer J., Walker J.S., Gregson F.K.A., Hardy D.A., and Reid J.P. (2020) *Langmuir* **36 (42)**, 12481-12493.

Sirignano W.A. (1999) *Fluid dynamics and transport of droplets and sprays*, Cambridge University Press.

CarbonX: A Process Design Tool for the Gas-Phase Synthesis of Metal Nanoparticles and Carbon Nanotubes

H. Rahbar[1] and M. R. Kholghy[2]

[1] Energy and Particle Technology Laboratory, Department of Mechanical and Aerospace Engineering, Carleton University, K1S 5B6, Canada

Keywords: carbon nanotube, gas-phase synthesis, numerical solver, machine learning.

Presenting author email: HosseinRahbar@cmail.carleton.ca

Carbon nanotubes (CNTs) exhibit exceptional electrical, optical, and mechanical properties that make them promising candidates for applications in energy storage, sensing, and advanced composites, Conley and Karttunen (2022). Chemical vapor deposition (CVD) synthesis offers advantages in terms of scalability, cost-effectiveness, and control over nanotube characteristics compared with earlier methods, Manawi *et al* (2018). However, controlling CNT morphology and yield in floating-catalyst CVD (FCCVD) reactors remains challenging due to the complex interplay between chemical kinetics, catalyst nanoparticle evolution, and carbon deposition mechanisms, Xu and Ding (2021).

This study presents CarbonX, an object-oriented Python package designed to model one-dimensional CVD reactors for predicting the gas-phase synthesis of metallic (Fe, Ni, Co) nanoparticles (NPs) and their role in single- and multi-walled CNT formation. The framework integrates four fully coupled submodules: detailed chemical kinetics (using up to 971 species and 1948 reactions), surface kinetics models accounting for catalyst activation, deactivation, and hydrogenation, population balance models (both monodisperse and sectional) for tracking the evolution of morphology of NPs during inception, coagulation, and sintering, and CNT dynamics modules for predicting CNT length, diameter, and wall number.

Two surface kinetics models, multilayered and dual-dissociation, are adapted from the literature on substrate-based CVD and extended to FCCVD conditions. The package performance is validated against experimental measurements of NP size distributions, CNT growth kinetics, and terminal lengths from multiple CVD reactor configurations. Parametric maps are generated to identify optimal process conditions (temperature, feedstock concentration, residence time) for producing single- and multi-walled CNTs, with decision boundaries determined using an integrated machine learning classification submodule. CarbonX predictions show agreement within 22% for CNT mobility diameters and 30% for NP primary particle sizes compared to differential mobility analyzer and transmission electron microscopy measurements.

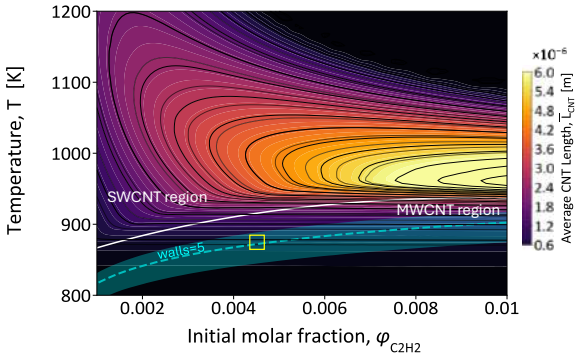

Figure 1. Maps of CNT length (L_{cnt}) as a function of the initial C_2H_2 molar fraction and reactor temperature, evaluated at the reactor outlet ($L_{reactor}$=0.6 m). The map has generated from 1024 simulations performed by CarbonX in this study. The white isopleth indicates the decision boundary calculated from machine learning classification submodule in the package that separates the regions of single- and multi-walled CNT zones. The package performance is benchmarked by predicting the number of walls of MWCNTs produced in the reactor proposed by Kim and Zachariah (2005) at T=873 K and $\varphi_{C_2H_2}$=0.0045 (□), where the predicted wall number (i.e., 4 ≤ walls ≤ 12, with an average of 5) is in good agreement with HRTEM measurements (i.e., walls < 15). The shaded region represents the range of process conditions required for the synthesis of MWCNTs within the calculated wall number range.

The research leading to these results has received funding from the Canada Research Chairs Program (Grant # CRC-2019- 232527), the Natural Sciences and Engineering Research Council of Canada (Discovery Grant #RGPIN-2019-06330 and Early Career Supplemental Award #DGECR-2019-00220), and MITACS.

Conley, K., Karttunen, A. J. (2022) *The Journal of Physical Chemistry C*. **126**, 17266-17274.

Kim, S. H., Zachariah, M. R. (2005) *Nanotechnology*. **16**, 2149.

Manawi, Y. M., Ihsanullah, Samara, A., Al-Ansari, T., Atieh, M. A. (2018) *Materials*. **11**, 822.

Xu, Z., Ding, F. (2021) *Carbon*. **175**, 69-76.

First steps towards the development of a digital twin for flame spray pyrolysis systems

B. Franzelli, I. Choudhury, J. Yi, J. Bonnety, S. Iavarone
Laboratoire EM2C, CNRS, CentraleSupélec, Université Paris-Saclay, 91960 Gif-sur-Yvette, France
Keywords: real-time monitoring, low-order models, optical diagnostics, CFD simulations, TiO_2 optical properties.
Presenting author email: benedetta.franzelli@cnrs.fr

Flame spray pyrolysis (FSP) is a promising technology to produce high-value unique nanoparticles (NP) at a large scale (Li H. et al. 2026). Despite its high potential, FSP technology is still not extensively deployed at an industrial level. Typically, the desired nanoparticle characteristics are obtained through empirical adjustments of the operating conditions. This ''trial and error" strategy is tedious, time-consuming, and inefficient, especially given the variability in applications and, consequently, in the targeted NP characteristics. Additionally, this approach often neglects the quantification of pollutant emissions from combustion such as CO2, CO and NOx. Finally, most of the results are today established at a laboratory-scale level. In this context, a robust physics-based optimization strategy is essential for tailoring NP while minimizing emissions and scaling-up FSP systems at the industrial scale. A digital twin is a multi-physics, multi-scale simulation that mirrors in real-time its physical twin using low-order models, sensors and input data (Aversano et al. 2021). The development of a physics-based digital twin for FSP systems will largely support their optimization and, consequently, their use at the industrial level.

In this work, we will present the first milestones achieved at laboratory EM2C towards the creation of a digital twin for FSP. For this, we will consider a fundamental configuration allowing: 1) the improvement of our fundamental understanding of the in-flame aerosol process; 2) the development of tools on a well-controlled configuration, facilitating a quantitative evaluation of their accuracy. In specific, we will consider a laminar coflow diffusion H_2/Ar/TTIP flame already experimentally and numerically studied to produce TiO_2 NP [Yi 2023, Franzelli 2024]. As a first goal, we aim to monitor the in-flame optical properties, specifically the spectral evolution $\varepsilon_{\lambda=}$ $E(m_\lambda)$/ $E(m_{450})$ of the absorption function $E(m_\lambda)$, which may contain information on the particle size, morphology, crystallinity structure, surface defects, and so on.

To obtain a real-time monitoring of TiO_2 optical properties, we will consider images obtained using a digital camera, whose implementation and use is extremely easy (Choudhury et al. submitted). From these images, the three Red-Green-Blue (RGB) channels will be extracted to measure the flame luminosity at three emission wavelengths. To obtain ε_λ from pyrometry theory, the 2-D field of the gas temperature T is required. A satisfactory T estimation can be obtained from CFD simulations. However, the associated simulation time is of the order of a day, preventing its use for monitoring in real-time. To overcome this issue, we will construct a low-order model based on machine-learning methods trained on a high-fidelity CFD database (Aversano et al. 2021). The CPU time of the low-order model will be of the order of seconds up to minutes.

Thus, by coupling information from a digital camera with a low-order physics-based model (Fig. 1), it will be possible to obtain, in quasi-real time the 2-D spatial evolution of flame temperature and finally NP optical properties. If successful, this coupling will represent the first step towards real-time monitoring and optimization of FPS systems. This coupled strategy has the potential to be extended to any NP quantity of interest, enabling to follow in real-time the effects of the operating conditions on NP flame synthesis and paving the way for automatic optimization of FSP systems.

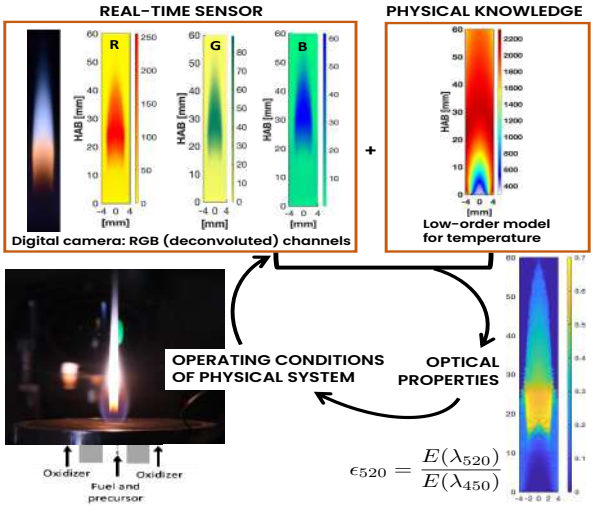

Figure 1. Representation of the optimization strategy.

This work has been supported as part of France 2030 programme (Grant agreements ANR-11-IDEX-0003, ANR-24-CE50-4913, ANR-25-ERCC-0001).

Li H., Goudeli E., Teleki A., Sotiriou G. (2026) *Prog. Energy Comb. Sci.* **113**, 101272.
Aversano G., Ferrarotti,M., Parente A. (2021) *Proc. Comb. Ins.* **32**, 5373-5381.
Franzelli B., Bonnety J., Yi J., Ogata Y., Cuoci A., Betrancourt C. (2024) *Proc.. Comb. Ins.* **40**, 105599.
Yi J. (2023) *PhD thesis at Université Paris-Saclay*.
Choudhury I., Yi J., Bonnety J., Franzelli B. submitted to *7th International Symposium on Gas-Phase synthesis.*

The VERT GPF retrofit program within the Horizon Europe AeroSolfd project: Overview and Final results

L. Rubino, A.C. Mayer, J. Czerwinski, T. Lutz, L.C. Larsen
VERT Association

Presenting author email: Lauretta.rubino@vert-dpf.eu

The Swiss-based VERT association has a long history in reducing ultrafine particle emissions via filtration and retrofitting. In the HORIZON Europe AeroSolfd project (2022-2025), aiming to advance clean urban mobility by developing affordable and sustainable retrofit solutions for tailpipe but also brakes emissions and semi-closed environment, VERT focussed on reducing tailpipe emissions from gasoline vehicles (both DI and PFI).

A state-of-the-art Gasoline Particulate Filter (GPF) technology, featuring an uncoated ceramic multicell wall-flow filter was used. VERT, in partnership with HJS, CPK, BFH, developed and tested a GPF-retrofit system at Technology Readiness Level 8 (TRL 8).

Results demonstrate over 99% filtration efficiency for particles smaller than 500 nm on standard cycles (WLTC) and realworld driving cycles (RDE).
Forty-two gasoline vehicles (GDI and PFI) were retrofitted with the GPF retrofit across
Germany, Switzerland, Israel, and Denmark over a 6 to 8-month operational period.
No issues were observed with filter regeneration, or increased fuel consumption, noise, drivability or secondary emissions.
This paper presents the GPF retrofit program, the field trial results and the NPTI investigation of over 1000 gasoline vehicles in Switzerland.

VERT strongly recommend retrofitting and NPTI for both the diesel and gasoline vehicle fleet to drastically reduce harmful nanoparticle emissions and immediately improve air quality in congested urban areas with cost-effective filtration solutions.

The impact of particle size on the light absorption of carbonaceous aerosol emissions from wood combustion

C. Moularas[1,2], I. Tsiodra[3], N. Mihalopoulos[3,4], P. Demokritou[1] and G.A. Kelesidis[1,2]
[1]Environmental and Occupation Health Science Institute, Rutgers University, Piscataway, 08854 NJ, USA
[2]Faculty of Aerospace Engineering, Delft University of Technology, Delft, 2629 HS, The Netherlands
[3]Institute for Environmental Research and Sustainable Development, National Observatory of Athens, Athens, 15236, Greece.
[4]Department of Chemistry, University of Crete, Heraklion, 71003, Greece

Keywords: brown carbon, wildfires, wood combustion, light absorption
Associated Conference Topics: Fundamentals of APT
Presenting author email: G.Kelesidis@tudelft.nl

The increasing frequency and intensity of climate change-driven wildfires has enhanced dramatically the emissions of particulate matter (PM), such as Brown Carbon (BrC), that affect millions of people even in densely-populated metropolitan areas (Laurent *et al*, 2024). At the same time, BrC particles can cool or warm the climate depending on their light absorption and change the wildfire dynamics (Wang *et al*, 2024). Thus, identifying the link between the light absorption of BrC and its physicochemical properties is essential to quantify the climate impact of wildfire PM.

Here, the light absorption of wildfire-like BrC emitted by pine and oak wood combustion is elucidated using a thermal decomposition platform coupled with a variety of real-time monitoring and time-integrated sampling instrumentation (Moularas *et al*, 2024). So, BrC particles with controlled morphology, size distribution and light absorption were generated by varying the wood mass to emulate the physicochemical properties of "real world" wildfire PM emissions. That way, it is shown that increasing the wood mass from 50 to 600 mg enhances the BrC mass absorption cross-section, *MAC*. The measured *MAC* ranges from 0.3 to 0.6 m^2/g (Fig. 1: lined bar), explaining nicely the MAC variation observed in the field between different wildfire PM events.

Most importantly, the light absorption of size-fractionated BrC particles was quantified, for the first time to the best of our knowledge. This reveals that the large $PM_{0.1\text{-}2.5}$ size fraction of BrC (Fig. 1: red bar) contains carcinogenic, high molecular weight PAHs and absorbs up to five times more light compared to the small size $PM_{0.1}$ fraction (Fig. 1: blue bar). So, increasing the fuel mass from 50 to 600 mg increases the $PM_{0.1\text{-}2.5}$ mass concentration and explains the enhancement of the overall BrC *MAC*. This is in line with previous field measurements showing that the concentration of high molecular weight PAHs exhibiting strong light absorption increases with increasing particle size (Di Lorenzo *et al*, 2018). The *MAC* of the $PM_{0.1}$ and $PM_{0.1\text{-}2.5}$ fractions of BrC measured here can be interfaced with global climate models to determine the contribution of wildfire PM to global warming (Kelesidis *et al*, 2022).

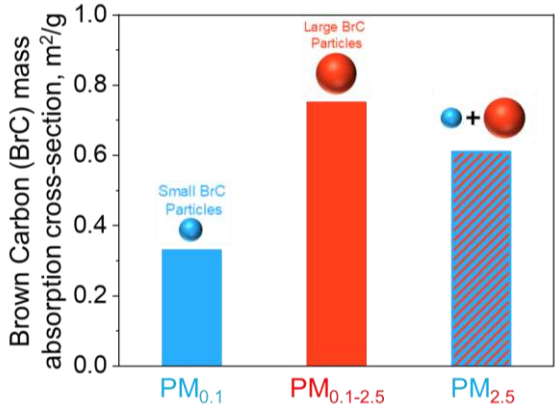

Figure 1. Mass absorption cross-section, *MAC*, of $PM_{0.1}$ (blue filled bar), $PM_{0.1\text{-}2.5}$ (red filled bar) and $PM_{2.5}$ with (lined bar) of BrC particles.

This work was funded by NIH grants num. 1R01HL168899-01A1 and 1R01HL168899, the Rutgers-NIEHS Center for Environmental Exposures and Disease (CEED) (NIH grant # P30ES005022) and, in part, by Delft University of Technology.

References

Laurent, J.G.C., Parhizkar, H., Calderon, L., Lizonova, D., Tsiodra, I., Mihalopoulos, N., Kavouras, I., Alam, M., Baalousha, M., Basiza, L., Kelesidis, G.A. and Demokritou, P. (2024) *Environ. Sci. Technol.* **58**, 14753-14763

Wang, Z., Huang, X., Xue, L., Ding, K., Lou, S., Zhu, A. and Ding, A. (2024) *Geophys Res Lett* **51**, e2024GL108444

Moularas, C., Demokritou, P. and Kelesidis, G.A. (2024) *Proc. Combust. Inst*. **40**, 105513.

Di Lorenzo, R.A., Place, B.K., VanderBoer, T.C. and Young, C.J. (2018), *ACS Earth Space Chem.* **2**, 278-285

Kelesidis, G.A., Neubauer, D., Fan, L.S., Lohmann, U. and Pratsinis, S.E. (2022) *Environ. Sci. Technol.* **56**, 8610-8618

Nucleation, Surface Growth and Coagulation of Soot by Hierarchical Modeling

A. Fakharnezhad[1], A. Ganguly[1], G. A. Kelesidis[2], S. P. Roy[3], and E. Goudeli[1]

[1]Department of Chemical Engineering, The University of Melbourne, Parkville, Melbourne VIC 3010, Australia
[2] Chemical Engineering, The University of Melbourne, Parkville, Melbourne VIC 3010, Australia
[3]Department of Mechanical Engineering, Marquette University, Milwaukee WI 53233, USA
Keywords: soot, nucleation rate, surface growth rate, reactive Molecular Dynamics, monodisperse particle dynamics.

Presenting author email: eirini.goudeli@unimelb.edu.au

Carbon black is the largest nanomaterial produced industrially today, primarily through the combustion of residual fuel oil. Carbon black nanoparticles are used in inks, tires, and paints, contributing to a $16 billion industry worldwide. In contrast, soot has long been at the forefront of research due to its adverse health effects and negative impact on the environment and Earth's albedo. So, research on combustion chemistry and a more systematic understanding of carbon-based nanoparticle formation is crucial not only for better product design but also for the development of cleaner combustion technologies. The complexity in modelling carbonaceous nanoparticle formation, remains a significant challenge. Soot nucleation and surface growth largely affect particle size distribution, and chemical composition, which are critical for determining end-product properties and meeting emission regulations.

Here, chemical nucleation and surface growth of carbonaceous nanoparticles are investigated during pyrolysis of acetylene by reactive molecular dynamics at temperatures of 1350-1800 K for various initial fuel concentrations. The mass increase of soot nanoparticles, having initial diameter of 3 – 4.5 nm, is tracked as a function of time during surface condensation of reactive hydrocarbon molecules and radicals produced by acetylene pyrolysis. This temporal evolution of the soot mass growth allows for the direct derivation of a "lumped" surface growth rate constant, based on the hydrogen-abstraction acetylene addition (HACA) reaction model (Frenklach & Wang (1991)), however, without relying on explicit information or assumptions about the soot surface reactivity.

A surface growth rate equation is derived "ab initio" by MD simulations that follows an Arrhenius dependence with process temperature:

$$\ln(k'_{MD,avg}) = 3.946 - \frac{2017.3}{T} \qquad (1)$$

This MD-derived "effective" rate constant implicitly accounts for the soot surface reactivity eliminating the need to assume or specify the number density of reactive sites and the fraction of active sites. Equation (1) is employed into a monodisperse particle dynamics model (Kholghy *et al.*, 2018) accounting for surface growth and coagulation. The MD-obtained surface growth rate constant (Figure 1: solid line) nicely predicts soot volume fraction measurements (Figure 1: symbols) in various burners, yielding improved predictions over the HACA growth rate (Figure 1: broken line).

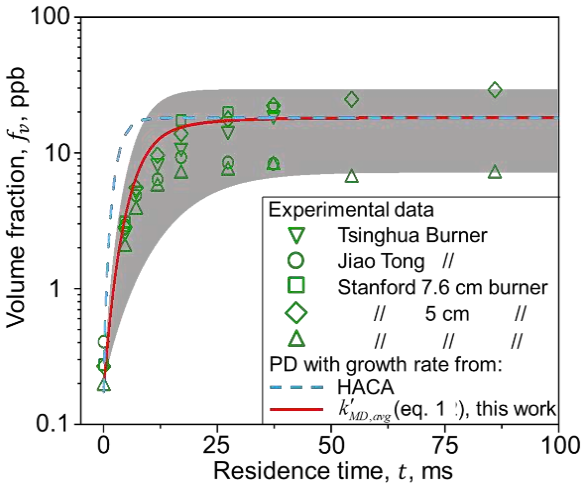

Figure 1. Soot volume fraction, f_v, as a function of residence time obtained by a monodisperse particle dynamics model using MD-obtained (eq. 1; solid line) and HACA surface growth rate (broken line). The model is compared to f_v measurements at various burners (symbols).

The proposed methodology, when combined with MD-derived nucleation rates, can greatly simplify soot modelling by lumping surface and gas-phase reactions into a single effective rate constant. This approach can be readily applied to material synthesis, enabling the determination of surface reaction rates of carbon blacks as well as a range of inorganic nanomaterials (metals, oxides, composites, etc.).

Frenklach, M., Wang, H. (1991) *Symp. Combust. Proc.*, **23**, 1559-66.
Kholghy, M.R., Kelesidis, G.A., Pratsinis, S.E. (2018) *Phys. Chem. Chem. Phys.*, **20**, 10926-10938.

Nitrogen-assisted particle fluidization for dry coating of high-dose inhalable powders: Impact on particle micrometrics

H. A. Al-Assaf[1], A. Rahman[2], R. Badhan[1], D. Kirby[1], A. R. Mohammed[1]
[1]Aston Pharmacy School, Aston University, Birmingham B4 7ET, UK
[2]Dentistry, School of Health Sciences, University of Birmingham, Birmingham B5 7EG, UK
Keywords: high-dose inhalable powders; dry particle coating; particles micrometrics
Presenting author email: 210266519@aston.ac.uk

High-dose inhalable powders present persistent formulation challenges due to increased particle aggregation, poor flowability, and reduced dispersibility, which ultimately compromise aerosol performance (Sibum et al., 2018). Conventional blending approaches often provide limited control over particle surface properties in high drug-content inhalable formulations. Building on recent advances in high-dose powder manufacturing (Al-Assaf et al., 2023), this study investigated isothermal dry particle coating (iDPC) – a low-shear process employing nitrogen-assisted particle fluidization – to modulate particle micrometrics relevant to pulmonary delivery, with a focus on changes in surface area, surface accessibility, and particle layering.

Fluticasone propionate (FP) and lactose (Respitose® SV001) were used to prepare high-dose formulations (50% w/w FP) using iDPC at 1500 rpm for 10 min and nitrogen flow rates of 0 $L \cdot min^{-1}$ (F1) and 20 $L \cdot min^{-1}$ (F2). Particle morphology was analyzed by SEM (JEOL JSM-IT200, 5 kV), surface characteristics by BET (Micromeritics TriStar II Plus), and particle size distribution by laser diffraction (Sympatec HELOS).

The iDPC process resulted in a high powder yield (F1: 98.63%; F2: 98.73%) confirming negligible material loss during powder processing. Marked differences in surface and particle micrometric properties were observed between unprocessed materials and dry-coated formulations prepared with and without nitrogen airflow. FP exhibited high surface area (SA) (10.82 m^2/g), indicative of a highly energetic API surface, whereas lactose had a surface area of 0.23 m^2/g, consistent with a smooth, low-energy carrier. Airflow-assisted processing (F2) produced an 8.76% increase in surface area and 7.41% larger pore diameter relative to F1, indicating surface alteration and the formation of porous structures due to adsorption of fine FP particles (Table 1). SEM micrographs corroborated these trends, confirming fewer discrete FP particles and denser, more continuous FP coverage with compact multilayer stacking for F2, consistent with nitrogen-driven multilayer deposition, whereas F1 exhibited patchier and less uniform coating (Figure 1). Particle size distribution analysis showed a clear shift in coated formulations relative to lactose (D90 = 218.90 µm), with higher D90 values observed for F1 (302.48 µm) and F2 (297.92 µm), confirming FP deposition onto the carrier surface. The slightly lower D90 for F2 compared to F1 indicates more compact and stacked multilayer FP assemblies under nitrogen-assisted fluidization rather than randomly distributed coating.

Table 1. Surface and particle micrometric properties of F1, F2 dry-coated formulations prepared using iDPC.

Particles properties	F1	F2
SA (m^2/g)	3.88	4.22
BET Constant	127.73	103.05
% Yield	70.96	75.73
Pore size (Å)	45.08	48.42

Similarly, the higher BET constant observed for F1 (127.73) compared to F2 (103.05) indicated a more heterogeneous surface resulting from irregular FP attachment, whereas the reduced BET constant for F2 suggests a more uniform surface energy distribution. Such homogenization of surface energetic sites has been associated with improved particle rearrangement and coating uniformity in dry powder systems.

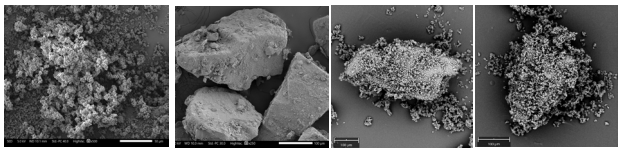

Figure 1. SEM images of FP, Lactose, F1 and F2 formulations from left to right.

These findings show that the process of dry coating using iDPC (20L/min of N_2) induces particle fluidization, promoting rearrangement of the powder bed. In contrast, dry coating in the absence of airflow relies primarily on mechanically driven particle movement, which can result in uneven FP distribution and heterogeneous surface coverage. The integration of nitrogen-assisted fluidization therefore represents a key mechanistic advantage of iDPC in achieving controlled multilayer deposition for high-dose inhalable powders.

Al-Assaf, H. A., Papadimitriou, S. A., Rahman, A., Badhan, R., & Mohammed, A. R. (2025). Advanced Manufacturing Methods for High-Dose Inhalable Powders. Pharmaceutics, 17(3), 359. https://doi.org/10.3390/pharmaceutics17030359

Sibum, I., Hagedoorn, P., de Boer, A. H., Frijlink, H. W., & Grasmeijer, F. (2018). Challenges for pulmonary delivery of high powder doses. *International journal of pharmaceutics*, *548*(1), 325–336. https://doi.org/10.1016/j.ijpharm.2018.07.008

Novel High-Efficiency Cyclone Collector Using a 15 mL Falcon Tube for Bioaerosol Collection and Molecular Detection

R.Baxter[1], D.McCluskey[1], I.Munro[1], R.Kaye[1], and I.Johnston[1]
[1]Biodetection Hub, University of Hertfordshire, Hatfield, AL109AB, UK
Keywords: Bioaerosol sampling, High-efficiency cyclone, Molecular detection, Aerosol chamber testing.

Presenting author email: r.baxter3@herts.ac.uk

Airborne biological particles are a critical vector for plant diseases and environmental pathogens, driving demand for compact samplers that can concentrate trace bioaerosols for rapid molecular detection. This work presents the design and experimental characterisation of a miniature high-efficiency cyclone derived from the Stairmand geometry and integrated into a standard 15 mL Falcon tube as a sealed, disposable collection vessel. The cyclone proportions were scaled and modified (extended body, 22 mm cone, involute inlet) to preserve Stairmand-type flow while increasing residence time and collection capacity at a manageable pressure drop. Theoretical performance was assessed using classical cyclone models (including Möthes–Löffler and Leith–Licht) to estimate grade efficiency and cut-off diameter, with particular attention to miniature-scale effects and the potential for a 'fish-hook' ,W.Kraipech et al (2002), in the efficiency curve. Experimental testing was performed in an 8 m^3 aerosol chamber using polystyrene microspheres and *Bacillus globigii* (BG) as a biological simulant over flow rates from 38 to 100 $L \cdot min^{-1}$. Collection efficiency and d_{50} were determined by flow cytometry and biological assays, with 1 µm PSL collection ranging from 9–18% and optimal performance near 80 $L \cdot min^{-1}$ for 5 µm particles. BG spores collected by the cyclone were consistently detectable by loop-mediated isothermal amplification (LAMP), lateral flow immunoassay, and culture, confirming preservation of biological integrity and compatibility with integrated molecular workflows. The results demonstrate that a miniaturised, Falcon-tube-based Stairmand cyclone can provide robust, reusable geometry for portable bioaerosol surveillance platforms in both agricultural and defence applications and define a baseline for further CFD-guided optimisation of fine-particle capture and pressure drop.

A basic description of the methodology is as follows: - polystyrene microspheres that are nebulised into a 2x2x2 meter ($8m^3$) aerosol chamber. The aerosol chamber provides a reservoir of particles that can be pulled through a cyclone where they are separated and deposited into centrifuge tube. The particles are then mixed with DI water and run through a flow cytometry machine to determine the number of particles present. The flow rate through the cyclone is recorded, and the particle concentration is logged for the duration of the test. Collection performance can then be calculated from this data.

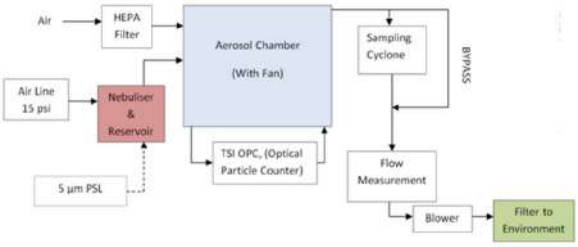

Figure 1: Aerosol chamber setup for 3 stages - Aerosolising particles (PSL), Cyclone collection/Separation, and Flow measurement

The performance of the modified Stairmand cyclone was evaluated across flow rates ranging from 38 to 100 $L \cdot min^{-1}$ using both polystyrene microspheres and biological aerosols (Bacillus globigii, BG) . Figure 2 summarises the mean collection efficiency obtained for the various particle size fractions.

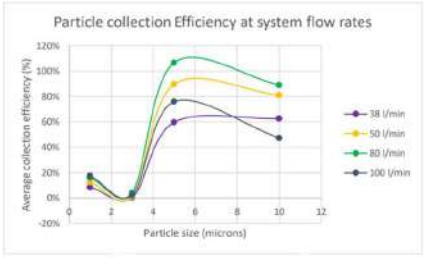

Figure 2 Particle collection efficiency at system flow rates

The 'fish-hook',W.Kraipech et al (2002), cyclone effect observed at smaller particle sizes is shown in Figure 2, where the collection efficiency curves display a characteristic dip around 3 µm, consistent with cyclone performance data in the literature.

Kraipech, W., Chen, W., Parma, F.J., & Dyakowski, T. (2002). Modelling the fish-hook effect of the flow within hydrocyclones. International Journal of Mineral Processing, 66(1–4), 49–65. https://doi.org/10.1016/S0301-7516(02)00012-1

This work was supported by DASA under DASA Contract #: ACC2016891.

Highly porous carbon blacks for supercapacitors and electrochemical energy storage

G.A. Kelesidis[1], N. Rossi[2], A.G. Senol[3], C. Prehal[3,4], and S.E. Pratsinis[2]

[1]Faculty of Aerospace Engineering, Delft University of Technology, Kluyverweg 1, 2629 HS Delft, the Netherlands
[2]Particle Technology Laboratory, Institute of Process Engineering, Department of Mechanical and Process Engineering, ETH Zürich, Zürich, 8092, Switzerland
[3]Material and Device Engineering Group, Department of Information Technology and Electrical Engineering, ETH Zürich, Zürich, 8092, Switzerland
[4]Department of Chemistry and Physics of Materials, University of Salzburg, Salzburg, 5020, Austria

Keywords: carbon black, oxidation, porosity, supercapacitors.
Presenting author email: g.kelesidis@tudelft.nl

Supercapacitors are essential for efficient energy storage in power electronics, as well as to complement Li-ion batteries for short-time energy delivery and harvesting in hybrid/electric vehicles and other transportation systems (Simon and Gogotsi, 2020). These devices rely on porous carbonaceous materials, such as activated carbons that have specific surface area, *SSA* > 1800 m^2/g and exhibit large specific capacitance, C_g (≥ 180 F/g) at small (< 1 A/g) current densities (Li *et al*, 2019). However, the C_g of such supercapacitors decreases up to 40 % at increasing current densities due to the presence of small pores (< 1 nm) in the bulk activated carbon that limit the access of electrolyte ions to the internal particle surface area (Fuertes *et al*, 2004). In this regard, carbonaceous nanomaterials with large pores can be designed by carbon black (CB) oxidation (Kelesidis *et al*, 2022).

Here, highly porous carbonaceous nanoparticles are produced by oxidation of a commercial CB grade (Kelesidis *et al*, 2026). Microscopy and X-Ray diffraction analysis revealed that CB nanoparticles become more disordered during oxidation at these conditions. This enables O_2 to diffuse and react internally with the bulk CB, forming 2 - 8 nm pores that increase the CB *SSA* up to a factor of ten (Fig. 1), consistent with lattice Monte Carlo modelling of amorphous CB oxidation (Kelesidis *et al*, 2024). The CB *SSA* = 2185 ± 200 m^2/g obtained at 75 % conversion is 50 to 100 % larger than the *SSA* of most porous CB grades that are currently available in the market and on par with that of commercial activated carbons (e.g. YP80) used in supercapacitors (Li *et al*, 2019).

Supercapacitors were assembled with the oxidized CB produced here. Their measured C_g is on par with those obtained using YP80 and Ketjenblack at a current density of 0.2 A/g. Most impressively, at large current densities, the measured C_g of the oxidized CB produced here is 40 % larger than those obtained using commercial YP80 or Ketjenblack. The superior performance of the present CB is attributed to the large concentration of fine pores formed largely by internal oxidation (Kelesidis *et al*, 2022 & 2024). So, close control of the internal oxidation dynamics of CB is essential to design highly porous carbonaceous nanomaterials and optimize their performance for electrochemical energy storage.

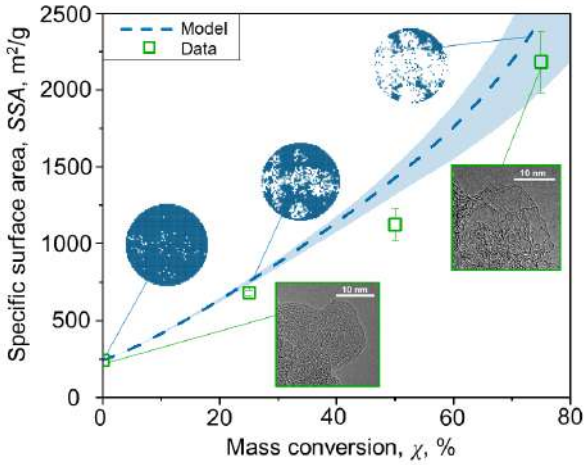

Figure 1. Evolution of CB *SSA* as a function of its conversion, χ, measured (symbols) or simulated (line & shaded area) by lattice Monte Carlo for internal and external oxidation of commercial CB (Kelesidis *et al*, 2024).

This research was funded by the Particle Technology Laboratory, ETH Zurich and Swiss National Science Foundation (grant # 182668, 163243 and 170729).

Fuertes, A.B., Pico, F. and Rojo, J.M. (2004) *J. Power Sources* **133**, 329-336.
Kelesidis, G.A., Rossi, N. and Pratsinis, S.E. (2022) *Carbon* **197**, 334-340.
Kelesidis, G.A., Crepaldi, P. and Pratsinis, S.E. (2024) *Carbon* **219**, 118764.
Kelesidis, G.A., Rossi, N., Gungor, A.S., Prehal, C. and Pratsinis, S.E. (2026) *Powder Technol.* **467**, 121557.
Li, P., Li, H., Han, D.L., Shang, T.X., Deng, Y.Q., Tao, Y., Lv, W. and Yang, Q.H. (2019) *Adv. Sci.* **6**, 1802355.
Simon, P. and Gogotsi, Y. (2020) *Nat. Mater.* **19**, 1151-1163.

Large-scale silicon nanowire paper fabrication via aerosol-catalysed CVD.

I. Gómez-Palos[1], R. S. Schäufele[1] and J.J. Vilatela[1,2]

[1]Floatech S.L., Madrid, 28906, Spain
[2]IMDEA Materials, Madrid, 28049, Spain,
Keywords: catalyst, silicon, energy, battery, Scale-up, nanowires.

Presenting author email: Isabel.gomez@floatech.eu

This work presents an aerosol-based process for the continuous fabrication of a paper-like, freestanding material composed entirely of silicon nanowires (SiNWs) and its application as anodes for next generation Li-ion batteries.

The nanowires are synthesised using a floating catalyst chemical vapour deposition (FCCVD) process, in which an aerosol of catalyst nanoparticles is mixed with a silicon precursor gas (silane) inside a tubular reactor. In the absence of a substrate, nanowire growth occurs continuously and entirely in the gas phase via the vapour–liquid–solid (VLS) mechanism (Gomez-Palos, 2023).

The process operates at atmospheric pressure and, combined with fast reaction kinetics, enables high production rates and the formation of high–aspect ratio SiNWs (length/diameter ≈ 100) (Schäufele, 2020). During gas-phase transport, the nanowires undergo aggregation and self-assembly, transitioning from a dispersed aerosol into macroscopic aggregates that can be continuously collected at the reactor outlet. As a macroscopic material, the nanowire network is similar to office paper: flexible in bending, strong in tension, and porous.

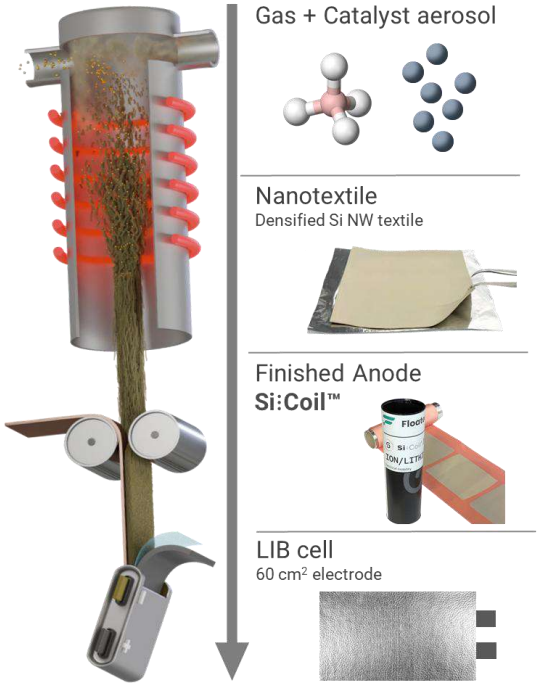

Figure 1.. From gas to batteries. Floating catalyst-based process for SiNW anodes fabrication.

The resulting SiNW nanotextile can be directly transferred onto a current collector, forming a ready-to-use anode for next-generation lithium-ion batteries. The gas-phase assembled architecture minimizes interparticle junction resistance and accommodates the large volume changes during cycling, resulting in high areal capacities and long-term electrochemical stability with both liquid (Pendashteh, 2024) and sulphide-based solid electrolytes (Sánchez-Ahijón, 2024)

Overall, the process provides a scalable route to high-performance silicon anodes and highlights the broader potential of aerosol-based manufacturing for functional energy materials. Si anodes can enable EV range near 1000km and charge times below 15 minutes, while reducing pressure of natural graphite, a critical raw material, on a scale of 100s of kilo tonnes per annum (ktpa). In the processes, this would prevent CO_2 emissions on mega tonne scale during battery manufacture, according to estimates for embodied emissions.

References

Gómez-Palos, I., Vazquez-Pufleau, M., Schäufele, R. S., Mikhalchan, A., Pendashteh, A., Ridruejo, Á., Vilatela, J. J. (2023). *Nanoscale*, *15*(13), 6052–6074.

Schäufele, R. S., Vazquez-Pufleau, M., Vilatela, J. J. (2020). Materials Horizons, 7(11), 2978–2984.

Pendashteh, A., Tomey, R., Vilatela, J. J. (2024). *Advanced Energy Materials*, *14*(16).

Sánchez-Ahijón, E., Pendashteh, A., & Vilatela, J. J. (2024). *Batteries & Supercaps*, *7*(12).

Measuring Urban Aerosol Volatility Fractions with a Catalytic Stripper at an ACTRIS Aerosol Observatory: Characterization and Implementation

M. Dollner[1], P.S. Bauer[1], V. Berger[1], B. Weinzierl[2], A. Kupc[2], A. Gattringer[2], H. J. Schulz[1], A. Boies[1,3], J. Swanson[1,4]

[1]Catalytic Instruments GmbH & Co.KG, Rosenheim, 83026, Germany
[2]University of Vienna, Faculty of Physics, Aerosol Physics and Environmental Physics, Vienna, 1090, Austria
[3]Stanford University, Department of Engineering, Stanford, CA 94305, United States
[4]Minnesota State University, Mankato, MN 56001, United States
Keywords: aerosol volatility fraction, catalytic stripper, urban air quality

Presenting author email: maximilian.dollner@catalytic-instruments.com

Aerosol particles play a central role in atmospheric processes, influencing air quality, human health, and climate. To fully understand these impacts, it is essential to quantify not only the physical properties such as concentration or size but also their chemical composition. Offline chemical analysis of aerosol samples or online mass spectrometry are generally complicated or expensive. Another efficient method is to determine the partitioning between the volatile and non-volatile fractions. This information provides insight into the chemical composition of an air mass and allows to infer information about aerosol sources, chemical aging, and transformation processes in the atmosphere (e.g. Weinzierl et al. (2006); Wehner et al. (2005, 2009); Ehn et al. (2007)).

A catalytic stripper (CS) is commonly used to separate the volatile and semi-volatile fraction from the solid aerosol particles, which allows for precise measurement of the non-volatile fraction and the total aerosol load (Swanson and Kittelson, 2010). Compared to a thermal denuder, it has the advantage that volatile substances undergo catalytic transformation and cannot recondense into particles after treatment. The CS has successfully been used in many automotive applications such as Particle Measurement Program (PMP) compliant studies (Giechaskiel et al., 2020; Swanson and Kittelson, 2010). However, not many atmospheric aerosol studies apply this simple distinction between volatile and solid particles, which plays an important factor for the investigation of air quality, human health and climate impact of aerosols.

Here we present the application of a CS for measurements of non-volatile aerosol particles at the Aerosol Observatory of the University of Vienna which is on track to become a National Facility for aerosol in-situ observations within the pan-European Aerosol, Clouds, and Trace Gas Research Infrastructure ACTRIS. This study includes the characterization of the CS with respect to particle penetration (see Figure 1) and removal efficiency of volatile and semi-volatile components. For particle penetration silver particles were generated with the Silver Particle Generator (SPG) and treated by the Sintering Stage S8000 to obtain thermally stable silver spheres in the size range between 2nm and 100nm. The characterization of the removal efficiency of volatile and semi-volatile particles is done with tetracontane, which is a well-established method in many regulations for the testing of volatile particle removal (VPR) systems in the automotive section (e.g. Euro-7).

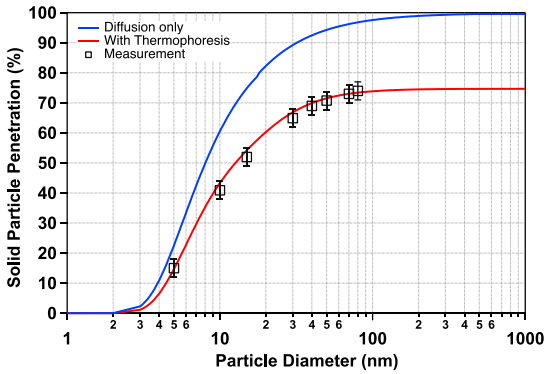

Figure 1. Measurements of solid particle penetration efficiency of a Catalytic Stripper (black squares) with calculated diffusional only (blue line) and combined thermophoretic and diffusional effects (red line).

The aim of this study is to present initial results from continuous measurements of the non-volatile aerosol fraction over several weeks at the Aerosol Observatory in Vienna, demonstrating their potential for source identification and chemical characterization, and highlighting the importance of non-volatile particle measurements.

Weinzierl, B., Petzold, A., Esselborn, M., Wirth, M., Rasp, K., Kandler, K., Schütz, L., Koepke, P. and Fiebig, M. (2009). Tellus B: Chemical and Physical Meteorology, 61(1), 96–117.

Wehner, B., T. Petäjä, M. Boy, C. Engler, W. Birmili, T. Tuch, A. Wiedensohler, and M. Kulmala (2005), *Geophys. Res. Lett.*, 32, L17810.

Ehn, M., Petäjä, T., Birmili, W., Junninen, H., Aalto, P., and Kulmala, M. (2007), *Atmos. Chem. Phys.*, 7.

Wehner, B., Berghof, M., Cheng, Y. F., Achtert, P., Birmili, W., Nowak, A., Wiedensohler, A., Garland, R. M., Pöschl, U., Hu, M. and Zhu T. (2009), J. *Geophys. Res.*, 114

Swanson, J. and Kittelson, D. (2010). *J. Aerosol Sci.* 41 (12):1113.

Giechaskiel, B., Melas, A.D., Lähde, T., and Martini, G. (2020). *Vehicles* 2 (2):342.

Microwell Aerosol-to-Vapor Conversion for Rapid Mass Spectrometric Analysis

Joe Wang[1], Byron Ockerman[1], Joe He[2], Igor Novosselov[2]

[1] SpecTree Inc., 4625 Union Bay Pl NE, Seattle, WA, USA
[2] Department of Mechanical Engineering, University of Washington, Seattle, WA, USA

One of the major challenges in aerosol science is the rapid identification of airborne particulate composition on user-friendly, portable platforms with high molecular specificity. We demonstrate a compact microwell **aerosol-to-vapor (A2V) conversion system** that collects aerosol particles within a millimeter-sized volume and thermally desorbs the concentrated sample for direct introduction into a mass spectrometer.

We conducted a comprehensive validation of the A2V module's **particle-collection efficiency**, **thermal-desorption reproducibility**, and **analytical sensitivity** for representative aerosol-phase chemicals across the aerodynamic size range of 0.5–5 μm and sampling flow rates of 1-3 liters per minute. Collection efficiency is highest for particles with aerodynamic diameters> 1 μm (>85%) and remains above 50% for particles between 0.5 and 1 μm. Thermal desorption of analytes showed reproducible, consistent release with standard deviations <10%. Sensitivity assessments using dimethyl methylphosphonate (DMMP), tributyl phosphate (TBP), and levoglucosan yielded calibration curves ($R^2 > 0.99$) and detection limits in the low-nanogram range. In the aerosol-to-MS test, the combined sampling/recovery efficiency ranged from 50–70%, driven primarily by particle capture efficiency, analyte volatility, and transmission line losses.

This work establishes the utility of the microwell A2V system as a **fully-automated, field-compatible, detector-agnostic front end for aerosol chemical analysis**, enabling trace detection of vaporized compounds with mass spectrometric specificity and minimal sample processing. The approach is suitable for environmental monitoring, exposure assessment, and chemical threat surveillance where rapid, compound-specific aerosol characterization is required.

Towards Real-Time Pollen Monitoring in Southern Europe: A Novel Automatic Classifier

Yanick Zeder[1], Kilian Koch[1], Andreas Schwendimann[1], Elias Graf[1] and Erny Niederberger[1]

[1] Swisens AG, Emmen, 6032, Switzerland
Keywords: Aeroallergens, Validation, Pollen Classification, Automatic Pollen Monitoring, Air-flow Cytometer

Presenting author email: erny.niederberger@swisens.ch

Pollen and fungal spores trigger allergies and asthma in 15–40% of Europeans, causing annual costs exceeding €50 billion (Zuberbier et al., 2014; Tummon et al., 2021). Effective prevention requires reliable real-time pollen measurements, which in turn depend on automatic monitoring systems. We developed and validated a new automatic pollen classifier for Southern Europe to support real-time monitoring.

The location-dependent performance of such classifiers in Southern Europe is poorly studied due to limited deployments and high validation effort. To address this gap, a new classifier for the SwisensPoleno Jupiter airflow cytometer was developed and validated using data from four Southern European sites collected between 2023 and 2025.

The classifier uses a random forest model with novel morphological features extracted from two holographic images per particle, combined with a new pre-filter and confidence thresholding.

Performance was evaluated using Kendall's τ as proposed by Meurville et al. (2025), along with their benchmark values for quality assessment. Olea was excluded due to absence at the study sites. The benchmarks originate from parallel manual Hirst trap measurements at MeteoSwiss and represent very high reference quality. Matching or exceeding these benchmarks indicates performance comparable to or better than manual classification.

Table 1. Benchmark values for Kendall's τ from Meurville et al. (2025)

Factor	*Poaceae*	*Alnus*	*Betula*	*Corylus*
Switzerland (n=3)	0.64	0.48	0.63	0.50

Measurements were conducted in (Cordoba (ES), Barcelona (ES), Bozen (IT), San Michele all'Adige (IT)) for total eight seasons. Scaling factors for the automated system were the same across all locations and seasons, below the maximum of 24 proposed by Meurville et al. (2025). Table 2 shows the results.

Table 2. Mean Kendall's τ results by comparison of automatic pollen classification with new classifier and Hirst and manual classification

Factor	*Poaceae*	*Alnus*	*Betula*	*Corylus*	*Olea*
Italy (n=5)	0.66	0.57	0.59	0.74	0.53
Spain (n=3)	0.43	0.36*	*	0.63	0.61
Overall (n=8)	0.58	0.49	0.59	0.72	0.56

*Measured concentrations < 20 particles/ m^3

In Italy, *Poaceae*, *Alnus*, and *Corylus* met or exceeded their benchmarks, while Betula was slightly below. In Spain, Corylus exceeded its benchmark, whereas Poaceae fell below, likely because some Hirst-identified species were absent from the training data. For Alnus and Betula, concentrations were below the manual detection limit, making Kendall's τ unreliable.

Overall, *Corylus* and *Alnus* met or exceeded benchmarks in both countries, while *Poaceae* and *Betula* were slightly below. Although no benchmark exists for *Olea*, its Kendall's τ values fall between the Betula and Corylus benchmarks, indicating good performance.

The classifier therefore meets or exceeds benchmarks for major allergenic pollen types, supporting reliable real-time monitoring across Southern Europe.

Zuberbier, T., Orlow, S.J., Pajno, G.B., Shah-Hosseini, K., Roberts, G., Bousquet, J. (2014) Allergy. 69, 1275-1289.

Tummon, I., Smith, M., Johansson, P. (2021) Clinical and Translational Allergy. 11, 1-10.

Meurville, M., Keller, M., Steiner, A. (2025). Proc. EGUsphere Conference, [preprint].

Efficient Butanol Vapor Removal Eliminates Measurement Cross-Sensitivity and Health Risks

H.J. Schulz[1], V. Berger[1], P.S. Bauer[1], M. Dollner[1], J. Swanson[1,3], A. Boies[1,4]

[1]Catalytic Instruments GmbH & Co.KG, 83026 Rosenheim, Germany.
[2]University of Cambridge, Department of Engineering, Cambridge CB2 1PZ, United Kingdom.
[3]Minnesota State University, Mankato, MN 56001, United States.
[4]Stanford University, Department of Engineering, Stanford, CA 94305, United States.
Keywords: catalytic converter, catalyst, thermodenuder, scrubber, benzene.

Presenting author email: hans-joachim.schulz@catalytic-instruments.com

Butanol is commonly used as a working fluid in condensation particle counters (CPCs) due to its favorable physical properties for condensational growth of nanoparticles. Nevertheless, there are negative aspects of its use: Exposure to butanol vapor coming from the CPC exhaust can cause irritation of the eyes, nose, and throat, headaches, dizziness, and central nervous system depression (Segal et al., 2019; Catalytic Instruments, 2020). Therefore, it is considered a health hazard to the human body, which needs to be mitigated by occupational safety and health measures. Furthermore, butanol vapors can render parallel measurements invalid, if the discarded CPC exhaust plume reaches the inlet of other instruments. This is often the case with roadside emission measurements. Two types of measurement interference can be distinguished:

a) Butanol is correctly detected as a hydrocarbon and falsely attributed to an external source instead of the CPC.

b) Butanol exhibits cross-sensitivities for certain measurement principles, e. g. for the measurement of benzene, resulting in wrong readings of other instruments (Catalytic Instruments, 2024).

A simple method for avoiding these problems is to chemically convert butanol in the exhaust into non-toxic CO_2 and H_2O. This can be achieved safely and conveniently with a catalytic converter. In this study, the oxidation efficiency of a commercially available catalytic device, a Catalytic Vapor Filter (CVF) by Catalytic Instruments, is evaluated under various operating conditions. Two models were tested: a CVF100 and a CVF400-V with nominal flow rates of 1 and 4 L/min, respectively. A custom-built butanol vapor generator was used to simulate the exhaust gas of butanol-driven CPCs while being able to vary the flow rate (see Figure 1). Butanol concentration in air was set to approximately 9000 ppm to replicate typical CPC exhaust gas conditions. Butanol concentrations before and after the CVF were measured with a Flame Ionization Detector (FID). Comparing inlet and outlet concentration yields the butanol removal efficiency. Results show the CVF100 under test achieved a butanol removal efficiency of 99.9 % under nominal operating conditions. When processing diluted butanol vapor at concentrations of 2000 and 4000 ppm, removal efficiencies above 99.8 % were obtained. To investigate its robustness, the CVF100 was tested with butanol vapor flow rates above manufacturer specification (1 L/min). Removal efficiencies around 99.9 % were measured for flow rates up to 2.5 L/min, showing that the catalyst is designed with a safety factor. Nevertheless, the manufacturer specification is related to thermal design and safety and should not be exceeded.

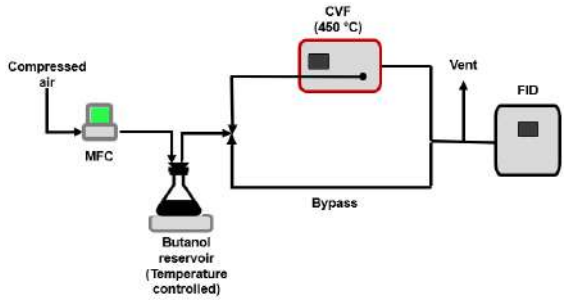

Figure 1. APT2026 Experimental setup. A custom-built butanol vapor generator simulates the exhaust gas of a butanol-driven CPC. The butanol removal efficiency of a Catalytic Vapor Filter (CVF) is determined using the CVF inlet and outlet butanol concentration readings from a Flame Ionization Detector (FID).

The results underscore the importance of the CVF as a significant contributor to improving measurement accuracy and reducing health risks in air quality monitoring stations and laboratories.

Segal, D., Bale, A. S., Phillips, L. J., Sasso, A., Starkey, C., & Makris, S. L. (2019) Issues in assessing the health risks of n-butanol. Journal of Applied Toxicology. https://doi.org/10.1002/jat.3820

Catalytic Instruments. (2020) Application Note: Health Risks of Butanol Vapor.

Catalytic Instruments. (2024) Application Note: Cross-Sensitivity of Butanol in Benzene Measurements.

Gas-phase chemistry and soot formation during shock-tube pyrolysis of methane at high fuel loadings

Mohammad Adib[1], Gibson Clark[2], Jahanbakhsh Jahanzamin[1], Chengze Li[2], Jesse W. Streicher[2], Enoch Dames[3], Shruthi Dasappa[3], M. Reza Kholghy[1], Ronald K. Hanson[2]
[1]Department of Mechanical and Aerospace Engineering, Carleton University, K1S 5B6, Canada
[2]Department of Mechanical Engineering, Stanford University, Stanford, CA 94305, USA
[3]Monolith Materials, Inc., San Carlos, CA 94070, USA
Keywords: Methane pyrolysis; High fuel loading; Carbon flux analysis; Kinetic modelling.

Presenting author email: reza.kholghy@carleton.ca

Direct decomposition of methane offers a low-emission route for large-scale co-production of carbon black (CB) and hydrogen. Achieving CB with desired specific surface area, morphology, and internal structure requires kinetic models coupled with particle dynamics to describe polycyclic aromatic hydrocarbon (PAH) formation and particle inception, but most kinetic models were developed for dilute conditions to minimize spectral interference in laser diagnostics (Kohse-Höinghaus *et al.* 2005). However, high fuel loadings (local mole fractions ~1) are typical in industrial CB synthesis (Fulcheri *et al.* 2023), highlighting the need for data to benchmark kinetic models across low- to high-fuel regimes.

In this work, we investigate the shock-tube pyrolysis of 5%, 10%, and 30% CH4-Ar mixtures at P_5=4±0.9 atm and 1800<T_5<2500 K, providing simultaneous measurements of key intermediates and soot volume fraction via optical diagnostics. The time-resolved mole fractions of methane (CH_4), ethylene (C_2H_4), and acetylene (C_2H_2) were quantified using laser absorption diagnostics, while a 633 nm light extinction diagnostic was utilized to quantify concentration of particulates. Simulations were conducted using several kinetic models coupled with a sectional population balance model to capture pyrolysis chemistry leading to soot formation, aiding the investigation of the processes bridging small molecule chemistry and particulate formation.

The measured CH_4 concentration was captured by all models relatively well at 5% and 10% loadings, but a large discrepancy was observed at 30% due to absorption interference. FFCM2 (Zhang *et al.* 2023) results are in good agreement with the three measured gas-phase species, but predict a faster C_2H_2 increase compared to other models due to its lack of PAH chemistry necessary for soot modeling.

The exclusive carbon pathways from CH_4 to C_2H_2, C_2H_4, and C_3H_3 were identified, and the corresponding carbon fluxes were compared for the kinetic models. Figure 1 illustrates major identified pathways of CH4 consumption. Carbon flux analysis highlighted the dominant role of C_3H_3 in channeling carbon toward C_2H_2 and PAHs, and the role of P-C_3H_4 as a key precursor of C_3H_3.

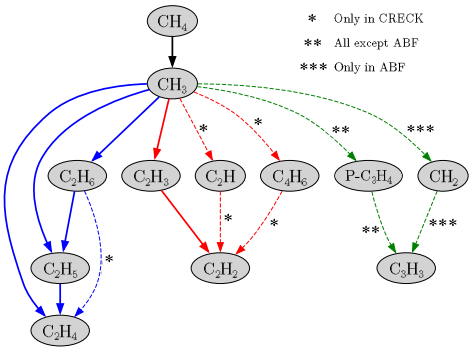

Figure 1. The common pathways for CH_4 conversion predicted using various kinetic models.

Soot volume fraction, fv predicted using CRECK (Pejpichestakul *et al.* 2019) successfully captures the time-behavior and temperature dependence of the measurements at 5% and 10% loadings, but a large discrepancy was found at 30% loading, indicating potential missing chemistry in the model that suppresses soot surface growth.

This research has received funding from the Canada Research Chairs #CRC-2019-232527 and NSERC #RGPIN-2019-06330, MITACS (#IT28731), and Monolith Materials, Inc.

K. Kohse-H¨oinghaus, R. S. Barlow, M. Ald´en, J. Wolfrum, Combustion at the focus: laser diagnostics and control, *Proc. Combust. Inst.* 30 (2005) 89–123.

L. Fulcheri, V.-J. Rohani, E. Wyse, N. Hardman, E. Dames, An energy-efficient plasma methane pyrolysis process for high yields of carbon black and hydrogen, *Int. J. Hydrogen Energ.* 48 (2023) 2920–2928.

Y. Zhang, W. Dong, L. Vandewalle, R. Xu, G. Smith, H. Wang, Foundational Fuel Chemistry Model Version 2.0 (FFCM-2) (2023)

W. Pejpichestakul, E. Ranzi, M. Pelucchi, A. Frassoldati, A. Cuoci, A. Parente, T. Faravelli, Examination of a soot model in premixed laminar flames at fuel-rich conditions, Proc. Combust. Inst. 37 (2019) 1013–1021.

An interdisciplinary consortium on FSP at Université Paris-Saclay: optimizing the operating conditions to tailor the size of iron oxide nanoparticles

B. Franzelli[a], A. Sottas[a,b], E. De Rolland Dalon[b], J. Bonnety[a], S. Iavarone[a], B. Podvin[a], O. Sublemontier[b], M. Briant[b], A. Bertrand[b], Y. Leconte[b]
[a]Laboratoire EM2C, CNRS, CentraleSupélec, Université Paris-Saclay, 91960 Gif-sur-Yvette, France
[b]Université Paris Saclay, CEA, CNRS, NIMBE, 91191 Gif-sur-Yvette, France
Keywords: real-time monitoring, low-order models, optical diagnostics, CFD simulations, iron oxides nanoparticles, single droplet combustion
Presenting author email: benedetta.franzelli@cnrs.fr

Inorganic nanoparticles (NP) are considered for a wide range of applications related to the energy transition and the environment (Pokhler and Madler 2020). Among the numerous synthesis methods for NP, increasing attention is being given to Flame Spray Pyrolysis (FSP) systems, allowing for rapid, single-step, large-scale, and cost-effective synthesis of NP with well-controlled composition, size, and morphology (Meierhofer and Fritsching 2021).

In this context, an interdisciplinary consortium between researchers from CNRS, CEA and CentraleSupélec has been created to develop a combined experimental-numerical framework for the automatic optimization of FSP systems, which will enable, in the future, to accelerate the sustainable production of new high-value-added complex nanoparticles (core-shell, metastable, multi-component, etc.) (Schneider et al. 2019, Sellmann et al. 2022). The partners are located on the Paris-Saclay campus. This proximity facilitates continuous exchanges, easy mobility for recruited students, sample sharing, participation in FSP experiments, and optimized use of equipment. The consortium aims to develop the key elements for deploying a rigorous optimization strategy for FSP: i) a significant advancement in knowledge about the NP synthesis process in flames, using optical diagnostics to enable 'in-flame' characterization of both the nanoparticles and the gas phase in reference academic configurations such as laminar prevaporized diffusion flames or turbulent spray flames; ii) the implementation of online monitoring techniques to measure the composition, size, and morphology of nanoparticles in the 'post-flame' zone of FSP systems; iii) the development of reduced-order models for FSP processes based on informed machine learning to predict the FSP system's response to operational conditions and to optimize online monitoring in the 'in-flame' zone; iv) the establishment of an FSP experimental platform open to research community for the automatic production of metal-oxides.

As a first step, in the framework of a joint PhD work led by A. Sottas, we are developing a framework capable of optimizing both the solution composition and the FSP operating conditions to tailor the size of a population of iron oxide nanoparticles. Indeed, when the metal precursor is mixed with pure ethanol, a droplet-to-particle reaction occurs, resulting in a highly polydisperse size distribution. However, when a mixture of ethanol and ethylhexanoic acid is used, a gas-to-particle mechanism takes place, yielding a much narrower size distribution (see Figure 1).

In parallel with experiments on the FSP reactor, we will develop a numerical approach to simulate the FSP process. To accurately account for the two possible synthesis pathways (gas-to-particle, droplet-to-particle), a model will first be developed to replicate the micro-explosion phenomena observed in FSP systems. The model will initially be validated using the combustion of an isolated evaporating droplet. In a second stage, the model will be coupled with a Large Eddy Simulation CFD approach to simulate the entire FSP system. Finally, low-order models will be built based on the obtained experimental and high-fidelity CFD database to predict the size characteristics of iron-oxide nanoparticles as function of the operating conditions, enabling in silico experiments in few minutes to reduce the number of trials required before finalizing the nanomaterial.

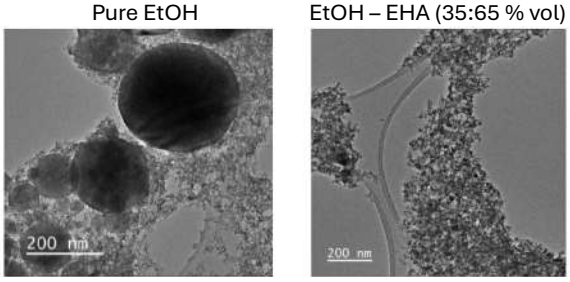

Figure 1 TEM images of iron oxides NP obtained in the FSP system at CEA from Fe(NO3)2 precursor mixed with (left) pure EtOH and (right) EtOH-EHA. The image has been realized by M. Vallet (SMPS, CNRS, CentraleSupélec, Université Paris Saclay).

Pokhrel S. and Mädler L. (2020), *Energy Fuels* **34**, 13209-13224.
Meierhofer F. and Fritsching U. (2021) *Energy Fuels*, **35**, 5495-5537.
Schneider F., Suleiman S., Menser J., Borukhovich E., Wlokas I., Kempf A., Wiggers H., Schulz C. (2019), *Rev.Sci. Instrum.* **90**, 085108.
Sellmann J., Wollny P., Baik S.-J., Suleiman S., Schneider F., Schulz, C., Wiggers H., Wlokas I., Kempf. A. (2022), *Pow. Tech.*, **404**, 117466.

Diffusive Transport of Linear Aggregates of Nano-spherical Particles

P.L. Garcia-Ybarra, A. Garcia-Corral and J.L. Castillo

Departmento de Fisica Matematica y de Fluidos, UNED, Las Rozas de Madrid, 28232, Spain
Keywords: aerosol aggregates, nano-particles, particle transport, diffusion, thermal diffusion.

Presenting author email: pgybarra@ccia.uned.es

The spherical particle is the standard morphology used in theoretical analyses to study the transport properties of aerosols in gases. However, aerosols commonly form aggregates of non-spherical shapes whose peculiar transport properties differ largely from those of spherical particles.

Industrial environments are usually the ground of two-phase particle-gas processes with large thermal gradients reigning in the carrier gas and/or with strong radiative fluxes. Thermal inhomogeneities induced on the particle surface and in the surrounding gas lead to the phoretic drift of the particles towards the cooler regions driven by radiometer forces. The study of this thermally induced transport of particles (termed as thermophoresis) is the objective of the present work because it may overwhelm the usual Brownian transport by orders of magnitude in these systems of practical interest.

The transport of particles smaller than the gas mean free path (large Knudsen numbers) can be analyzed by means of the kinetic theory of gases in the limit of free molecular flow approximation. Thermal differences in the environment induce an anisotropic transfer of momentum between the particle and the impinging/rebounding gas molecules (with the gas velocity distribution modified by the prevailing temperature gradient), exerting a finite non-zero themophoretic force on the particle.

The simple but still relevant case of a linear array of spherical particles was considered by Chan and Dahneke (1981) carrying out a Monte-Carlo simulation of the molecule collisions to get the resistance force on each concave unit consisting of two touching hemispherical caps. Also, analytical expressions for the resistance and themophoretical forces on convex bodies have been obtained, by adding the momentum transferred by the colliding molecules (Epstein, 1924; Waldmann, 1961; Garcia-Ybarra and Rosner, 1989; Rosner *et al*, 1991). However, this analytical method fails when the body has concave regions because the number of molecules arriving and leaving at each point of the concave site is not known a priori and must be computed by accounting for multiple internal reflections inside the concavity (Chaine, 1961). The limit case of completely diffuse gas-particle reflections becomes like a complex radiation problem, depending on the specific geometry of the concave region. Under this limit, the particular case of two touching hemispheres (as a unit cell) is an amenable problem that can be fully worked out.

Let us consider the incoming flow of gas molecules over the external surface of such a unit cell. To compute the total force on the hemispheres, the net momentum exchange is obtained by adding the momentum transferred by the impinging molecules from the surrounding space (the non-screened region) plus the one transferred by the leaving molecules reflected outwards. On the other hand, the internal reflections inside the concave region produce a zero net exchange of momentum. The solid angle intercepted by each sphere on any concave point of the opposite sphere is a cone. Then, the total screening undergone by each point is: this cone plus the half space screening due to its own sphere minus the common interception. From geometric considerations, the screening region is fully determined and the momentum transferred by the impinging molecules is obtained from the distribution function of the molecular velocities.

It remains to know the momentum transferred by the diffusively reflected molecules when they *evaporate* from the particle surface with velocities that follow a Maxwellian distribution function. This distribution function must be normalised to conserve the number of gas molecules. Imposing the balance between reflected and impinging molecules at each point in the concavity, a nonhomogeneous linear integral equation is obtained which can be solved by iteration as a von Neumann series.

Once the momentum transfer between the gas molecules and the concave unit is computed, the force on a straight array can easily be found.

Work supported by Ministerio de Ciencia e Innovacion of Spain [Grant no. PID2022-139082NB-C55 MCIN/AEI/ 10.13039/501100011033/FEDER, UE].

Chaine, M. T. (1961) In *Rarefied Gas Dynamics* (Edited by Talbot, L.) pp. 209-230. Academic Press.

Chan, P., Dahneke, B. (1981) *J. Appl. Phys.* **52**, 3106-3110.

Epstein, P.S. (1924) *Phys. Rev.* **23**, 710-733.

Garcia-Ybarra, P.L., Rosner, D.E. (1989) *AIChE Journal* **35**, 139-147.

Rosner, D.E., Mackowsky, D.W., Garcia-Ybarra, P.L. (1991) *Comb. Sci. Tech.* **80**, 87-101.

Waldmann, L. (1961) In *Rarefied Gas Dynamics* (Edited by Talbot, L.) pp. 323-344. Academic Press.

Development of a UV-Based Ion Source for Iodide Chemical Ionization Mass Spectrometry

A.C. Wagner[1], A. Rostedt[1] and M. Dal Maso[1]

[1] Aerosol Physics Laboratory, Physics Unit, Tampere University, FI-33014 Tampere, Finland
Keywords: instrument development, mass spectrometry, ion source, atmospheric

Presenting author email: andrea.wagner@tuni.fi

Iodide chemical ionization mass spectrometry (I^-–CIMS) is widely used for detecting oxygenated organic compounds, organic acids and inorganic halogens, amongst others (e.g., Huey et al. (1995)). Conventional approaches to generating iodide parent ions typically rely on radioactive ionization of methyl iodide (^{210}Po-based sources). These methods have demonstrated robust performance, but also the use of radioactive material comes with safety and regulatory constraints which make field deployment logistically intensive. Therefore, in recent years, an alternative was found in ultraviolet photolysis combined with charge-transfer chemistry (e.g., UV and charge transfer using benzene in addition to methyl iodide or ethyl iodide, as benzene has a higher UV cross-section (Ji et al. (2020); Riva et al. (2024)).

Here, we present a new non-radioactive ion source based solely on UV photolysis of methyl iodide (CH_3I). It does not use benzene as a high-UV-absorption charge-transfer medium, and instead relies exclusively on evaporated methyl iodide. The design was developed at Tampere University for the present Tofwerk H-TOF mass spectrometer and intended for dual use in gas-phase measurements and in combination with the FIGAERO inlet (Lopez-Hilfiker et al. (2014)) for particle-phase analysis. As most work of the group is field-campaign-based, a non-radioactive source was needed. A compact photoionization detection (PID) krypton lamp provides the photon flux needed to sustain parent-ion formation without the use of any auxiliary charge-transfer substance that could introduce contamination. Because the system omits the charge transfer from benzene, and the UV cross-section of methyl iodide is rather low, stable I^- production requires higher CH_3I concentrations together with intense UV illumination, and the flow and optical geometry were optimized accordingly.

The ion source was deployed both in laboratory conditions and during a field campaign, where it was used for gas- and particle-phase measurements. Under typical operating settings, reagent-ion spectra were dominated by I^-, I_3^-, and their respective water clusters, consistent with expected CH_3I photolysis chemistry.

Although several technical refinements have been identified for future versions, the current prototype already provides reliable parent-ion generation for laboratory studies and field campaigns. The results demonstrate that a purely photolytic CH_3I approach is a practical alternative within the existing landscape of iodide-CIMS ion sources, offering a non-radioactive and chemically simple implementation while maintaining performance suitable for gas- and particle-phase measurements.

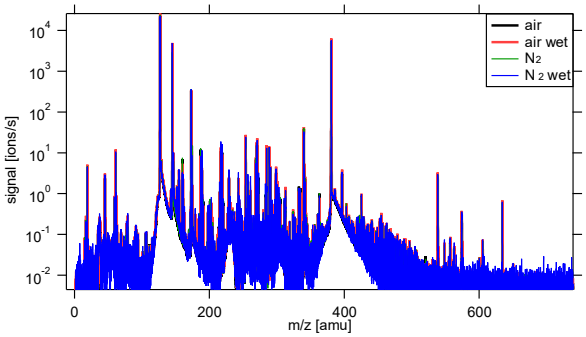

Figure 1. Exemplary spectra from the ion source. Dominant peaks are the parent-ions I^- and I_3^-.

This work was supported by the Research Council of Finland through the Condenz project under grant Nos. 310627 and 326437, and by the Academy of Finland Flagship programme ACCC under grant Nos. 337551, 357903, 359341 and 374288.

Huey, L. G. et al. (1995) The Journal of Physical Chemistry 99 (14), 5001-5008 DOI: 10.1021/j100014a021
Ji, Y. et al. (2020) Atmos. Meas. Tech., 13, 3683–3696, DOI 10.5194/amt-13-3683-2020
Lopez-Hilfiker et al. (2014) Atmos. Meas. Tech., 7, 983–1001, DOI 10.5194/amt-7-983-2014
Riva, M. et al. (2024) Atmos. Meas. Tech., 17, 5887–5901, DOI: 10.5194/amt-17-5887-2024

Field-Driven Particle Harvesting in Flames for Morphology and Wettability Control of Carbon Coatings

R. Griffo[1], A. Parisi[2], P. Minutolo[3], M. Minale[1], F. Di Natale[2] and C. Carotenuto[1]

[1]Department of Engineering, University of Campania "Luigi Vanvitelli", Aversa (Caserta), 81031, Italy
[2]Department of Chemical, Materials and Industrial Production Engineering, University of Naples "Federico II", Naples, 80125, Italy
[3]Institute of Science and Technology for Sustainable Energy and Mobility National Research Council (CNR) P.le Tecchio, Naples, 80125, Italy

Keywords: Carbon nanoparticles films, carbon-based coatings, electrophoretic capture, flame synthesis, hydrophilic film, superhydrophobic film.

Presenting author email: raffaella.griffo@unicampania.it

Carbon-based coatings with controlled wettability are of interest for a wide range of surface-engineering applications, including liquid-solid interaction control, protective coatings, and functional interfaces (Khan *el al.,* 2021). A simple route to fabricate such surfaces consists in directly harvesting flame-generated carbon nanoparticles onto solid substrates, avoiding multistep post-processing treatments.

In thermophoretic flame synthesis (ThFS), a substrate is intermittently inserted into a fuel-rich premixed ethylene/air flame, where carbon nanoparticles formed in the flame are driven toward the cooler surface by thermophoretic forces. As previously demonstrated for ethylene/air flames, tuning the flame regime enables the fabrication of either super-hydrophobic coatings under fully sooting conditions or hydrophilic ones under incipient sooting conditions (Commodo *et al.* 2016, Griffo *et al*., 2024).

However, incipient sooting flames, required to obtain carbon hydrophilic coatings, are characterized by very low particle concentrations and small particle sizes. As a result, purely thermophoretic deposition leads to extremely slow film growth, limiting the scalability and technological relevance of this approach.

In this work, we investigate Electric Field-Assisted Thermophoretic Flame Synthesis (E-ThFS) as an effective strategy to overcome this limitation. Carbon nanoparticle films are deposited from rich ethylene/air premixed flames under both incipient (Φ = 2,01, C/O = 0.67) and fully sooting (Φ = 2,46, C/O = 0.82) conditions, applying a negative electric potential (-1 to -3 kV) to the substrate. The applied electric field promotes particle harvesting by superimposing electrophoretic transport onto thermophoretic deposition, thereby enhancing nanoparticle capture during each flame insertion.

UV–vis spectroscopy reveals that the electric field increases the deposition rate by up to a factor of five under incipient sooting conditions, reducing the number of flame insertions required to reach functional film thicknesses. Raman spectroscopy confirms that the electric field does not alter the intrinsic carbon nanostructure. Optical profilometry shows that E-ThFS induces a transition from homogeneous layer-by-layer growth to heterogeneous, clustered morphologies with increased surface roughness.

Despite these morphological changes, wettability trends are preserved: films remain hydrophilic when produced under incipient sooting conditions, with final static contact angles in the range of ≈13-25°, and superhydrophobic under fully sooting conditions, with contact angles of ≈160-165°. Notably, incipient sooting films undergo a time-dependent wetting transition: an initial metastable superhydrophobic state (CA ≈ 160°), whose duration is voltage-dependent, collapses abruptly into a stable hydrophilic regime.

These results demonstrate that E-ThFS is a scalable and versatile approach for tailoring growth kinetics, surface morphology, and wettability of flame-deposited carbon coatings, with potential relevance for surface engineering and functional coatings.

This work was supported by the Italian Ministry of University and Research (MUR) through the PRIN 2017 project "MAGIC DUST" (Grant No. 2017PJ5XXX).

Khan, S. A., Ganeev, R. A., Boltaev, G. S., & Alnaser, A. S. (2021). Fullerenes, Nanotubes and Carbon Nanostructures, 29(8), 576-587.
Commodo, M., De Falco, G., Larciprete, R., D'Anna, A., & Minutolo, P. (2016). Experimental Thermal and Fluid Science, 73, 56-63.
Griffo, R., Di Natale, F., Minale, M., Sirignano, M., Parisi, A., Carotenuto, C. (2024) Nanomaterials. 14, 301.

Assessment of total and thermally resolved PM-bound water using Karl Fischer titration in areas with contrasting emission profiles

K.Widziewicz-Rzońca[1], D. Chyzhykov[1,2], M. Błaszczak[1], P. Rogula-Kopiec[1], K. Słaby[1], B. Mathews[1], M. Żurawka[1]

[1]Department of Air Protection, Institute of Environmental Engineering, Polish Academy of Sciences, M. Skłodowskiej-Curie St. 34, Zabrze 41-819, Poland
[2]Faculty of Energy and Environmental Engineering, Silesian University of Technology, Konarskiego St. 22B, Gliwice 44-100, Poland
Keywords: PM-bound water; Karl Fischer titration; evaporation spectra; aerosol characterization

Presenting author email: kamila.rzonca@ipispan.edu.pl

Atmospheric particulate matter (PM) contains variable amounts of particle-bound water, which plays a key role in aerosol physicochemical properties and represents a significant source of uncertainty in reference gravimetric PM measurements (Widziewicz-Rzońca et. al., 2020). The presence, chemical form, and thermal stability of PM-bound water depend on aerosol composition, atmospheric origin, and environmental conditions during sampling, filter conditioning, and weighing (Chyzhykov et. al., 2025). In this study, PM samples collected at two locations in southern Poland - Kraków (Steelworks) and Zdzieszowice (Coke plant) (Fig. 1) were analyzed to assess the content and forms of PM-bound water and their impact on mass measurement artefacts.

Figure 1. Sampling sites in Zdzieszowice (on the left) and T. Sendzimir Steelworks in Kraków (on right).

Water content in PM samples was determined by Karl Fischer titration coupled with thermal evaporation (Fig. 2), enabling analysis of evaporation spectra and differentiation among weakly bound, capillary, and chemically bound water fractions. A temperature-ramp program was used to evaluate the influence of PM chemical composition and potential emission sources on the resulting evaporation spectra.

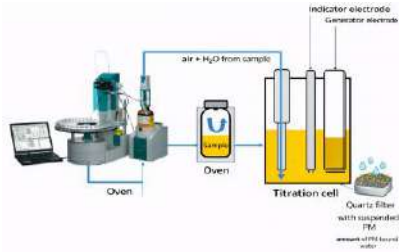

Figure 2. A measurement setup for conductometric KF titration using an oven-based system for the determination of PM-bound water.

The influence of sampling site, PM fraction, and filter type on PM-bound water contents was investigated. Statistical tools, including regression analysis, were applied to assess relationships between PM-bound water content and synoptic conditions during sampling: air temperature, relative humidity, wind speed, and direction to identify seasonal and spatial patterns in PM-bound water content.

Table 1. Comparison of dominant PM characteristics and expected PM-bound water (PBW) content at the steelworks and coking plant sites.

Feature	Steelworks (Kraków)	Coking plant (Zdzieszowice)
Dominant PM fraction	PM_{10} ↑	$PM_{2.5}$–PM_1 ↑
Key chemical components	Metals, metal oxides, Ca-rich slag	SO_4^{2-} / NO_3^- / NH_4^+, EC, OC, PAHs
Particle hygroscopicity	Low ↓	Moderate-High ↑
Water uptake mechanism	Surface adsorption (limited)	Hygroscopic growth + condensation
Sensitivity to RH	High (uptake mainly at high RH)	High, stable over wider RH range
Expected particle-bound water (PBW)	Lower ↓	Higher ↑

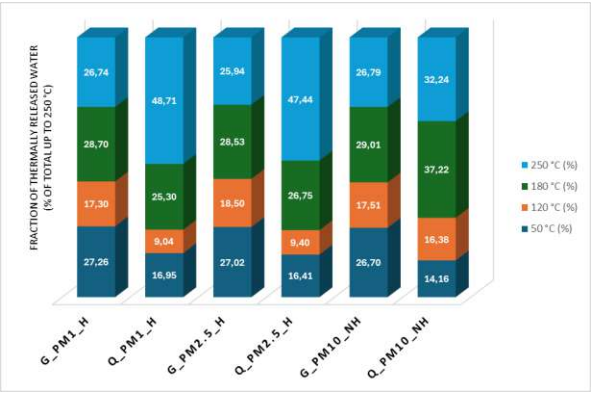

Fig 3. Average water contents in the PM mass (wt. %) for the PM_1, $PM_{2.5}$, and PM_{10} fractions in Krakow sampling site for heating (H) and non-heating (NH) seasons.

The thermal distribution of particle-bound water at the Krakow site (Fig. 3) depends on both filter material and particulate matter (PM) size fraction. When expressed as a percentage of the total water released up to 250 °C, distinct water-binding behaviors are observed for glass and quartz fiber filters.

For samples collected on glass fiber filters, water release is relatively evenly distributed across the 50–180 °C range for all PM fractions (PM1, PM2.5, PM10), with no single temperature step clearly dominating. This pattern indicates that water retained on glass filters is mainly weakly to moderately bound, associated with physically adsorbed water and hygroscopic inorganic components.

In contrast, quartz fiber filters show a pronounced shift toward higher desorption temperatures. For PM1 and PM2.5, the 250 °C step dominates the thermal profile, accounting for nearly half of the total released water, indicating the presence of strongly bound water associated with organic and soot-like aerosol components. For PM10 collected on quartz filters, the maximum water release occurs at 180 °C, suggesting a greater influence of mineral dust in the coarse fraction.

Overall, these results demonstrate that filter type plays a key role in shaping the apparent thermal distribution of aerosol-bound water, while PM size fraction further controls the relative contribution of strongly bound water.
The results demonstrate that PM-bound water significantly contributes to gravimetric mass and that its magnitude depends on both seasonal conditions and aerosol origin. The application of Karl Fischer titration provides a robust tool for identifying measurement artefacts and improving the reliability of PM mass determination, offering valuable insights for aerosol and particle technology research.

This work was supported by the National Science Centre in Poland under grant 2021/42/E/ST10/00209.

References:

Chyzhykov D, Widziewicz-Rzońca K, Mathews B. Variability of PM measurement results due to subsampling of filters and water content analysis. Chemosphere. 2025; 374:144177. doi: 10.1016/j.chemosphere.2025.144177.

Widziewicz-Rzońca, K.; Tytła, M.; Majewski, G.; Rogula-Kopiec, P.; Loska, K.; Rogula-Kozłowska, W. Strongly and Loosely Bound Water in Ambient Particulate Matter—Qualitative and Quantitative Determination by Karl Fischer Coulometric Method. Sustainability 2020, 12, 6196. doi: 10.3390/su12156196.

Advances in Fluorescence Probe Spectroscopy to Characterize Viscosity, and Other Physicochemical Properties of Aerosols

Angel M. Gibbons [1], Victoria G. Cover [1], and Paul E. Ohno [1]

[1]Department of Chemistry and Biochemistry, Auburn University, Auburn, AL, 36830, United States
Keywords: Viscosity, Fluorescence, Probe Spectroscopy, Time-correlated single-photon counting (TCSPC)

Presenting author email: amg0200@auburn.edu

The physicochemical properties of aerosols, including hygroscopicity, phase state, pH, and viscosity, impact the design and the performance of aerosol technologies like health and enviromental monitoring, pathogen mitigation systems, and molecular sensing. The determination of the relative humidity (RH)- and temperature-mediated physicochemical properties in situ has been challenging due to their small size and low number density in air.

Here, we present recent advances in the use of fluorescence probe spectroscopy to investigate the physicochemical properties of aerosols. This approach relies on incorporating fluorescent probe molecules, selected for their sensitivity to specific physicochemical properties, into aerosols. Importantly, this method provides in situ analysis and is applicable to both fine and ultrafine aerosols.

Viscosity is assessed using molecular rotor probes, such as 4-DASPI, whose fluorescence response depends on the local microviscosity. Figure 1 shows the instrumentation used to study aerosol viscosity in situ. Briefly, a picosecond laser is directed into a sample cell, where probe molecules in the aerosols are excited, and the resulting fluorescence emission is collected and directed to a photomultiplier tube (PMT). The fluorescence lifetime data is acquired using time-correlated single-photon counting (TCSPC) implemented on a PicoHarp system. Figure 2 shows the RH dependent lifetime response of the molecular rotor 4-DASPI in pure PEG particles.

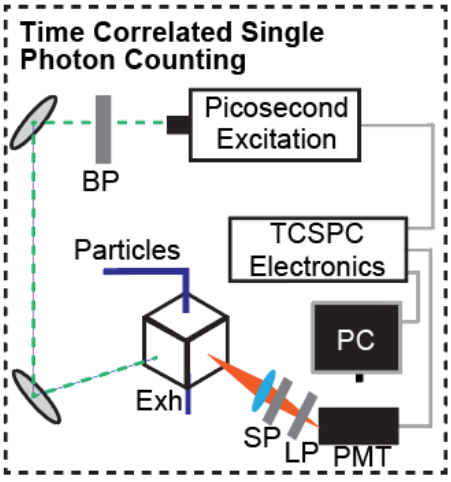

Figure 1. Schematic of the apparatus to study the viscosity of aerosols.

Furthermore, we demonstrate that volatilization of probe molecules from aqueous solutions via gentle heating, followed by condensation into the particles of interest, is a viable method for fluorescent aerosol labeling. This technique enables the study of real exhaled respiratory particles and ambient aerosols using fluorescence probe spectroscopy. Ongoing work focuses on optimizing this approach to additional probe molecules and expanding this work to help technological applications of aerosols.

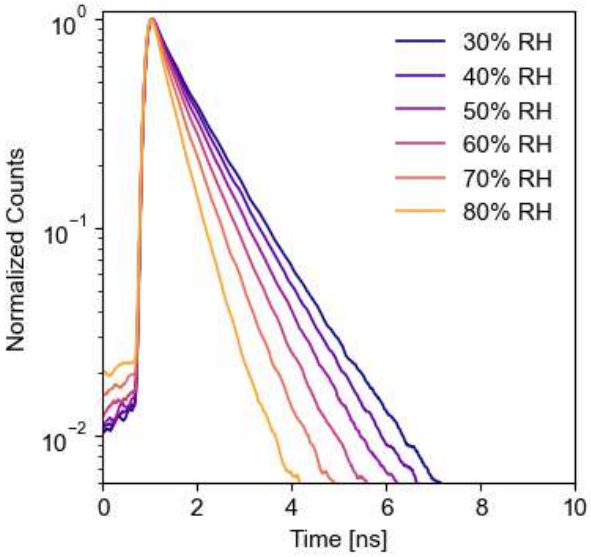

Figure 2. Fluorescent lifetimes as a function of RH for model PEG particles.

This work was supported in part by Auburn startup funding, the National Institute of General Medical Sciences of the NIH under Award Number R21GM155887, and AMG was supported by NSF GRFP.

Neveen Hosny, Clare Fitzgerald, Changlun Tong, Markus Kalberer, Marina Kuimova, Francis Pope. (2013) *Faraday discussions.* **165**, 343-356.

Paul Ohno, Yiming Qin, Jianhuai Ye, Junfeng Wang, Allan Bertram, Scot Martin. (2021) *ACS Earth and Space Chemistry.* **5**, 1223-1232.

Angel Gibbons, Michael Boadu, Paul Ohno. (2024) *Analytical Chemistry.* **96**, 19947-19954.

Titania Nanoparticles from Organometallic Precursors by Electrospray

P. Martínez Cánovas[1], F. Medina[1] and J. Rosell-Llompart[1, 2]

[1]Department of Chemical Engineering, University Rovira i Virgili, Tarragona, E-43007, Spain
[2]Catalan Institution for Research and Advanced Studies – ICREA, Barcelona, E-08010, Spain
Keywords: electrospray, TiO_2, nanoparticles, rutile, anatase.

Presenting author email: joan.rosell@urv.cat

Titania (TiO_2) nanoparticles are known for their photocatalytic activity (Erdemoğlu *et al*, 2008), among other applications. Superior performance was reported for dye-sensitized solar cells printed by electrospray than cells prepared by conventional methods like doctor blading or screen-printing (Zhao and Deng, 2020).

In electrospray, a liquid containing either TiO_2 nanoparticles or an organometallic precursor (e.g., titanium (IV) isopropoxide, TTIP) is electrostatically atomized from a Taylor cone meniscus which ejects a stationary microjet. The jet breaks up into electrically charged droplets which are electrophoretically driven towards a conductive substrate (Rosell-Llompart *et al*, 2018; Jaworek *et al*, 2018; Bodnár *et al*, 2018). Different TiO_2 particle morphologies have been reported (An and Ahn, 2012); however, the factors and mechanisms which determine those morphologies are not fully understood.

In this work, we aim to identify the relationship between the operational parameters of electrospray and the resulting morphology and crystallinity of the TiO_2 nanoparticles through a combination of techniques (SEM, TEM, XRD). We also investigate its dependence on the TTIP precursor concentration in ethanol.

Although water is probably responsible for the precipitation of titanium (as hydroxide), elevated moisture in the electrospray ambient caused precipitation at the Taylor cone, destabilizing it. Under dry ambient conditions, we produced TiO_2 nanoparticles which, after calcination, were comprised of small crystallites (Fig. 1). Analysis by XRD and TEM demonstrated a 70/30 anatase-rutile ratio with an individual crystalline domain size ranging from 20 to 40 nm (Fig. 1e-f). The produced nanoparticles are surrounded by abundant smaller particles which we identify as the relics from progeny droplets produced in Coulombic instabilities of the main droplets. The role of such tiny nanoparticles should be established in the future.

This study also contributes to the broader goal of understanding electrospray mechanisms responsible for the particle morphology and crystalline phase formation.

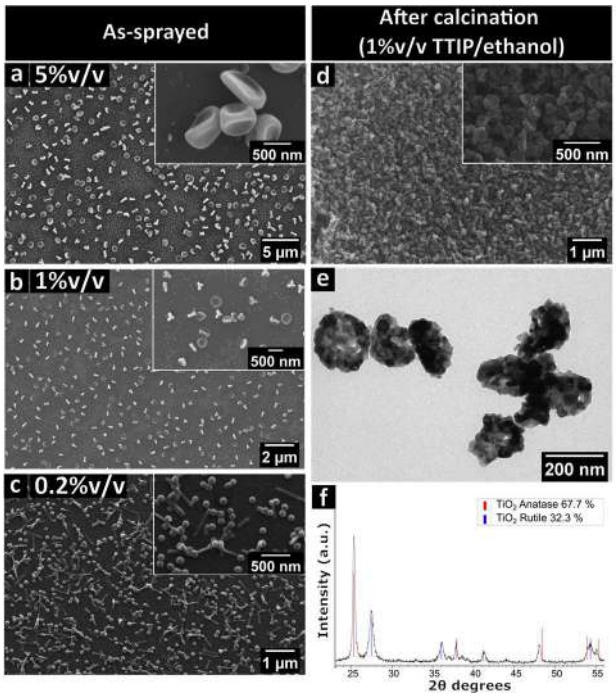

Figure 1. Electrosprayed nanoparticles at different solute concentrations in TTIP/ethanol solutions: (a,b,c) as-sprayed. For 1%v/v calcined (650°C): (d) SEM and (e) TEM images, and (f) XRD spectrum.

This work was supported by the Spanish Government and EU's ERDF under grant PID2021-129064NB-I00, by a FPU scholarship under grant FPU19/03733, and by the Catalan Government under grant 2021SGR-00978.

An, H., Ahn, H.-J. (2012). *Materials Letters*. **81**, 41–44.
Bodnár, E., Grifoll, J., Rosell-Llompart, J. (2018*). Journal of Aerosol Science.* **125**, 93–118.
Erdemoğlu, S., Aksu, S. K., Sayılkan, F., İzgi, B., Asiltürk, M., Sayılkan, H., Frimmel, F., Güçer, Ş. (2008). *Journal of Hazardous Materials*. **155(3)**, 469–476.
Jaworek, A., Sobczyk, A. T., Krupa, A. (2018). *Journal of Aerosol Science*. **125**, 57–92.
Rosell-Llompart, J., Grifoll, J., Loscertales, I. G. (2018). *Journal of Aerosol Science*. **125**, 2–31.
Zhao, X., Deng, W. (2020). *Opto-Electronic Advances*. **3(6)**, 190021–190038.

Field evaluation of the Spider-MAGIC mobility sizer in the Los Angeles area

S. Amanatidis[1], A. Eiguren-Fernandez[1], G.S. Lewis[1], S.V. Hering[1],
H. Baliaka[2], P. Kumar[2], J. H. Seinfeld[2], R. C. Flagan[2], N. L. Ng[2], R. Bahreini[3], A. M. Dillner[4], A. G. Russell[5]

[1]Aerosol Dynamics Inc., Berkeley, CA 94710, USA; [2]California Institute of Technology, Pasadena, CA 91125, USA; [3]University of California, Riverside, CA 92521, USA; [4]University of California, Davis, CA 95616, USA; [5]Geogia Institute of Technology, Atlanta, GA 30332, USA

Keywords: ambient air monitoring, particle size distribution, field evaluation
Presenting author email: arantza@aerosol.us

Particle electrical mobility spectrometry is one of the most prominent techniques for the measurement of sub-micron particle size and concentration. These instruments provide valuable data in aerosol research and air monitoring, but traditional mobility sizers are often not as fast nor as portable as desired.

In this work we report on the long-term field performance of a new, fast, compact dual-polarity mobility system called Spider-MAGIC.

Methods

Spider-MAGIC is a scanning electrical mobility sizer that combines the "Spider" radial-flow Differential Mobility Analyzer (DMA) (Amanatidis et al., 2020), and the "MAGIC" water-based Condensation Particle Counter (CPC) (Hering et al., 2019) into a compact, fully integrated, dual-polarity system (Model 810, Aerosol Dynamics Inc). It was operated alongside a TSI Scanning Mobility Particle Sizer (SMPS) at the Pico Rivera site of the ASCENT monitoring network in the Los Angeles area between Aug-Dec 2025. Additionally, total number concentrations were measured with a TSI 3783 water-CPC and three ADI community CPCs (Hering et al., 2025).

For the comparisons presented here, the Spider-MAGIC employed a Po210 charge conditioner and was operated at fixed sheath and aerosol flows of 0.9 L/min and 0.3L/min to span the 10-500 nm size range. Scans alternated between positive and negative polarities of both up- and downscans. Each scan was ~30 s.

The TSI SMPS was based on a TSI 3083 DMA with a negative voltage supply, a TSI 3789 water CPC, and a TSI 3088 Soft X-Ray charger. The system operated at 4.8 L/min sheath and 0.6 L/min aerosol flow, spanning the 13-800 nm size range with a time resolution of 152s.

Results

Figure 1 compares 10-min averaged data from the various collocated instruments. The two electrical mobility sizing instruments, Spider-MAGIC and the TSI SMPS, show good agreement in both the reported mean particle size and number concentration over their overlapping size range (13-500 nm). A strong correlation is also observed between the total number concentration from the Spider-MAGIC and the condensation particle counters.

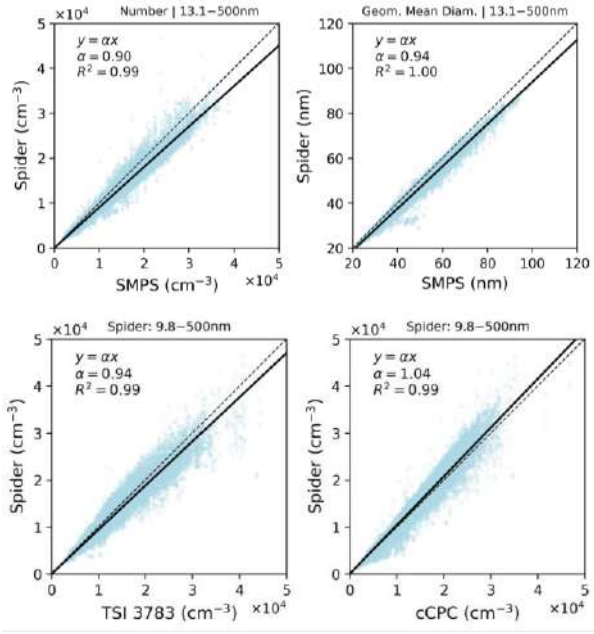

Figure 1. Comparison between Spider-MAGIC and TSI SMPS number concentration and mean size (top), and TSI 3783 CPC and ADI community CPC number concentration (bottom).

Because the Spider-MAGIC alternates between positive and negative polarity scans, the positive-to-negative ion mobility ratio (Z^+/Z^-) can be inferred from the raw data (Chen and Jiang, 2018). We find that this ratio varies over time from 0.725 to 0.801, and is lower than the fixed 0.875 value employed in the widely-used approximation by Wiedensohler (1988) for radioactive chargers.

This work was supported by the US Department of Energy under the DE-SC0022440 SBIR award.

References

Amanatidis, S. et al. (2020) *Aerosol Sci. Technol.* **54**(2), 175-189.
Hering, S. V. et al. (2019) *Aerosol Sci. Technol.* **53**(1), 63-72.
Hering, S. V. et al. (2025) *Aerosol Sci. Technol.* **59**(12), 1475-1485.
Chen, X. and Jiang, J. (2018) *Aerosol Sci. Technol.* **52**(10), 1145-1155.
Wiedensohler, A. (1988). *J. Aerosol Sci.* ***19*** *(3)*, 387-389

Breath of Health: Brine Aerosols under Controlled Sanatorium Conditions

Patrycja Rogula-Kopiec[1,2]*, Magdalena Żurawka[2], Jan Stefan Bihałowicz[3], Wioletta Rogula-Kozłowska[3], Magdalena Kostrzoń[4], Artur Badyda[1]
[1]Faculty of Environmental Engineering, Warsaw University of Technology, Warsaw, Poland
[2]Institute of Environmental Engineering, Polish Academy of Sciences, Zabrze, Poland
[3]Fire University, Warsaw, Poland
[4]Wieliczka Salt Mine Health Resort Wieliczka, Poland
Keywords: indoor/outdoor air, particulate matter, speleotherapy, health

Presenting author email: patrycja.kopiec@pw.edu.pl

One of the hallmark treatments used in spas is saline inhalation conducted in closed chambers. Such spaces are characterized by a stable temperature, high relative humidity, and air enriched with saline aerosol, while remaining largely free from common urban pollutants and allergens. The fine-particle fraction of the aerosol promotes its persistence in the air and facilitates penetration into the lower respiratory tract, which is considered a key factor supporting therapeutic benefits. Despite widespread clinical use and a long tradition, comprehensive data on the chemical composition, particle characteristics, and microbiological quality of saline-enriched air are still limited. Consequently, doubts remain regarding the actual patterns of inhalation exposure and the balance between potential therapeutic effects and health risks.

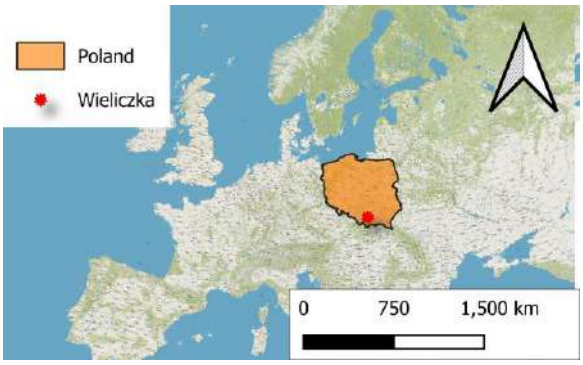

Figure 1 Map of with location of Wieliczka (Poland)

The Wieliczka Salt Mine (Poland) is a unique research center both nationally and across Europe. Its underground environment differs significantly from the surface environment in terms of microclimate stability, aerosol composition, and air exchange, making it highly suitable for comparative air quality studies. Measurements were conducted simultaneously at two locations. The underground site was in the "Lake Wessel" chamber, approximately 135 m below ground level. This environment is characterized by stable temperature and humidity, limited ventilation, and aerosols shaped by the natural properties of salt formation. The reference site was located outdoors, near the Daniłowicz's Shaft, in an area influenced by meteorological variability and local emission sources, including tourism. The parallel sampling project enabled direct comparison of particulate matter characteristics and pollutant levels in underground and ambient air. Air quality parameters were monitored using Palas AQ Guard 1200 multi-parameter analyzers (Palas GmbH, Germany), which use optical aerosol spectrometry and light scattering measurements, enabling continuous quantitative and resolved particle assessment.

Concentrations of $PM_{2.5}$ and coarser fractions were consistently higher underground than outdoors, which is typical for poorly ventilated subterranean environments. Mean $PM_{2.5}$ (9 µg/m³) and PM_{10} (32 µg/m³) remained below the daily limits of Directive 2008/50/EC and WHO guidelines; however, short-term peak values substantially exceeded these thresholds and may be relevant for sensitive individuals.

Despite compliance of mean values (also with the new Directive 2024/2881/EC, applicable from 2030), large standard deviations, high Q3, and maxima indicate pronounced temporal variability linked to occupancy and activity. The findings support the hypothesis that particle levels are driven mainly by resuspension of mineral dust caused by human movement. The low contribution of PM_1 points to negligible influence of combustion-related sources within the underground spa.

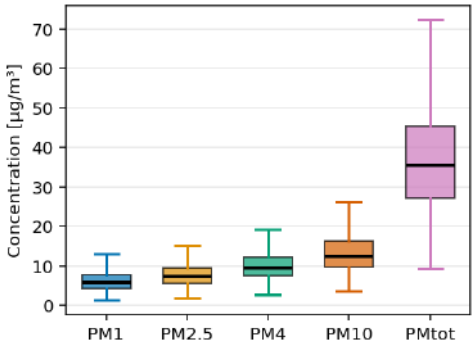

Figure 2. Boxplots of PM fractions in underground

This work was supported by Warsaw University of Technology within the Excellence Initiative: Research University (IDUB) programme, POSTDOC VI

Bralewska K. et al. (2022) *Int. J. Environ. Res. Public Health* **19(2)** 826.
Rogula-Kozłowska W. et al. 2017 *Pathobiology of Pulmonary Disorders*, Springer, 9-18

Reactive Indoor Atmospheres: Volatile Compounds and Ozone Chemistry in Beauty Salons

P. Rogula-Kopiec[1], M. Żurawka[1], W. Rogula Kozłowska[2], K. Widziewicz-Rzońca[1], A. Smola-Dmochowska[3], J.S. Bihałowicz[2]

[1]Institute of Environmental Engineering, Polish Academy of Sciences, Zabrze , 41-819, Poland
[2]Institute of Safety Engineering, Fire University, Warsaw, 01-629, Poland
[3]Centre of Polymer and Carbon Materials, Polish Academy of Sciences, Zabrze, 41-819, Poland

Keywords: Volatile organic compounds (VOCs), Indoor air quality, Occupational exposure, Air pollutants, Beauty salon.

Presenting author email: Magdalena.zurawka@ipispan.edu.pl

The study aimed to assess concentrations of selected air pollutants and evaluate exposure levels among employees and customers in hairdressing, beauty, and nail salons, taking into account service type and location. Air pollutants, especially VOCs and reactive gases, can cause respiratory irritation, allergies, and increase the risk of chronic diseases with long-term exposure (Raju et al (2020)). Measurements were conducted at 15 sites in the Upper Silesia region (Poland), including outdoor and indoor background locations, six hair salons (one children's salon treated as an indoor background), three beauty salons, and four nail salons.
During the 28-day campaign, sorbent-based methods were used to determine SO_2, NO_2, NH_3, O_3, VOCs, and formaldehyde. The results showed clear differences in air quality depending on service profile and location, confirming the significant impact of business activity on exposure levels.

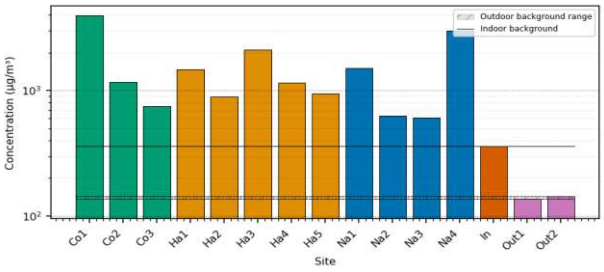

Figure 1 VOC concentrations (µg/m³) recorded at each beauty salon over four consecutive weeks. The bars show the weekly mean values for each site, and the shaded areas depict the range of indoor and outdoor background levels.

Indoor VOC concentrations were on average ten times higher than outdoors (1485.54 µg/m³ vs. 136.62–142.91 µg/m³), indicating the dominant role of indoor sources such as cosmetic products and treatments. The highest levels were observed at sites additionally affected by industrial and traffic emissions (e.g., Ha4 – 3976.16 µg/m³; Co1 – 2995.38 µg/m³; Na3 – 2124.88 µg/m³), highlighting the combined influence of indoor and outdoor sources. At the same time, unexpected findings were observed for ozone. As shown in Figure 2, ozone concentrations remained low in all salons despite elevated outdoor levels. This suggests that effective indoor removal of O_3 likely occurred through reactions with reactive pollutants, leading to the formation of secondary contaminants such as aldehydes and ultrafine particles.

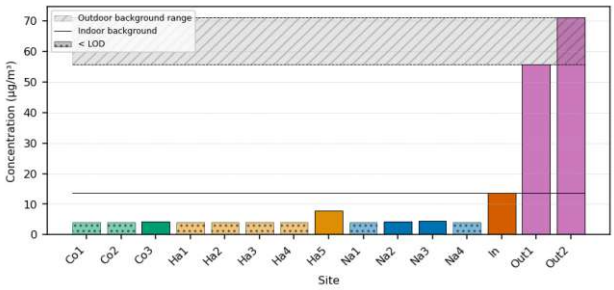

Figure 2 O_3 concentrations (µg/m³) recorded at each beauty salon over four consecutive weeks. The bars show the weekly mean values for each site, and the shaded areas depict the range of indoor and outdoor background levels.

This work was supported by NCN under grant 2021/41/B/ST10/04101;
https://repod.icm.edu.pl/dataset.xhtml?persistentId=doi:10.18150/P3W6X2&faces-redirect=true

Raju, S., Siddharthan, T., & McCormack, M. C. (2020) *Clinics in chest medicine*, *41*(4). Indoor air pollution and respiratory health, 825-843.

From Computation to Synthesis: Validating the Magnetic Properties of Pt_2FeNi

M. Pourhossein[1], M. Sedrpooshan[1,2], T. Krinke[1], R. Westerström[1], M.E. Messing[1,2]

[1]Department of Physics and NanoLund, Lund University, Lund, 22100, Sweden
[2]Department of Microtechnology and Nanoscience, Chalmers University of Technology, 412 96 Gothenburg, Sweden
Keywords: Rare-Earth-Free Permanent Magnets, Pt_2FeNi Nanoparticles, Spark Ablation, Compositional Engineering.

Presenting author email: Mohammad.pourhossein@fysik.lu.se

High-performance permanent magnets are critical components for green energy technologies, including electric vehicle motors and wind turbine generators. Currently, the market is dominated by rare-earth (RE)-based compounds such as $Nd_2Fe_{14}B$. However, the reliance on RE elements presents significant economic and supply-chain risks due to their uneven global distribution and concentration of production. Consequently, there is an urgent need to develop rare-earth-free alternatives that can achieve comparable cost–performance ratios.

Addressing this critical need via traditional materials discovery often relies on the experimental investigation of single compounds—a time-consuming and costly process with no guarantee of success. Integrating computational predictions with experimental validation offers a more robust pathway. Recent high-throughput simulations targeted 3d-5d transition metal compounds with high magnetocrystalline anisotropy (Vishina *et al* (2020)). Among predicted candidates, bulk Pt_2FeNi demonstrated the best performance, with a calculated Magnetic Anisotropy Energy (MAE) > 2 MJ/m^3 and saturation magnetization of 1T—properties approaching standard rare-earth magnets like $Nd_2Fe_{14}B$, making it a compelling candidate.

While the computational study focused on the bulk phase, experimental realization and characterization of these materials—in both bulk and nanoscale forms—remain unexplored. We focus specifically on the nanoscale, where magnetic materials are expected to enter the single-domain regime and exhibit enhanced functional properties. (Montsouka *et al* (2006)). Consequently, the primary objective of this study is to synthesize Pt_2FeNi nanoparticles to experimentally validate whether the predicted intrinsic bulk properties translate to real-world nanomaterials. However, simulation data indicates that practical application is constrained by high costs and a low Curie temperature (T_C = 230 K), preventing operation at room temperature. To address these limitations, the second phase of this work employs compositional engineering strategies. Guided by computational refinements which predicted that replacing 3d metals with Cobalt (e.g., Pt_2CoNi and Pt_2FeCo) increases the T_C to 385–605 K while preserving high anisotropy (up to 6.83 MJ/m^3), we specifically investigate the partial replacement of transition metals with Cobalt (Co). While we recognize that Cobalt is also an expensive resource, this modification is essential to compensate for the low Curie temperature. To mitigate the overall material cost, we concurrently explore the isoelectronic substitution of Platinum (Pt) with Nickel (Ni) or Palladium (Pd).

To experimentally realize these complex alloy compositions with high precision, we utilized aerosol-based spark ablation—a method selected for its unique ability to control nanoparticle stoichiometry and morphology. The generation system comprised an alloyed FeNi electrode (1:1 atomic ratio) paired with a high-purity Platinum (Pt) electrode. To promote metallic phase formation and inhibit in-flight oxidation, the synthesis was conducted within a reducing atmosphere (95% N_2 + 5% H_2). We will present the results of the physicochemical characterization. The methods used included X-ray Diffraction (XRD), Scanning and Transmission Electron Microscopy (SEM & TEM), and Energy Dispersive X-ray Spectroscopy (EDS) to elucidate crystal structure, morphology, and elemental composition. Complementary magnetic characterization is scheduled to utilize Vibrating Sample Magnetometry (VSM).

This study bridges the gap between theoretical prediction and experimental realization, specifically demonstrating the unique capability of spark ablation as a rapid prototyping tool for complex functional alloys in aerosol science.

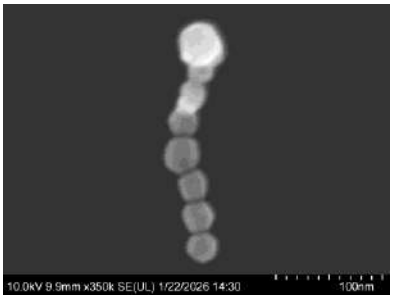

Figure 1. SEM image of the Pt_2FeNi nanoparticles

This work was supported by the Wallenberg Initiative Materials Science for Sustainability (WISE) and NanoLund.

Vishina, A., Vekilova, O.Y., Björkman, T., Bergman, A., Herper, H.C., Eriksson, O. (2020) Phys. Rev. B.101, 094407.

Montsouka, R.V.P., Arabski, J., Derory, A., Faerber, J., Schmerber, G., Pierron-Bohnes, V. (2006) Mater. Sci. Eng. B.126, 236-239.

A Study on the Internal Dose Assessment of Workers due to Radioactive Aerosol Inhalation

[1]DoWon-Hyeun,[1]SangRyeol-Yoon *JongSong-Soon

[1]Department of Nuclear Engineering, Chosun University, Gwangju city,61452, Republic of Korea
Keywords: Internal Dose Assessment, Radioactive Aerosol, IMBA code
burylibrary@chosun.kr

1. Introduction

Radioactive liquid waste spills in nuclide separation processes pose severe internal exposure risks to workers through aerosol inhalation. Because internalized nuclides deposit in target organs causing prolonged damage, precise assessment is essential. This study evaluates internal doses using the IMBA code under a hypothetical spillage scenario to establish effective protection strategies.

2. Materials and Methods

The IMBA (Integrated Modules for Bioassay Analysis) code was used to calculate internal doses based on ICRP biokinetic models (HRTM, HATM). It simulates radionuclide transfer and deposition to estimate organ-specific effective doses.

The assessment models a hypothetical accidental spillage of liquid radioactive waste during nuclide separation, assuming immediate aerosol dispersion and acute inhalation. Target nuclides included ^{3}H, ^{14}C, and ^{90}Sr, selected for their high volatility and radiotoxicity as major beta-emitting byproducts in liquid waste. Default values recommended by the ICRP for occupational workers were applied for key input parameters, including an Activity Median Aerodynamic Diameter (AMAD) of 5 µm, a breathing rate of 1.2 m^3/h (Light Work), and absorption types (Type F and M) (Table 1).

Table 1. IMBA input parameters

Parameter	Value	
Intake Scenario	Acute Inhalation	
AMAD	5 µm	
Breathing Rate	1.2 m^3/h	
Absorption Type	^{3}H	Type F
	^{14}C, ^{90}Sr	Type M
Biokinetic Model	ICRP 68	
Concentration	^{90}Sr	1.64E+05 Bq
	^{14}C	1.79E+05 Bq
	^{3}H	7.49E+06 Bq

3. Results

Simulations revealed distinct exposure patterns based on nuclide biokinetics. ^{14}C and ^{90}Sr (Type M) exhibit prolonged pulmonary retention, delivering sustained radiation to lung tissues. For ^{14}C, this resulted in a total effective dose of 2.95E-01 mSv, with significant localization in the lungs (2.51E-01 mSv). ^{90}Sr, a bone-seeking nuclide, primarily deposits on bone surfaces; it contributed the highest total effective dose of 9.20 mSv, with the Red Bone Marrow (R.B.M) receiving 5.63 mSv as the critical organ. Conversely, ^{3}H dissolves rapidly into body fluids and distributes systemically, resulting in a negligible total effective dose (1.50E-02 mSv) and uniform distribution.

Table 2. Evaluation results of internal effective dose for major organs

	Effective Dose (mSv) Total		
Nuclide / Target Organs	^{90}Sr	^{14}C	^{3}H
Urinary Bladder	2.01E-02	2.50E-03	7.42E-04
Breast	8.82E-03	2.50E-03	7.42E-04
Liver	8.82E-03	2.50E-03	7.42E-04
Thyroid	8.82E-03	2.50E-03	7.42E-04
R.B.M.	5.63E+00	6.00E-03	1.78E-03
Bone Surface	1.07E+00	5.00E-04	1.48E-04
Stomach	2.36E-02	6.51E-03	1.90E-03
Skin	1.76E-03	5.00E-04	1.48E-04
Lung	2.29E+00	2.51E-01	1.78E-03
Colon	8.11E-02	6.00E-03	1.78E-03
Esophagus	8.82E-03	2.50E-03	7.42E-04
Gonads	3.53E-02	1.00E-02	2.97E-03
Remainder	8.96E-03	2.53E-03	8.03E-04
TOTAL	9.20E+00	2.95E-01	1.50E-02

4. Conclusion

This study assessed internal exposure from radioactive aerosol inhalation using the IMBA code. While the total effective dose (9.51 mSv) remains within the occupational annual limit (20 mSv), it significantly exceeds the public annual limit (1 mSv). Therefore, strict containment measures and respiratory protection are essential to ensure radiological safety. Future research will focus on refining input parameters through empirical experiments to minimize uncertainties in the assessment model.

5. Reference

[1] ICRP. (1994) Ann.ICRP.24(4)
[2] ICRP. (1994) Ann.ICRP.24(1-3)
[3] Birchall, A., Puncher, M., Marsh, J.W., Davis, K., Bailey, M.R., Jarvis, N.S., Peach, A.D., Dorrian, M.D., James, A.C. (2007) *Radiat. Prot. Dosim.* 125, 194-197.
[4] Lee, M.H., Lee, S.H., Ha, W.B., Yu, H.J., Song, J.S. (2025) *Sci. Technol. Nucl. Install.* 2025, 1408025.

6. Acknowledgements

This work was supported by the Radiation Technology Commercialization Support Program (RS2025-25396500) funded by the Ministry of Science and ICT (MSIT).

Electrical-Field-Focused Aerosol Assembly of Embedded 3D Ag Nanostructures for Flexible Transparent Electrodes

G. Kim[1, 2], J. Shin[2], S. Cho[2, 3], S. Song[1, 2], K. Park[2, 3], D. Yoon[2, 3], Y. S. Lee[2, 3], N. Ahn[1, 2] and M. Choi[2,3]

[1]Department of Integrated Display Engineering, Yonsei University, Seoul 03722, South Korea
[2]Global Frontier Center for Multiscale Energy Systems, Seoul National University, Seoul 08826, South Korea
[3]Department of Mechanical Engineering, Seoul National University, Seoul 08826, South Korea

Keywords: Aerosol Deposition, E-field focusing, Metal nano-grid, Transparent & Flexible electrode.

Presenting author email: g_kim@yonsei.ac.kr

Flexible and transparent conducting electrodes (TCEs) with high mechanical durability are essential for emerging foldable, wearable, and large-area electronic devices[1]; however, conventional transparent electodes suffer from an intrinsic trade-off between electrical performance, optical transparency, and mechanical robustness[2]. Here, we demonstrate a hybrid transparent electrode combining Ag vertically elongated nano-grid with a thin indium tin oxide (ITO) enabled by atmospheric aerosol deposition.

Ag aerosol nanoparticles are generated via spark discharge and selectively deposited onto photolithographically defined micro-patterns under a strong electric field, where field focusing due to ion accumulation induces the formation of high-aspect-ratio 3D Ag nano-grid with characteristic feature sizes down to 100 nm [3,4]. Following photoresist lift-off, the aerosol-assembled Ag structures are directly embedded into a CPI matrix through spin coating and thermal curing, allowing mechanical peel-off without any interfacial treatment[5]. A 360 nm thick indium tin oxide (ITO) layer is subsequently sputtered onto the embedded structure, forming a hybrid ITO/Ag/CPI transparent electrode.

The resulting Ag electrodes with a line width of 4.5 um and a height of 170 nm exhibit a low sheet resistance of 7.1 Ω sq^{-1} with an average optical transmittance of 83% in the visible range over 2.5 × 2.5 cm^2, while an ITO electrode without the Ag nano-grid shows a sheet resistance of 9.1 Ω sq^{-1} and transmittance of 84%. The vertically elongated geometry of the Ag nano-grid effectively improves electrical conduction without compromising optical transmission. In addition, the hybrid electrodes demonstrate excellent mechanical reliability, retaining more than 90% of their initial conductivity after 10^4 bending cycles at a bending radius of 1 mm.

The metal electrode thickness can be freely patterned from 100 nm to 10 um, as exemplified by Au nano-grids with a height of 578.4 nm and a width of 98.6 nm, enabling monolithic integration of transparent conducting regions and low-resistance current-collecting architectures within a single process. Moreover, centimetre-scale electrodes up to 10 × 10 cm^2 can be fabricated using the same process.

This work highlights electric-field-focused aerosol deposition as a powerful route for deterministic 3D nanostructure assembly and demonstrates its potential for scalable, ambient fabrication of high-performance flexible transparent electrodes for next generation optoelectronic applications.

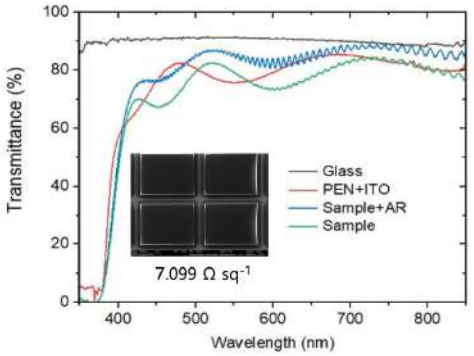

Figure 1. Optical transmittance spectra of aerosol-assembled Ag nanostructure embedded into CPI & ITO.

	Glass	PEN+ ITO	This work
Average T (%) (400-800 nm)	90.35	79.32	83.08
Sheet resistance (Ω sq^{-1})	-	9.056	7.099

Table 1. Comparison of average optical transmittance in the visible range (400-800 nm) and sheet resistance.

This work was supported by the Global Frontier R&D Program of the Center for Multiscale Energy Systems and the National Research Foundation (NRF) under the Ministry of Education, Science and Technology, Korea (RS-2023-00282896 & RS-2023-00279529).

[Reference]

[1] D. S. Hecht, et al., (2011) *Advanced Materials.* **23**, 1482-1513.
[2] S. De, et al., (2009) *ACS Nano.* **3,** 1767-1774.
[3] H. Kim, et al., (2006) *Nature Nanotech*. **1**, 117-121.
[4] W. Jung et al., (2021) *Nature.* **592**, 54-59.
[5] U. Kim et al., (2023) Advanced Energy Materials. 13, 2203198.

Electrospray Deposition of Gold-Doped Carbon Films for Energy and Sensing Applications

A. Parisi[1], R. Griffo[2], S. Arcopinto[1], C. Carotenuto[2], and F. Di Natale[1]

[1]Department of Chemical, Material and Industrial Production Engineering, University of Naples Federico II, Naples, 80125, Italy

[2]Department of Engineering, University of Campania "L. Vanvitelli", Aversa, 81031, Italy

Keywords: electrospray deposition, gold-doped carbon films, cone-jet stability, gas sensing, catalysis

Presenting author email: arianna.parisi@unina.it

The demand for sustainable energy technologies and advanced sensing systems is driving the development of tailored surface and transport properties of multifunctional materials. Renewable hydrogen production and fuel cell technologies have recently gained centre stage in discussions on the transition toward low-carbon energy systems, while gas sensing plays a crucial role in process monitoring, safety, and environmental control.

In this context, carbon-based materials have become increasingly attractive on account of their remarkable physicochemical properties, which encompass high surface area, electrical conductivity, chemical stability, tunable porosity, and easily functionalized surfaces. Noble metals such as gold can be doped into carbon materials and, by so doing, increase the density and activity of surface sites and further modify interfacial and electronic properties. In this regard, gold-doped carbon systems are a versatile class of materials exhibiting functionality that far exceeds that of pristine carbon substrates.

There are several kinds of carbonaceous supports, such as carbon black, activated carbons or flame-derived carbon nanopowders, whose selection depends on the desired particle size distribution, surface chemistry, and degree of porosity. Following that, the gold may be incorporated by various methods, such as impregnation with metal precursors or adsorption from metal-containing solutions, allowing control of metal loading and dispersion.

This work reports experimental studies concerning the production of waste-derived gold-loaded carbon films produced through hydrometallurgical recovery of gold from waste electrical and electronic equipment (WEEE) and electrospraying. Gold is extracted from WEEE and adsorbed onto carbon materials, which are then directly used for the deposition ink formulation without additional purification steps.

When these gold-doped carbon materials are processed into thin films, functional surfaces are delivered that can be integrated into a variety of devices. To be effective in industrial applications, these films must exhibit uniform thickness, surface homogeneity, strong substrate adhesion, mechanical robustness, and controlled wettability, all of which strongly depend on the deposition method.

While the hydrometallurgical process allows fine-tuning of the gold adsorption, the electrospray deposition is used as a versatile technique in the preparation of uniform and nanostructured coatings with fine control over morphology and composition.

During electrospraying, high voltage is applied to a liquid suspension flowing through a capillary needle, thus producing a stable cone-jet that subsequently breaks up into charged microdroplets. These droplets are transported by the electric field and deposited onto a grounded or biased collector, forming homogeneous films. Compared to conventional deposition techniques such as spin coating or airbrushing, electrospray deposition offers improved reproducibility, enhanced control over porosity, and the possibility to operate at low material consumption.

This work provides stability diagrams of gold-doped carbon suspensions as a function of the gold mass fraction, together with some crucial process parameters, such as liquid flow rate, applied voltage, and needle-to-collector distance. It investigates how these parameters may affect the cone-jet stability domain, together with the effects of the gold content on electrospray behaviour.

The experimental results are interpreted in light of established electrospray scaling laws for droplet size and charge, providing insight into process productivity and associated electrical energy consumption. Thin films produced under the optimal electrospraying conditions are characterised in terms of surface morphology and wettability, using scanning electron microscopy and sessile droplet contact angle measurements.

The combined analysis of stability, deposition efficiency, and film properties provides useful indications on the potential application of gold-doped carbon films in catalysis and sensing technologies.

Karczmarska, A., Adamek, M., El Houbbadi, S., Kowalczyk, P., & Laskowska, M. (2022). *Crystals* 12(5), 584.

Trucillo, P., Lancia, A., & Di Natale, F. (2022). J. Environ. Chem. Eng., 10(3), 107730.

Castillo, J. L., Martin, S., Rodriguez-Perez, D., Higuera, F. J. and Garcia-Ybarra, P. L. (2018). *J. Aerosol Sci.* 125, 148-163.

Aerosol Nanoparticle Synthesis by Inductive Heating

N.Sochorakis[1,2], C.Loizides[1] and G.Biskos[1,3]

[1]*The Cyprus Institute, Climate and Atmosphere Research Centre, Nicosia 2121, Cyprus*
[2]*Nanomicron Ltd., Nicosia, 2121, Cyprus*
[3]*Faculty of Civil Engineering and Geosciences, Delft University of Technology, 2628 CN, Delft, The Netherlands*
Keywords: Inductive Heating, , Metal, MOX
Presenting author email: n.sochorakis@cyi.ac.cy

Aerosol technology offers advantageous methods for synthesizing well-defined nanoparticles[1]. Here we present a new evaporation-condensation aerosol nanoparticle generator that relies on inductive heating[2]. The metal vapours produce by heating the workpiece, are subsequently carried away and cooled down by a gas stream to yield atomic clusters and nanoparticles (singlets and agglomerates) by nucleation and subsequent growth by condensation and coagulation (Fig. 1). By passing an alternating current through a coil, a fluctuating magnetic field induces eddy currents and magnetic hysteresis—in the case of ferromagnetic workpieces like iron—allowing for rapid and highly localized heating (Fig. 2).

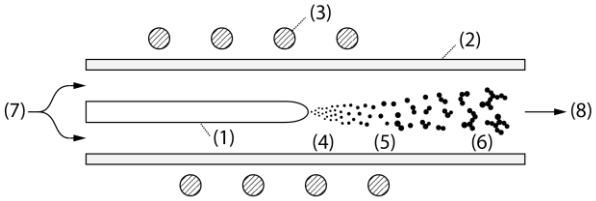

Figure 1. Schematic of the inductive heating nanoparticle generator, comprising of (1) the heated workpiece with (2) glass tube, (3) a coiled inductive heater, (4) the vapours produced by the workpiece yield atomic clusters that subsequently grow to form (5) singlet and (6) agglomerated nanoparticles. The glass tube has an inlet (7) from where the carrier gas is introduced, and an outlet (8) through which the produced nanoparticles exit.

The novelty of the method relies on the fact that the only material in the heating zone is the target workpiece, avoiding any holders that can unintentionally emit impurities upon heating either directly by the inductive heater or indirectly by the heated target workpiece.

Figure 3 shows measured concentration of the nanoparticles as a function of time (Fig. 3a) and size distributions of the nanoparticles produced by the inductive heating aerosol nanoparticle generator for different operating flow rates (i.e., 1, 10 and 30 lpm; Fig. 3b). The measurements were recorded by a Scanning Mobility Particle Sizer. Evidently the system can produce nanoparticles over a wide size range depending on the operating conditions, which apart from the flow rate also include the input electrical energy to the system.

Acknowledgement: This work is supported by the project EXCELLENCE/0524/0307 (ANCHOR), co-funded by the European Regional Development Fund (EDRF) and the Research and Innovation Foundation (RIF) of the republic of Cyprus

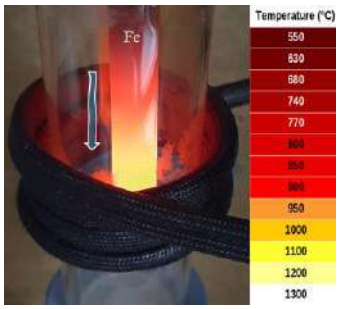

Figure 2. Picture of the inductive coil, the glass tube, and a heated iron workpiece of the heating generator operating with N_2 as the quenching gas.

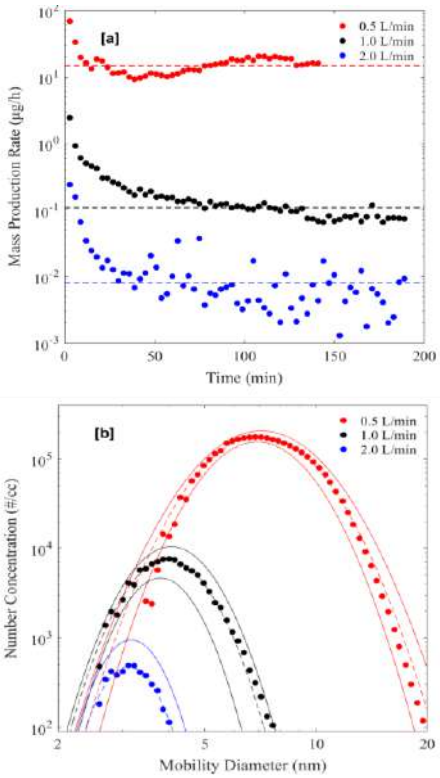

Figure 3. Flow rate affecting both nanoparticle concentration (a) and size distribution (b).

References

1. Sohail, A., (2025) Next Nanotechnology. **, 8.**
2. Nakum, V., Mehta,N., (2013) International Journal of Science and Engineering Applications. **2**. 141.

Multiplexed Coaxial Electrospraying for Continuous Production of Crosslinked Chitosan Nanoparticles

Y. Pérez-Pacheco[1], E. Bodnár[1], A. Oulad-Ali[1], R. Garcia-Valls[1] and J. Rosell-Llompart[1,2]

[1]Department of Chemical Engineering, University Rovira i Virgili, Tarragona, E-43007, Spain
[2]Catalan Institution for Research and Advanced Studies ICREA, Barcelona, E-08010, Spain
Keywords: chitosan, biopolymers, nanoparticles, coaxial electrospray, encapsulation.

Presenting author email: joan.rosell@urv.cat

Chitosan based nanoparticles have gained interest for their biocompatibility, biodegradability and muco-adhesive properties, making them ideal carriers for bioactive compounds (Sandri *et al*, 2012). Crosslinking enhances nanoparticle structural stability and enables the controlled release by modulating the polymer network in response to environmental stimuli such as pH. Specifically, pH dependent protonation of chitosan amino groups, together with the crosslinking density, governs charge distribution, matrix swelling and diffusion of encapsulated species. Those characteristics make chitosan nanoparticles useful for applications in medicine, food cosmetics, and agriculture. Our goal is to develop electrospray configurations and formulations of precursor water-based solutions to obtain stable production of the crosslinked chitosan nanoparticles for encapsulation of a broad range of active chemicals.

Using the coaxial electrospraying approach, we have demonstrated stable continuous production of those nanoparticles loaded with a range of compounds, such as copper salts, caffeine, resveratrol and curcumin. Our system is developed for electrospraying in-situ cross-linking water-based solutions with autonomous coaxial nozzles, differing from other novel multiplexing approaches (Olvera-Trejo *et al*, 2016; Jeong *et al*, 2022).

A proof-of-concept setup was developed for 8 sprayers in a scalable circular arrangement. In this configuration, the electrostatics are the same for all the nozzles, thus avoiding edge-effects (Sochorakis et al., 2019). In each Taylor cone, the chitosan solution constitutes the outer flow. The stability of the cones was inspected visually (Fig. 1A) and by monitoring the overall electrospray current on the collector. The nanoparticles arrived at the collector forming uniform deposition spots (Fig. 1B). Field Emission Scanning Electron Microscopy (FESEM) imaging of the nanoparticles (Fig. 1C-G) revealed globular shapes and that relatively homogeneous sizes, under about 200 nm. The particles collect forming aggregates, suggesting the role of the non-zero electrical conductivity of the particulate film while it forms (Higuera, 2018). Despite differences in the mechanisms involved, similarly looking porous films were also obtained in the electrospraying of nanoparticle suspensions (Zhu & Chiarot, 2017; Castillo *et al*, 2018).

We have demonstrated stable multiplexed coaxial electrospray for a range of aqueous solutions with in-situ crosslinking for the continuous production of uniform chitosan-based nanoparticles with active compounds.

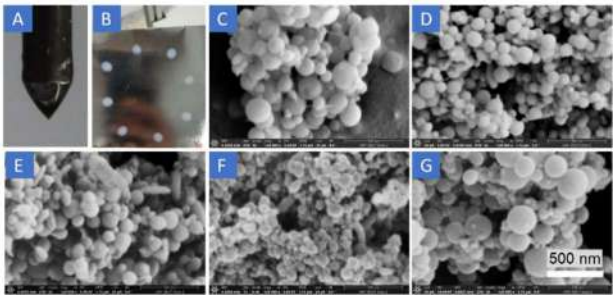

Figure 1. (A) Co-axial Taylor cone. (B) Collection spots. (C-G) FESEM images of nanoparticles obtained under different formulations: (C) Both outer and inner flows are chitosan-only solutions. (D-G) Crosslinking agent solutions are in the inner flow and in the outer flow are the chitosan solutions containing the active compound: (D) Copper(II) nitrate hydrate, (E) caffeine, (F) curcumin and except (G) containing resveratrol in inner flow.

This work was funded by the Spanish Gov. and EU's ERDF (grants PID2021-129064NB-I00 and PDC2022-133989-I00) and the Catalan Gov. (grant 2021SGR-00978).

Castillo, J., Martin, S., Rodriguez-Perez, D., Higuera, F. J., Garcia-Ybarra, P. L. (2018) *J Aerosol Sci.* **125**, 148-163.
Jeong, J., Park, K., Kim, H., Park, I., Choi, J., & Lee, S. S. (2022). *Microsystems & Nanoengineering*, **8**, 110.
Higuera F.J. (2018) *J Aerosol Sci.* **118**, 45-58.
Olvera-Trejo, D. & Velásquez-García, L. F. (2016) *Lab Chip*, **16**, 4121–4132.
Sandri, G., Rossi, S., Bonferoni, M. C., et al. (2012) *J. Drug Delivery Sci. Technol.*, **22**, 275–284.
Sochorakis, N., Grifoll, J., & Rosell-Llompart, J. (2019) *Chemical Engineering Science*, **195**, 281–298.
Zhu, Y. & Chiarot, P. R. (2019) *Journal of Materials Science*, **54**, 6122–6139.

Synthesis of Spray-Dried Iron and Iron–Zinc Based Catalysts for Catalytic Graphitization of Kraft Lignin

M.Taheri[1], K. Murashko[1], D. Donskyi[1], M. Kortelainen[1] and A. Lähde[1]

[1] Fine Particle and Aerosol Technology Laboratory, Department of Environmental and Biological Sciences, University of Eastern Finland, 70210 Kuopio, Finland

Keywords: Ultrasonic spray drying, Aerosol synthesis, Catalytic graphitization, Kraft lignin, Bimetallic catalysts

Presenting author email: Mojgan.Taheri@uef.fi

The development of efficient catalysts for the catalytic graphitization of biomass-derived carbon is a key challenge in producing sustainable graphite-like materials for energy storage applications. In this work, ultrasonic spray drying was employed as a scalable aerosol-based synthesis route to prepare mono- and bimetallic catalysts for the catalytic graphitization of kraft lignin. An ultrasonic spray dryer was used to generate aerosol droplets and control droplet-to-particle transformation through systematic variation of processing parameters, including precursor flow rate, solution concentration, inlet and outlet temperatures, and residence time (Figure 1).

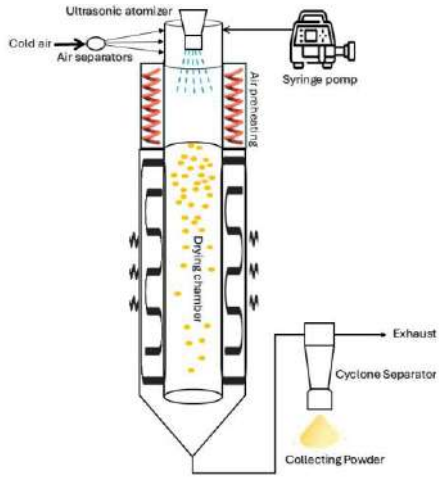

Figure 1. Spray dryer- Aerosol process schematic

Monometallic iron catalysts and bimetallic iron–zinc catalysts with Fe:Zn molar ratios of 1:2, 1:3, and 1:4 were synthesized. Scanning electron microscopy (SEM) revealed predominantly spherical particles with controlled morphology and size, demonstrating effective aerosol-mediated particle formation. Thermogravimetric analysis (TGA) was used to study the thermal decomposition behaviour of the spray-dried catalysts. SEM analysis after calcination confirmed that the spherical particle morphology was retained, indicating good structural stability of the aerosol-derived catalysts under thermal treatment (Figure 2).

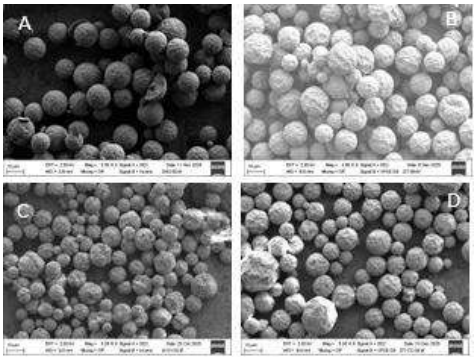

Figure 2. SEM images of catalyst particles: (A) Fe after spray drying, (B) Fe–Zn after spray drying, (C) Fe after calcination, and (D) Fe–Zn after calcination.

The spray-dried catalysts were applied for the graphitization of kraft lignin, with the Fe–Zn (1:3) bimetallic system selected for detailed study due to its favourable particle size characteristics. Structural characterization by Raman spectroscopy, XRD, and SEM showed that the Fe–Zn catalyst significantly enhanced graphitic ordering compared to monometallic Fe (Figure 3).

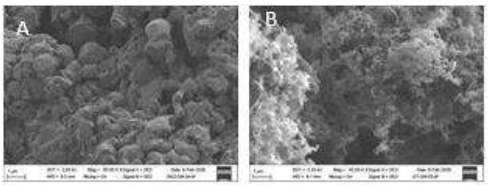

Figure 3. Graphitized carbon: (A) carbon produced using Fe catalyst and (B) carbon produced using Fe–Zn catalyst.

These results demonstrate that ultrasonic spray drying enables aerosol-assisted control over catalyst architecture, while Fe–Zn bimetallic synergy plays a crucial role in promoting efficient catalytic graphitization of kraft lignin. The study highlights the importance of aerosol process design in developing scalable catalyst systems for sustainable carbon materials.

This work was supported by EKOAKKU, ERDF grant R-01819 and NovelSusMat, TT-100V Foundation grant.

Zhang, S., et al. (2025) Sustainable Materials and Thechnologies 43, e01250.

Computational generation and discrete mechanics simulation of three-dimensional fibrous structures

Ioannis-Pantelis (Giagkos) Bamichas[2] and Athanasios G. Konstandopoulos[1,2]

[1]Aerosol & Particle Technology Laboratory, Aristotle University, Thessaloniki, 54124, Greece
[2]SYNEST PC, 19-21 G. Gennimata Str, Thessaloniki, 55535, Greece
Keywords: stochastic fibrous media; discrete mechanics; mass-spring model; permeability; tortuosity.

Presenting author email: gb@sy-nest.com

This work presents the development and application of a computational model for the generation and analysis of stochastic fibrous structures in three-dimensional space. The objective is to investigate how geometric randomness and fiber-scale mechanical parameters govern the macroscopic morphological and transport-relevant properties of the resulting fibrous medium. The fiber deposition process is simulated using a particle-based mass-spring representation, with the equations of motion advanced using a Verlet-type integration scheme (Verlet, 1967).

Rather than prescribing a static random geometry, the structure is allowed to emerge from mechanically constrained fiber deposition. The discrete representation enforces fiber connectivity, bending compliance and contact interactions, so that the final pore space reflects the combined effects of stochastic placement and fiber-scale mechanics. This makes the framework suitable for virtual prototyping of fibrous media, where changes in fiber properties can be propagated directly to morphology and transport-relevant descriptors before fabrication.

The generated structures are voxelized and analyzed to extract porosity, specific surface area, permeability, hydraulic radius, total contact area and tortuosity indicators. Parametric studies examined fiber stiffness, diameter, number and length of fibers, spatial distribution and stochastic diameter variability based on a Gaussian distribution. Similar discrete and physics-based approaches have been used to study fiber rigidity in virtual electrospun mats and realistic nonwoven microstructures using bead-spring fiber representations (Venkateshan et al., 2016; Moghadam et al., 2019).

The results show that fiber stiffness is a primary control on structural arrangement, directly affecting porosity, tortuosity, inter-fiber contact and permeability. The number and length of fibers mainly govern vertical build-up, volume, porosity and flow descriptors such as hydraulic radius and permeability, while other descriptors remain comparatively stable. Gaussian diameter variability affects most properties, especially permeability and contact area, even at constant mean diameter. Overall, the model was numerically stable and physically consistent, supporting optimization of fibrous media for filtration and aerosol capture (Konstandopoulos, et al 2003; Zarvalis et al. 2011) biomedical scaffolds and nonwoven material designs.

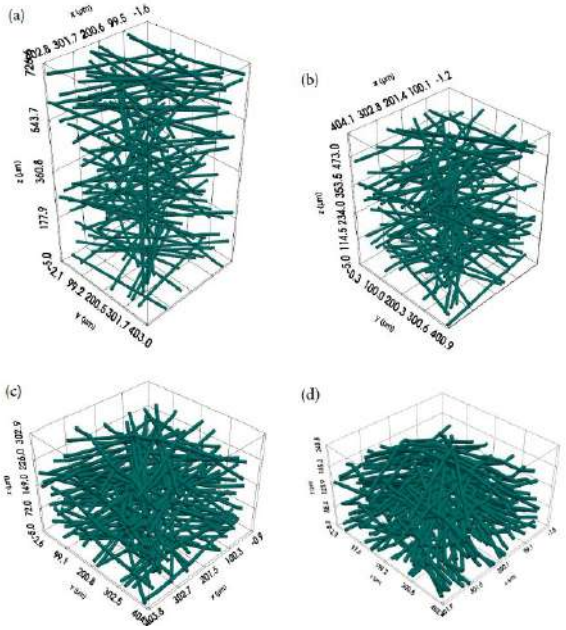

Figure 1. Visual representation of the effect of decreasing stiffness parameter values on the generated structure, from 2×10^{16} to 2×10^{13} N/(m·kg), for panels (a)–(d).

Konstandopoulos, A.G., Vlachos, N., Housiada, P., Kostoglou, M. (2003) Simulation of triangular-cell-shaped, fibrous wall-flow filters. *SAE Transactions*, 112, 680–690.

Verlet, L. (1967) Computer "Experiments" on Classical Fluids. I. Thermodynamical Properties of Lennard-Jones Molecules. *Physical Review*. 159, 98-103.

Venkateshan, D.G., Tahir, M.A., Tafreshi, H.V., Pourdeyhimi, B. (2016) Modeling effects of fiber rigidity on thickness and porosity of virtual electrospun mats. *Materials & Design*. 96, 27-35.

Moghadam, A., Yousefi, S.H., Tafreshi, H.V., Pourdeyhimi, B. (2019) Characterizing nonwoven materials via realistic microstructural modeling. *Separation and Purification Technology*. 211, 602-609.

Zarvalis, D., et al. (2011) A metal fibrous filter for diesel hybrid vehicles. *SAE International Journal of Engines*, 4, 537–552.